Electron and soft x-ray spectroscopy of indium sulfide buffer layers and the interfaces in Cu(In,Ga)(S,Se)$_2$-based thin-film solar cells

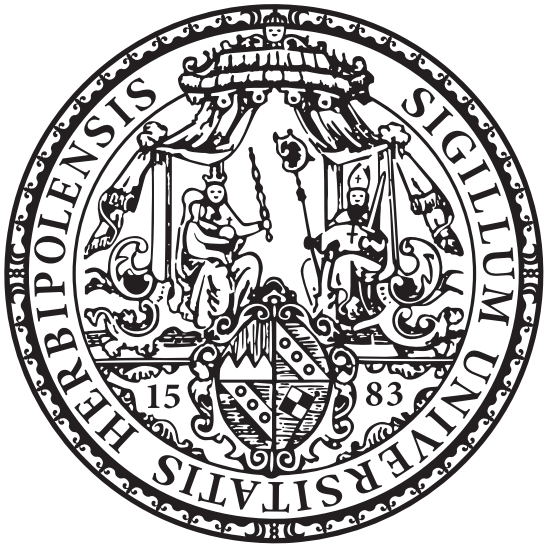

Dissertation zur Erlangung des naturwissenschaftlichen Doktorgrades der Julius-Maximilians-Universität Würzburg

vorgelegt von

Dirk Hauschild
aus Gera

Würzburg 2015

Eingereicht am: 20.08.2015
bei der Fakultät für Physik und Astronomie

1. Gutachter: Prof. Dr. Friedrich Reinert
2. Gutachter: Prof. Dr. Jens Pflaum
der Dissertation

Vorsitzende(r): Prof. Dr. Karl Brunner

1. Prüfer: Prof. Dr. Friedrich Reinert
2. Prüfer: Prof. Dr. Jens Pflaum
3. Prüfer: Prof. Dr. Matthias Kadler
im Promotionskolloquium

Tag des Promotionskolloquiums: 29.01.2016

Doktorurkunde ausgehändigt am:

Für Melanie, Anni und Julius

Abstract

In this thesis, thin-film solar cells on the basis of Cu(In,Ga)(S,Se)$_2$ (CIGSSe) were investigated. Until today, most high efficient CIGSSe-based solar cells use a toxic and wet-chemical deposited CdS buffer layer, which doesn't allow a dry inline production. However, a promising and well-performing alternative buffer layer, namely indium sulfide, has been found which doesn't comprise these disadvantages. In order to shed light on these well-performing devices, the surfaces and in particular the interfaces which play a major role for the charge carrier transport are investigated in the framework of this thesis. Both, the chemical and electronic properties of the solar cells' interfaces were characterized.
In case of the physical vapor deposition of an In_xS_y-based buffer layer, the cleaning step of the CdS chemical-bath deposition is not present and thus changes of the absorber surface have to be taken into account. Therefore, adsorbate formation, oxidation, and segregation of absorber elements in dependence of the storing temperature and the humidity are investigated in the first part of this thesis.
The efficiencies of CIGSSe-based solar cells with an In_xS_y buffer layer depend on the nominal indium concentration x and display a maximum for $x = 42\,\%$. In this thesis, In_xS_y samples with a nominal indium concentration of $40.2\% \leq x \leq 43.2\%$ were investigated by surface-sensitive and surface-near bulk-sensitive techniques, namely with photoemission spectroscopy (PES) and x-ray emission spectroscopy (XES). The surfaces of the films were found to be sulfur-poor and indium-rich in comparison with stoichiometric In_2S_3. Moreover, a direct determination of the band alignment at the In_xS_y/CISSe interface in dependence of the nominal indium concentration x was conducted with the help of PES and inverse PES (IPES) and a flat band alignment was found for $x = 42\,\%$.
In order to study the impact of a heat treatment as it occurs during subsequent cell process steps, the indium sulfide-buffered absorbers were annealed for 30 minutes under UHV conditions at 200 °C after the initial data set was taken. Besides a reported enhanced solar cell performance, a significant copper diffusion from the absorber into the buffer layer takes place due to the thermal treatment. Accordingly, the impact of the copper diffusion on the hidden In_xS_y/CISSe interface was discussed and for $x = 40.2\,\%$ a significant cliff (downwards step in the conduction band) is observed. For increasing x, the alignment in the conduction band turns into a small upwards step (spike) for the region $41\,\% \leq x \leq 43.2\,\%$. This explains the optimal solar cell performance for this indium contents.
In a further step, the sodium-doped indium sulfide buffer which leads to significantly higher efficient solar cells was investigated. It was demonstrated by PES/IPES that the enhanced performance can be ascribed to a significant larger surface band gap in comparison with un-

doped In_xS_y. The occurring spike in the Na:In_xS_y/CISSe band alignment gets reduced due to a Se diffusion induced by the thermal treatment. Furthermore, after the thermal treatment the sodium doped indium sulfide layer experiences a copper diffusion which is reduced by more than a factor of two compared to pure In_xS_y.
Next, the interface between the Na:In_xS_y buffer layer and the i-ZnO (i = intrinsic, non-deliberately doped), as a part of the transparent front contact was analyzed. The i-ZnO/Na:In_xS_y interface shows significant interdiffusion, leading to the formation of, e.g., ZnS and hence to a reduction of the nominal cliff in the conduction band alignment.
In the last part of this thesis, the well-established surface-sensitive reflective electron energy loss spectroscopy (REELS) was utilized to study the CIGSSe absorber, the In_xS_y buffer, and annealed In_xS_y buffer surfaces. By fitting the characteristic inelastic scattering cross sections $\lambda K(E)$ with Drude-Lindhard oscillators the dielectric function was identified. The determined dielectric functions are in good agreement with values from bulk-sensitive optical measurements on indium sulfide layers. In contrast, for the chalcopyrite-based absorber significant differences appear. In particular, a substantial larger surface band gap of the CIGSSe surface of $E_{Gap}^{Ex} = (1.4 \pm 0.2)\,\mathrm{eV}$ in comparison with bulk values is determined. This provides for the first time an independent verification of earlier PES/IPES results. Finally, the electrons' inelastic mean free paths λ for the three investigated surfaces are compared for different primary energies with theoretical values and the universal curve.

Zusammenfassung

Die vorliegende Arbeit untersucht Dünnschichtsolarzellen auf Basis von Cu(In,Ga)(S,Se)$_2$ (CIGSSe). Um hohe Effizienzen bei CIGSSe-basierten Solarzellen zu erreichen, wurde bisher meist eine toxische und schlecht in einen Vakuumprozess integrierbare nasschemische CdS Pufferschicht verwendet. Mit Indiumsulfid konnte stattdessen eine vielversprechende alternative Pufferschicht gefunden werden, die diese nachteiligen Eigenschaften von CdS nicht aufweist und Solarzellen mit diesem Puffermaterial zeigen gute bis sehr gute Wirkungsgrade. Um die Ursachen der guten Leistungen herauszufinden, wurden die in der Solarzelle vorkommenden Oberflächen und Grenzflächen, die für den Ladungstransport eine zentrale Rolle spielen, Schritt für Schritt als Modellsysteme charakterisiert.
Für einen In_xS_y-basierten Puffer, der durch die physikalische Gasphasenabscheidung aufgebracht wird, fehlt der Reinigungsprozess der Absorberoberflächen durch die nasschemische CdS Abscheidetechnik. Deshalb müssen Adsorbatbildung, Oxidation und Segregation von Absorberelementen die innerhalb der ersten Tage nach der Herstellung auftreten (je nach Feuchtigkeitsgehalt und Temperatur der Umgebung) berücksichtigt werden. Im ersten Teil der Arbeit werden solche Einflüsse auf die Oberfläche des Absorbers untersucht.
Zellen mit einem Indiumsulfidpuffer zeigen Wirkungsgrade, die von der nominellen Indiumkonzentration x abhängen und bei $x = 42\,\%$ ein Optimum aufweisen. Eine stöchiometrische Analyse der In_xS_y Oberflächen ergab für $40.2\% \leq x \leq 43.2\%$ eine schwefelarme bzw. indiumreiche Oberfläche im Vergleich zu stöchiometrischem In_2S_3 (40 % In und 60 % S). Allerdings zeigen die untersuchten Proben für verschiedene Indiumkonzentrationen im Rahmen der oberflächensensitiven Photoemission (PES) und volumensensitiven Röntgenemission (XES) keine quantitativen Unterschiede. Mit Hilfe der PES und inversen PES (IPES) wurde der Bandverlauf an der In_xS_y/CISSe Grenzfläche in Abhängigkeit von der Indiumkonzentration untersucht und für $x = 42\,\%$ konnte ein flacher Bandverlauf ermittelt werden.
Um den Einfluss des im Herstellungsprozess vorkommenden Temperaturschritts zu untersuchen, wurden die Proben für 30 Minuten auf 200 °C geheizt. Dabei konnte eine signifikante Diffusion von Kupfer aus dem Absorber in den Puffer beobachtet werden. Der Temperaturschritt führt neben der bereits bekannten Effizienzerhöhung vor allem zu einer Verringerung der Bandlücke des Puffers. Der Einfluss der Kupferdiffusion auf die verborgene In_xS_y/CISSe Grenzfläche wurde analysiert und für $x = 40.2\,\%$ wurde ein deutlicher "Cliff" (Stufe im Leitungsband nach unten) gefunden. Für Indiumkonzentrationen $41\,\% \leq x \leq 43.2\,\%$ wurde ein kleiner "Spike" (Stufe im Leitungsband nach oben) identifiziert, was dabei im Einklang mit den optimalen Wirkungsgraden ist.

In einem weiteren Schritt wurde ein mit Natrium dotierter Indiumsulfidpuffer Na:In_xS_y, der verbesserte Wirkungsgrade zeigt, untersucht. Diese konnte zum einen auf eine deutlich vergrößerte Oberflächenbandlücke des Puffers zurückgeführt werden. Zum anderen wurde nach dem Temperaturschritt im Vergleich zu dem In_xS_y Puffer eine um den Faktor zwei verringerte Kupferdiffusion an der Oberfläche festgestellt. Des Weiteren konnte bei dem Temperaturschritt eine Diffusion von Selen festgestellt werden, die den vor dem Temperaturschritt vorhandenen "Spike" im Leitungsbandverlauf verringert.
Nach dem Aufbringen der i-ZnO Schicht (i = intrinsisch, nicht absichtlich dotiert) als Teil des Frontkontakts auf den Na:In_xS_y Puffer, wurden Durchmischungseffekte an der i-ZnO/Na:In_xS_y Grenzfläche gefunden. Im weiteren Verlauf zeigte sich, dass der nominell auftretende "Cliff" zwischen i-ZnO und Na:In_xS_y durch die Bildung von ZnS reduziert bzw. vernachlässigt werden kann.
Im letzten Teil der Arbeit wurde die etablierte oberflächensensitive reflektive Elektronenenergieverlustspektroskopie auf die Absorber- sowie Indiumsulfidoberflächen angewandt. Die ermittelten inelastisch gestreuten Verlustspektren $\lambda K(E)$ wurden mit dem Drude-Lindhard Modell simuliert und somit die dielektrische Funktion der jeweiligen Oberflächen bestimmt. Ein Vergleich mit volumensensitiven optischen Werten zeigt für die In_xS_y Schichten eine gute Übereinstimmung. Bei der CIGSSe Oberfläche konnten hingegen signifikante Unterschiede festgestellt werden. Dabei wurde erstmals die Oberflächenbandlücke eines Cu(In,Ga)$(S,Se)_2$ Absorbers unabhängig von PES/IPES zu $E_{Gap}^{Ex} = (1.4 \pm 0.2)\,\mathrm{eV}$ verifiziert.
Abschließend wurden die mittleren freien Weglängen der Elektronen λ für die drei untersuchten Oberflächen für unterschiedliche Energien mit theoretischen Werten und der universellen Kurve verglichen.

Contents

1

Introduction

The nuclear power phase-out has led to an ongoing restructuring of the energy supply in Germany with renewable energy sources. In this process, solar cells have also gained higher significance. Therefore, it is not surprising that besides the well-established silicon-based solar cells, thin-film solar cells that promise lower production cost attract much interest. In fact, thin-film solar cells have superior properties in comparison with silicon-based solar cells, e.g., a direct optical band gap. Accordingly, the high efficiencies of thin-film chalcopyrite (Cu(In,Ga)(S,Se)$_2$)-based solar cells on laboratory scales (21.7 % [1]) as well as on large scale (17.5 % [2]) show the promising potential of this material.

A Cu(In,Ga)(S,Se)$_2$ (CIGSSe) solar cell usually consists of the back contact, the p-type absorber, the n-type buffer layer, and the transparent front contact. Each layer and therefore the respective interfaces influence the performance of a such solar cell. Thus, the multiplicity of electronic relevant effects at the interfaces make it a very complex system which requires the investigation of the chemical and electronic properties of the individual confinements. Beneficial effects in terms of efficiency are attributed to the buffer layer, though the working principle of the buffer layer is not yet fully understood. Consequently, it is crucial to understand the properties of the buffer as well as the properties of the buffer/absorber interface. In more detail, especially the conduction band alignment at the buffer/absorber interface plays an essential role for the charge carrier transport from the absorber to the front contact. While the most efficient solar cells have been processed with a wet-chemical

deposited state-of-the-art CdS buffer layer, industry is more and more favoring alternative buffer layers which are less toxic, more transparent, and capable of being integrated in a vacuum-based process line [3, 4].

The following approaches are promising candidates to replace CdS and still yield high efficiencies for chalcopyrite-based thin-film solar cells [5]: $ZnO_{1-x}S_x$, $Zn_{1-x}Mg_xO$, and In_xS_y. The here investigated indium sulfide buffer layers turned out to be the most promising material for the AVANCIS CIGSSe absorber as they achieve 17.1 % efficiency on large areas ($30 \times 30\,cm^2$) and thus overtake the CdS buffered CIGSSe thin-film solar cell [6]. The aim of this thesis is to uncover the secrets behind these high efficiencies and give further input for possible improvements. For this purpose, the samples were taken directly from the AVANCIS pilot line in Munich.

Since the surface cleaning step of the chemical bath deposition [7] is omitted when using dry-deposited buffer layers, the impact of environmental conditions on the absorber such as adsorbate formation, oxidation of absorber elements, or segregation processes have to be taken into account, which is covered in the first part of this thesis. In a further step, the chemical and electronic properties of different surfaces and interfaces in a CIGSSe-based solar cell are studied in detail. In particular, the chemical structure of the In_xS_y/CIGSSe junction is investigated by means of surface-sensitive photoemission spectroscopy (PES) and bulk-sensitive x-ray emission spectroscopy (XES), while the electronic structure is directly determined by a combination of ultraviolet PES (UPS) and inverse PES (IPES). Only the combination of these techniques allows a direct determination of the electronic band alignment [8, 9]. Solar cells with an indium sulfide buffer often require an annealing step at 200 °C in order to improve the solar cell performance [10]. Hence, the impact of this high-temperature step on the systems in terms of the chemical and electronic structure is investigated. After determining a comprehensive picture, the sodium-doped indium sulfide layer is investigated.
Doping the In_xS_y layer with sodium leads to a further improvement, i.e., its band gap is significant increased. The according changes of the chemical and electronic structure of the Na:In_xS_y/CIGSSe interface are probed and interdiffusion phenomena upon a thermal treatment are monitored. Moreover, the influence of depositing additional cover layers, i.e., the transparent ZnO front contact, has so far been neglected, the impact of the ZnO sputter step is probed. All these investigations draw together a comprehensive picture of the complex chemical and electronic structure of the solar cell.

Besides the chemical and electronic properties at the surface its optical properties play a crucial role for the performance of a solar cell device. However, the commonly employed optical measurements are only able to gather the optical properties of the complete device.

An alternative method to directly obtain the dielectric function ε of a material's surface is the reflective electron energy loss spectroscopy (REELS). Therefore, it is applied to the CIGSSe absorber, the In_xS_y, and the annealed In_xS_y surfaces. This technique gives insights into the surface-related optical properties and also provides fundamental information about the electronic structure including the surface band gap being complementary to UPS/IPES.

In the following, a brief outline of the present thesis and the respective contents is given:

Chapter 2 provides the relevant theoretical background which is necessary to interpret the measured data.

In chapter 3, the used setup is described. An introduction of the chalcopyrite-based absorber and the buffer layer materials follows in chapter 4.

Chapter 5 considers the impact of three different environmental conditions (nitrogen atmosphere, ambient conditions, and damp heat conditions) on the $Cu(In,Ga)(S,Se)_2$ surface for up to 14 days.

Chapter 6 investigates the chemical and electronic properties of different interfaces and the impact of a heat-treatment on the respective properties. Thereby, the chapter is divided into three sections: the In_xS_y/CISSe interface, the sodium doped Na:In_xS_y/CISSe interface, and the i-ZnO/Na:In_xS_y interface.

In chapter 7, the REELS approach is applied to three different surfaces. Furthermore, a depth-resolved picture of the absorber's optical properties is presented. With the focus on the above given aims of this thesis, chapter 8 finally recapitulates the results and gives an outlook on further improvements.

Parts of this thesis are published in peer-reviewed journals, chapter 5 in Ref. [11] and chapter 6 in Ref. [12].

2

Theoretical background and methods

2.1 Interactions of photons with matter

Photoemission spectroscopy

The photoelectric effect, i.e., the release of an electron when light irradiates a sample was discovered by Hertz and Hallwachs in 1887 [13, 14]. With the introduction of the quantum nature of light this effect could be described theoretically by Einstein in 1905 [15]. Over the last decades this effect has been utilized to investigate the electronic structure of samples since the photoemitted electron (photoelectron) transports the information of the (occupied) electronic states of the investigated sample. The corresponding technique is called photoemission spectroscopy (PES) and includes ultraviolet photoemission (UPS) for the investigation of the valence band and x-ray photoemission spectroscopy (XPS). The latter technique is typically conducted with photons of $\approx 1\,\mathrm{keV}$ to investigate core-levels. The inelastic mean free path of the photoelectron (IMFP) excited at such photon energies (leading to electron kinetic energies below the photon energy) is typically around $2-3\,\mathring{A}$ allowing to investigate the surface of a system. The IMFP is defined as the distance in a medium after which the intensity of an electron beam is decayed to $1/e$ of its initial value.

In the following, a very brief introduction to PES will be given. For further details the reader is referred to several publications and text books, e.g., [16, 17]. It should be noted that the investigated samples are many-body systems whereas a single-particle picture may act as starting point for understanding photoemission spectra. Using time-dependent first order perturbation theory, Fermi's golden rule gives the probability for a specific transition per unit of time [18]

$$w_{i\to f} = \frac{2\pi}{\hbar} \mid \langle \psi_f | \hat{H}_P | \psi_i \rangle \mid^2 \delta(E_i - E_f - \hbar\omega) \; . \tag{2.1}$$

Here, a photon with the energy $\hbar\omega$ excites the system from its initial state $|\psi_i\rangle$ to a final state $\langle\psi_f|$. The delta function δ accounts for the energy conservation and the perturbation operator $\hat{H}_P$ represents the interaction of the system with an electromagnetic field $\hat{A}$. For small electromagnetic fields and using the Coulomb gauge the perturbation operator $\hat{H}_P$ can be expressed by

$$\hat{H}_P = \frac{e}{m_e c}\hat{A}\hat{p} \; , \tag{2.2}$$

where $\hat{p}$ is the momentum operator. Assuming that the interaction of the photoelectron with the $(N-1)$ electron system can be neglected (sudden approximation), the initial state wave function can be written as a product of the excited electron's orbital $\phi_{i,k}$ and the wave function of the remaining $(N-1)$ electrons $\psi_i(N-1)$. Accordingly, the final state wave function is factorized as product of the wave function of the photoelectron $\phi_{f,E_{Kin}}$ and the remaining electrons $\psi_f(N-1)$. Thus, the transition matrix element in equation 2.1 can be written as

$$\langle \psi_f | \hat{A}\hat{p} | \psi_i \rangle = \langle \phi_{f,E_{Kin}} | \hat{A}\hat{p} | \phi_{i,k} \rangle \, \langle \psi_f(N-1) \mid \psi_i(N-1) \rangle \; . \tag{2.3}$$

This allows to separate the matrix element in two factors: the first consists of the perturbation operator acting on the single-electron orbitals, while the second factor consists of an $(N-1)$ electron overlap integral. The frozen orbital approximation assumes that the remaining orbitals are identical in the final and initial state which means $|\psi_f(N-1)\rangle = |\psi_i(N-1)\rangle$, i.e., the overlap integral equals one. Hence, in a photoemission experiment the binding energy corresponds to the negative of the orbital energy $E_{B,k} \simeq -\varepsilon_k$ and thus $E_{kin} = h\nu - E_{Bind}$.

This approximation neglects any screening of the remaining hole by the (N-1) system. In addition, extrinsic losses, e.g., excitation of electrons in unoccupied states or plasmons have to be taken into account. The treatment of such losses will be discussed later in this chapter.

With the help of XPS, each characteristic core-level binding energy of a sample's spectrum can be referred to an element and in particular, with the chemical shift of the core level the

chemical surrounding of the investigated element can be investigated. Moreover, with the core-level intensities the stoichiometric composition can be calculated.

UPS allows to probe the valence band of a sample. Taking the energy and the momentum conservation into account, the band structure can be measured. For $\vec{k}$-integrating measurements (as it is usually the case for polycrystalline samples), in a first approximation the density of states is recorded.

Inverse photoemission spectroscopy

PES allows to detect the occupied states below the Fermi level. Complementary to this, the unoccupied states can be studied using inverse photoemission spectroscopy (IPES). In a similar fashion as PES extracts one electron from the system, IPES adds one electron weighted with the transition matrix element from Fermis golden rule (for comparison see equation 2.1). In IPES the sample is irradiated with mono-energetic electrons which recombine into the empty states. The resulting fluorescence is detected at a fixed photon energy with a band-pass detector:

$$\hbar\omega = E_{Kin} + \Phi_{E-Gun} + E_{Bind} \ . \tag{2.4}$$

Here, E_{Kin} is the kinetic energy of the electron and Φ_{E-Gun} is the work function of the electron gun.

The ratio of the cross sections of IPES and PES in the UV regime is of the order of 10^{-5}. This low cross section of IPES makes this technique challenging in terms of measurement time and potential radiation damage. In the present thesis, IPES is used to probe the conduction band states of several samples and determine the conduction band minimum in order to calculate the conduction band offset. Further information about IPES can be found e.g., in Refs. [19, 20]

(X-ray excited) Auger electron spectroscopy

In a two-step model, a core hole is first filled by an outer shell electron causing the emission of x-rays or the emission of an Auger electron. Both processes are in competition with each other, however, the Auger decay is more likely, especially for light elements as shown in Fig. 2.1 for the K shell. The core hole necessary for the Auger process can be excited with electrons (AES), or with x-rays (XAES), the latter was used in this thesis. The final state of the Auger process includes the emitted Auger electron and two interacting holes. Hence, a

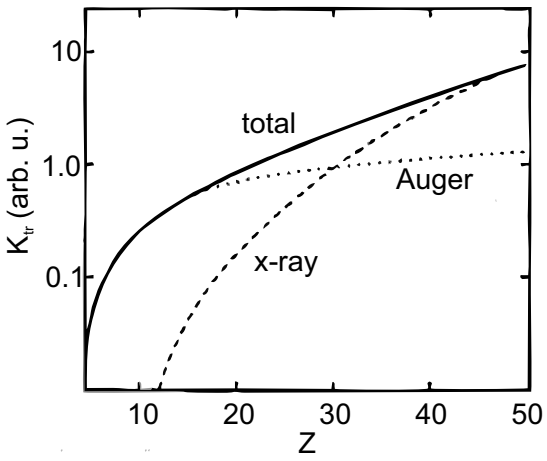

Figure 2.1: Calculated probability for the K shell K_{tr} for the competing Auger and x-ray emission in dependence of the atomic number Z. Graphic adapted from Ref. [16].

strong influence of the environment on the Auger electron kinetic energies $E_{kin}(C_1,C_2,C_3)$ is expected and it can be written as follows [21]:

$$E_{kin}(C_1,C_2,C_3) = E_{Bind}(C_1) - E_{Bind}(C_2) - E_{Bind}(C_3) - U(C_2,C_3)\ . \tag{2.5}$$

Here, C_i are the single-hole binding energies of the respective core levels and $U(C_2,C_3)$ is the energy related to the Coulomb interaction between the final state holes [21]. The influence of the chemical surrounding gives rise to the identification of the chemical bond with the modified Auger parameter [22]:

$$\alpha' = E_{Bind}(C_c) + E_{Kin}(Auger), \tag{2.6}$$

where $E_{Bind}(C_c)$ is the binding energy of the core level and $E_{Kin}(Auger)$ is the kinetic energy of the most prominent Auger transition. The benefit of using the modified Auger parameter is that α' is neither affected by charging nor interface and surface potentials [23]. A powerful approach is the presentation in the commonly known Wagner plot, where $E_{Kin}(Auger)$ is plotted against a decreasing $E_{Bind}(C_c)$. Here, a distinct Auger parameter is a linear function with slope -1 [24]. For a more detailed description the reader is referred to Refs. [21, 23–25].

X-ray emission spectroscopy

As stated above, a generated core hole can be filled by an outer shell electron under the radiation of x-rays. In the following, only the non-resonant excitation of an inner shell is discussed which allows to separate the excitation processes from the emission processes. According to the excited electron shell, e.g., 1s, 2s, or 2p the resulting x-rays are called K, L_1, or $L_{2,3}$ fluorescence, respectively. In x-ray emission spectroscopy (XES) the intensity is measured as a function of the emitted photon energy. The radiative recombination probability is determined by the dipole matrix element $|M_{fi}|^2 \sim |\langle\phi_f|\vec{e}\,\vec{r}|\phi_i\rangle|^2$ (see equation 2.1), where $\vec{e}$ is the direction of the out coming polarization of the light. It should be noted that the dipole transition implies the dipole selection rules [16], which includes, e.g., the change of the angular momentum quantum number $\Delta L = \pm 1$ between initial and final state. This transition probability turns out to be approximately $\sim Z^4$ [16] which is the reason for a low x-ray fluorescence for atomic numbers $Z < 30$.

XES is characteristic for each element as well as site-specific and hence probes the local occupied density of electronic states (LDOS) of a material which allows to monitor the local chemical environment of a specific atom species. The hole is typically generated by photons provided by a synchrotron facility. This "photon-in photon-out" technique has a much larger inelastic mean free path in comparison to PES and is thus more bulk sensitive. Furthermore, this technique is insensitive to sample charging. Consequently, x-ray emission spectroscopy is a widely applied tool to study the local electronic structure of solids and liquids.

2.2 Interactions of electrons with matter

The spectroscopies discussed in the previous section use light to investigate solids. Besides photons, a probing electron beam can interact directly with the electronic system and can be utilized for spectroscopy, too. In electron energy loss spectroscopy (EELS) the energy losses of electrons due to interaction with a sample are studied (even the excited PES electron undergoes these losses). In the following, the dielectric function will be introduced in order to describe scattering intensities in an EELS experiment.

The dielectric function of condensed matter

The dielectric function ε is fundamental for solid-state spectroscopies and characterizes the properties of matter in dependence of the frequency ω and wave vector $\vec{k}$. In the following, the problem is simplified and a dielectric function ε is used which depends only on ω. The dielectric function ε links the electric field $\vec{E}$ with the electric displacement field $\vec{D}$ according to [16]

$$\vec{D} = \varepsilon_0 \varepsilon \vec{E} \; . \tag{2.7}$$

The dielectric function (a common designation also is permittivity) is a measure of how a dielectric medium is influenced by an electric field, i.e., how easy atoms are polarized. The dielectric function is linked with the optical constants of the refractive index n and extinction coefficient κ [26]:

$$(n + \mathrm{i}\kappa)^2 = \varepsilon_1 + \mathrm{i}\varepsilon_2 \tag{2.8}$$

with the result that

$$n = \sqrt{\frac{1}{2}\left(\sqrt{\varepsilon_1^2 + \varepsilon_2^2} + \varepsilon_1\right)} \tag{2.9}$$

$$\kappa = \sqrt{\frac{1}{2}\left(\sqrt{\varepsilon_1^2 + \varepsilon_2^2} - \varepsilon_1\right)} \; . \tag{2.10}$$

A simple model to characterize the polarization of a medium in dependence of the frequency of an electric field is the Lorentz oscillator, i.e., a damped harmonic oscillator which is excited by a periodically changing external electric field. From the determined polarizability the complex dielectric function $\varepsilon = \varepsilon_1 + \mathrm{i}\varepsilon_2$ can be calculated. The typical shapes of ε_1 and ε_2 are shown in Fig. 2.2. The imaginary part ε_2 of the dielectric function has the shape of a resonance curve. The width of this curve depends on the damping coefficient of the harmonic oscillator. The real part ε_1 of the dielectric function has a static value for $\omega \to 0$. For increasing ω, ε_1 gains intensity, reaches a maximum in the resonance region and decreases subsequently. For $\omega > \omega_1$ the real part ε_1 of the dielectric function is negative for further increasing frequency it converges towards one.

It has to be stated that real materials exhibit more than one resonance frequency. Then the dielectric function consists of several parts, e.g., a quasi-free electron contribution and an interband transition contribution [27]. For the quasi-free electron contribution a characteristic frequency is found, which can be understood as the resonance frequency of longitudinal

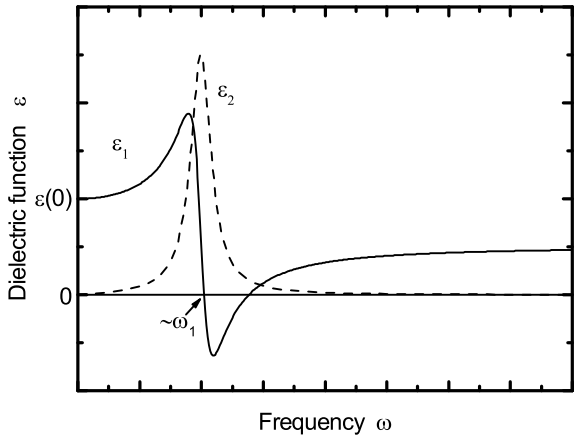

Figure 2.2: Course of the real part ε_1 and of the imaginary part ε_2 in dependence of the frequency ω according to the Lorentz oscillator model. In the case of a weak damping the first zero crossing of ε_1 is approximately at the resonance frequency ω_1.

oscillations of electrons, the so called plasma frequency ω_P. This frequency is defined by the zero crossing of the real part ε_1 of the dielectric function and the imaginary part ε_2 must not have a maximum value [28]. Correspondingly, the plasma oscillation is a collective oscillation of the conduction electrons. This quasi-particle is named plasmon. The plasmon frequency ω_P is proportional to the square root of the charge carrier concentration N_C, so $\omega_P \sim \sqrt{N_C}$. Accordingly, the plasma frequency can be fine-tuned by varying the doping concentration in a semiconductor.

Energy loss of fast electrons in condensed matter

In an inelastic electron scattering experiment the scattering probability P of an electron loosing a certain energy $\hbar\omega$ and momentum $\hbar\vec{k}$ (i.e., scattering angle) is measured. It can be described as [26]

$$P\left(\vec{k},\omega\right)\mathrm{d}\Omega\,\mathrm{d}(\hbar\omega) = \frac{4aN}{a_0^2\vec{k}^4}\,S\left(\vec{k},\omega\right)\mathrm{d}\Omega\,\mathrm{d}(\hbar\omega)\,, \tag{2.11}$$

where a_0, a, and N are the Bohr radius, the layer thickness, and the density of particles, respectively. The form factor $S\left(\vec{k},\omega\right)$ is a fundamental measure for many-body systems and correspondingly, the primary object for a calculation. With the help of the dielectric theory the form factor can be connected to the imaginary part of the dielectric function. Thereby it is assumed that a point charge is introduced in a solid and by moving the point

charge a polarization of the surrounding occurs. The appearing electric field affects the charged particle. The energy loss per time as well as the according form factor can be calculated [26]

$$S\left(\vec{k},\omega\right) = -\frac{\hbar\vec{k}^2}{4\pi^2 e^2 N}\mathrm{Im}\frac{1}{\varepsilon(\vec{k},\omega)} \ . \tag{2.12}$$

An advantage of this notation is the relative simple way of calculating a many-body system. Furthermore, excitation of oscillation of a system (as shown above) can be described and the influence of surfaces can be included.

The focus in equation 2.12 is on the factor $-\mathrm{Im}\frac{1}{\varepsilon(\vec{k},\omega)}$, which determines the retardation of the charged particle. This factor is called energy loss function (ELF), since it determines the energy loss spectrum. It can be further written [26]

$$-\mathrm{Im}\frac{1}{\varepsilon(\vec{k},\omega)} = -\mathrm{Im}\frac{\varepsilon_1 - \mathrm{i}\varepsilon_2}{\varepsilon_1^2+\varepsilon_2^2} = \frac{\varepsilon_2}{\mid \varepsilon \mid^2} \ . \tag{2.13}$$

The imaginary part of the dielectric function ε_2 is determined by single excitations. However, the ELF and therefore equation 2.11 include collective excitations. The real part ε_1 characterizes the screening of the electrons and the ions under the presence of an external field. Thus, ε_1 is a measure of collective excitations. In contrast, the imaginary part ε_2 characterizes the damping of an external field due to the excitation of electron transitions in the solid. Hence, in the ELF (equation 2.13) the numerator ε_2 indicates the excitation of an electron and the denominator $\mid \varepsilon \mid^2$ indicates the impact of the surrounding electrons and ions. Knowing only the real or imaginary part is sufficient to calculate the ELF. In fact, ε_1 and ε_2 are not independent of each other and the counterpart can be calculated with the help of the Kramers-Kronig relation [29, 30].

The complete information of the bulk dielectric function of a solid can be probed by optical reflection measurements and utilizing equation 2.8. A further possibility to determine ε is the excitation with electrons with the assumption that no multiple scattering events occur. This is usually given for high primary electron energies and thin foils. In particular, for the investigation of fast electrons which lose energy in thin foils by means of transmission electron energy loss spectroscopy (TEELS) surface contamination can be neglected. However, multiple losses have to be taken into account in a reflection EELS (REELS) experiment and thus have to be subtracted in a recursive equation for further evaluations. The inelastic scattering cross section $\lambda K(E)$ (weighted with the IMFP) in which only single-scattering events are included can be calculated assuming a homogeneous scattering probability $K(E,T)$ per

energy loss T [31]:

$$\lambda(E_0)K(E_0,E_0-E_i) = \frac{1}{j_l(E_0)\Delta E}\left[j_l(E_i) - \sum_{m=1}^{i-1}\lambda K(E_0,E_m-E_i)\,j_l(E_m)\Delta E\right], \quad (2.14)$$

where E_0 is the incoming primary electron energy, j_l(E) is the measured REELS spectrum and $j_l(E_0)\Delta E$ is the area under the elastic peak. The REELS spectrum is divided into several channels E_i of the energy width ΔE. This $\lambda K(E)$ can be directly correlated to the form factor $S(\vec{k},\omega)$.

A model to calculate the inelastic scattering cross sections as determined from REELS with the dielectric function as input was proposed by Yubero and coworkers which considers a general geometry and incoming electron energy [32]. Inside the solid, the electron travels a multiplicity of different trajectories, which all contribute to the experimental $\lambda K(E)$. Thus, the REELS spectrum is a superposition of all trajectories for different probing depths. In this surface reflection model the electron and its image charge are considered which travel through the vacuum ($\varepsilon = 1$) and in the infinite medium. The inelastic scattering cross section consists of four terms which correspond to the losses of the electron: the incoming electron in the vacuum $K_{eff}^{V_i}$ as well as the medium $K_{eff}^{M_i}$ and the outgoing electron in the medium $K_{eff}^{M_o}$ as well as the vacuum $K_{eff}^{V_o}$ [32].

$$K_{eff} = K_{eff}^{V_i} + K_{eff}^{M_i} + K_{eff}^{M_o} + K_{eff}^{V_o}\,. \quad (2.15)$$

Accordingly, a notation of the inelastic scattering cross section is derived from a given geometry and energy of the primary electrons if the dielectric function ε is known. To model the dielectric function a Lorentz oscillator is commonly used. This Yubero-Tougaard theory was validated several times [33, 34]. For a detailed derivation the reader is referred to Refs. [27, 32].

It should be noted that in contrast to XPS, the electrons have to pass the surface region twice in a REELS experiment. This may result in a different surface and bulk contribution of REELS in comparison with XPS [35]. However, this effect could be minimized by using higher primary electron energies in order to minimize the surface contribution to the REELS spectrum [36].

3

Experimental

3.1 Quantitative evaluation of the data

The measured XPS intensity depends on several factors. In the following, an infinity thick, homogeneous sample, perpendicular detection, and the "magic angle" between photon source and detector so that the angular asymmetry is unity are assumed. Then, the XPS line intensity of an element A at a specific kinetic energy E_A of the photoelectron is given as [37]:

$$I_A \sim \sigma_A N_A \lambda_A(E_A) T(E_A) \; . \tag{3.1}$$

Here, σ_A is the cross section for the emission of a photoelectron, N_A is the atom density, $\lambda_A(E_A)$ is the IMFP at the specific kinetic energy, and $T(E_A)$ is the analyzer transmission function. For the calculation of the stoichiometry the ratio $\frac{N_A}{N_B}$ is calculated where N_B is the atom density of the element B. The area and position of the core levels were determined by a simultaneous fit of Voigt profiles of the peaks where the area ratio was fixed according to the spin-orbit split $(2j+1)$. Before the fit, a linear background was subtracted for convenience. This is a good approximation as the relative error of the determined peak intensity is less than 2 % in comparison with the real background as determined in chapter 7. In all stoichiometric analyses, the cross sections from Yeh and Lindau [38] are used. A

comparison of the cross section values from Yeh and Lindau [38] with alternative values of Scofield [39] reveals a deviation of about 3 % for selected core level ratios which will be assumed as error for further evaluation. The analyzer transmission function T was determined according to [40] and (for a pass energy of 20 eV) the transmission function is computed to $T \sim (E_{Kin})^{-0.6}$. This is in accordance with Erfurth's value [41]. The uncertainty of the IMFP λ and analyzer transmission function T was minimized by investigating peaks with similar kinetic energies, e.g., In 4d, Se 3d, Na 2s, and Cu 3p as well as S 2p and Se 3p whenever possible. In some cases (e.g., S/In ratio for thick In_xS_y layers) it was not possible to avoid significantly different kinetic energies of the respective core levels and thus the errors of T and λ have to be taken into account.

3.2 Interfaces in real solar cells

A real solar cell consists of several layers and interfaces as well as a multitude of different elements and impurities. Hence, it is crucial to characterize and understand the chemical and electronic properties of these components. Due to of the complexity of the solar cells, these systems have been mostly optimized empirically. For further improvements, these empirical optimized parameters have to be understood and therefore further barriers need to be identified. Subsequent, these barriers need to be conquered and the system needs to be characterized in terms of the performed modifications and their influence on the chemical and electronic properties [42].

In 1974, the first chalcopyrite-based solar cell was demonstrated by evaporating a CdS buffer onto a $CuInSe_2$ (CISe) single-crystal absorber [43]. In the following years, the chemical bath deposition of CdS onto a polycrystalline thin-film lead to improved solar cell performances [44, 45]. The reason for the superior performance of polycrystalline thin-films over single-crystals is still not fully understood [46–48]. In any case, it was clear that the interface between CdS and $CuInSe_2$ plays a crucial role for the solar cell efficiency and hence it was assumed that the band alignment shows no spike (i.e., upwards step in the conduction band) which was indirectly measured by Turowski *et al.* [49]. In the following decade, the CdS/CISe interface attracted a lot of research interest. Several experiments as well as theory investigated the band alignment and found a spike-like conduction band alignment for the CdS/CISe interface [50, 51]. However, this finding is the result of calculating conduction band offsets from measured surface-related valence band maximas and bulk band gaps (from optical measurements). Moreover, several publications proposed spike-like align-

ments up to 0.3 eV as beneficial or at least not as unfavorable for the solar cell performance [52–55].

A clear picture of the actual band structure resulted especially from Morkel *et al.* and Weinhardt *et al.* [8, 9]. The utilization of surface sensitive ultraviolet photoemission (UPS) and inverse photoemission (IPES) allows a direct measurement of the conduction band offset and a flat band alignment at the CdS/CISe interface (i.e., offset in the conduction band (CB) alignment of 0 eV) was found. These findings demonstrate that the usage of bulk band gaps cannot be applied here. Due to the short inelastic mean free path (IMFP), photoemission as well as IPES give a surface-sensitive picture of the occupied and unoccupied states. In this context, a direct measurement of surface related band gaps and thus of the conduction band alignment at the interface is possible. In addition, in ultraviolet and inverse photoemission the final state has one hole in the valence band (VB) or one electron in the CB, respectively. This reflects the situation during charge transport and the thus derived band edge positions are often referred to as transport levels [56].

In the following, a brief instruction description is given, how the valence band maximum (VBM) and the conduction band minimum (CBM) values together with the interface induced band bending (see below) are used to derive the corresponding valence and conduction band offsets.

Determination of the band offsets at a p-n junction

In this thesis, the VBM and CBM are derived with a linear extrapolation of the leading band edge. In contrast to the utilization of the first broad peak maximum, the linear extrapolation approach leads to band gaps which are similar to optical measured ones [57–59]. Besides this qualitative argument, there are several arguments which support the linear extrapolation approach. A limited angular resolution of the analyzer leads to an asymmetric experimental broadening towards the Fermi energy due to the $\vec{k}$-dispersion [58]. Additional broadening is also caused by inelastic scattering processes (e.g., phonon excitations) [58]. Furthermore, for the determination of the band positions the fully relaxed (i.e., completely screened hole) energy is essential [58, 59]. Finally, no direct transition in $\vec{k}$-space from the VBM to an unoccupied state is possible for the employed photon energy, an indirect transition is needed and the corresponding spectral shape is reduced which can possibly be noticed in a foot at the band edge [60]. It has to be mentioned that all above given statements are also true for the inverse photoemission. In addition, the measurements on the polycrystalline samples are k-integrated. This suggests that in first approximation the density of states is recorded.

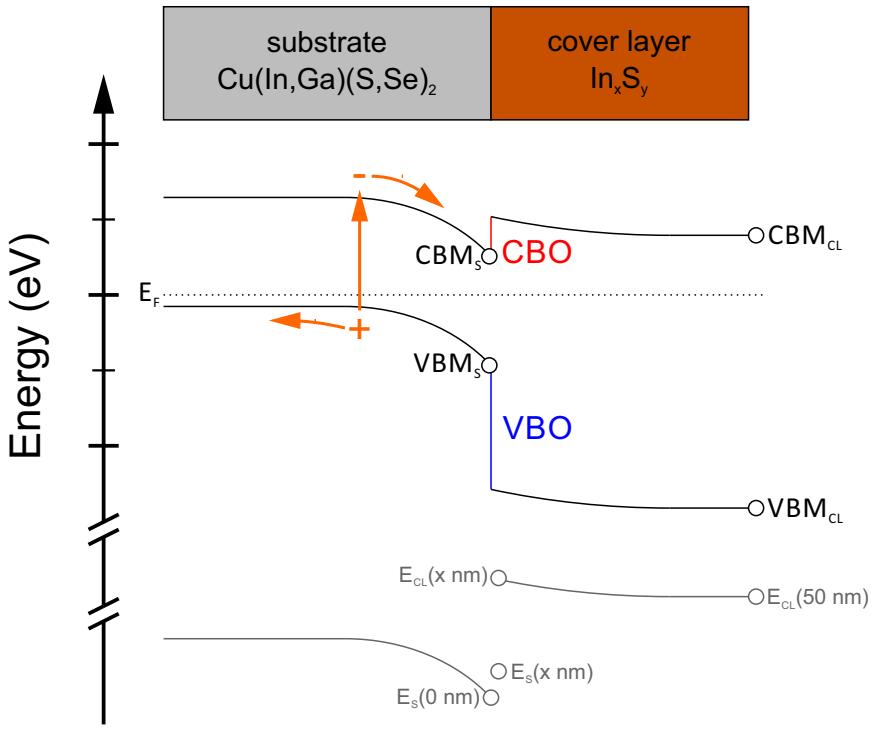

Figure 3.1: Schematic band diagram of the In_xS_y/Cu(In,Ga)$(S,Se)_2$ interface. Circles illustrate the measurements of the valence band maxima (VBM) of the substrate (S) and cover layer (CL) by UPS as well as the conduction band minima (CBM) which are determined by IPES. The notation for the determination of interface induced band bending (see equation 3.2) is also shown. For an effective electron transport, the offset of the conduction band (CBO) should be minimized.

However, it should be considered that the determined valence band edge is possibly not the real one.

Interface induced band bending

In the following it is assumed that the interface is abrupt and that diffusion can be neglected. With the help of the VBM and CBM positions of the respective layers the valence and conduction band offsets at the interface can be estimated. However, these positions are determined for the substrate (S) and the thick cover layer (CL) and positions at the interface might differ due to the differences in interface and surface dipoles. These dipoles affect the band bending in the substrate as well as the cover layer and will be referred to as interface induced band bending (IBB) in the following. The IBB can be determined by monitoring

the shifts of core levels during the interface formation (i.e., for a series of thin cover layer films with increasing thickness). In order to compute the IBB, at least one sample with a thin CL is measured where substrate-related core levels are still detectable. The relative shift of the substrate core levels as well as the relative shift of the cover layer core levels yield the IBB:

$$\mathrm{IBB} = -\left(E_S(0\,\mathrm{nm}) - E_S(x\,\mathrm{nm})\right) + \left(-E_{CL}(x\,\mathrm{nm}) + E_{CL}(50\,\mathrm{nm})\right) \ . \tag{3.2}$$

Here, E_S and E_{CL} are the core level positions of the substrate and cover layer for different film thicknesses (50 nm is here the thickest layer), respectively. The respective energy positions of the used notations are illustrated in Fig. 3.1. For the occupied states positive binding energies are used and for the unoccupied states negative ones. It is desired to measure more than one thin cover layer in order to minimize the error of chemically shifting core levels.

With the valence band maximum and conduction band minimum, the valence band offset (VBO) and conduction band offset (CBO) can be calculated:

$$\mathrm{CBO} = \mathrm{CBM}_S - \mathrm{CBM}_{CL} + \mathrm{IBB} \tag{3.3}$$

$$\mathrm{VBO} = \mathrm{VBM}_S - \mathrm{VBM}_{CL} + \mathrm{IBB} \ . \tag{3.4}$$

A negative value for the conduction band offset is called cliff, a positive offset is called spike, and a vanishing offset is referred to a flat alignment. A cliff is generally attributed to a decrease of the open circuit voltage V_{OC} [53, 55]. In contrast, a spike-like band alignment leads to a loss in the fill factor (FF) and hence in efficiency η [55, 61]. Niemegeers *et al.* [52] argued that electrons can thermally overcome a spike-like barrier of up to 0.2 eV.

3.3 Experimental details

In order to minimize additional surface contamination, all samples were mounted onto the sample holder in a glovebox or glovebag, which was attached to the load lock. Prior to that, the glovebag was evacuated several times and afterwards filled with dry nitrogen 3.0.

All XPS and XAES measurements were carried out in an ultra-high vacuum (UHV) chamber with a base pressure of $< 2 \cdot 10^{-10}$ mbar. The chamber is equipped with a VG CLAM 4 analyzer. A non-monochromatized twin-anode is used as x-ray source providing Mg K_α and Al K_α x-rays. The UPS measurements were performed with a gas discharge lamp using He II or He I. The analyzer was calibrated according to Ref. [62] and for UPS measurements the Fermi edge of a gold foil was set to a binding energy of $E_{Bind} = 0$ eV.

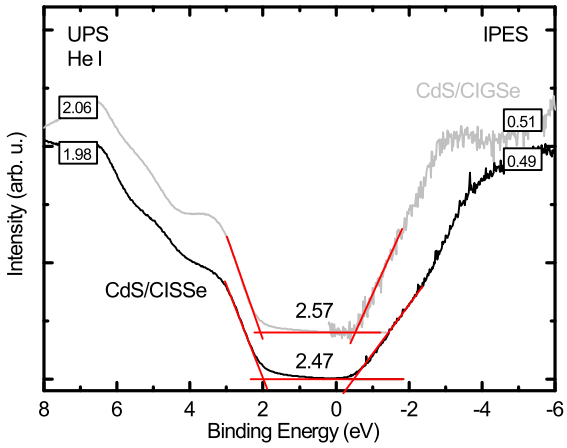

Figure 3.2: UPS/IPES measurements of the CdS/absorber interface for comparison of the IPES detectors. The CdS/CISSe IPES spectrum (black) was measured by the iodine detector while the CdS/CIGSe (gray) was measured by the photomultiplier tube detector. The determined VBM, CBM, and surface band gaps are given in eV. A good accordance between the spectra is detected. The CdS/CISSe spectrum (black) is courtesy of L. Weinhardt.

The IPES measurements were performed with a STAIB NEK 150-1 electron gun (for details see Ref. [63]). The custom-made photon detector uses a photomultiplier (PMP) tube C 9744 from Hamamatsu as photon counting unit. As a band pass, a mercury line filter is utilized which has a center wavelength of 254 nm, i.e., center energy of 4.88 eV (for further details see Refs. [64, 65]). The IPES spectra were calibrated to the Fermi edge of a cleaned copper foil. In total, a resolution of $\leq$ 380 meV and $\leq$ 100 meV could be achieved for IPES and UPS, respectively. In order to compare the IPES spectra, which were measured by the photomultiplier detector with the usually used iodine [66] or acetone [67] detectors (center energy of $\approx$ 9.5 eV) the well-known buffer material CdS was measured with both setups and is compared in Fig. 3.2. The spectral shape of the IPES measurements and the linear extrapolated energy positions of the CBM are in good agreement. However, the UPS determined VBM differ slightly. This can possibly be attributed to different absorber materials, to different deposition procedures, as well as to a different cleanliness of the CdS surface. In general, the shown E_{Gap} are identical within the error bar of $\pm$0.13 eV indicating that band gaps which were measured with the PMP detector are reliable.

The reflective electron energy loss spectroscopy (REELS) measurements were performed in a different chamber in Würzburg which is equipped with a VG ESCALab MK II analyzer. As electron source the electron gun LEG 24 from the rear view LEED Modell 8011 (Thermo VG scientific) was utilized. All experiments were performed at an incident angle of 56 $^\circ$ and

an exit angle of 64 ° (with respect to the surface normal of the sample). The base pressure was $\approx 1 \cdot 10^{-10}$ mbar.

For measuring x-ray emission spectroscopy (XES), a high photon flux is needed, since the cross section of the competing Auger process dominates especially for light elements. This requirements are met at, e.g., the Advanced Light Source (ALS) of the Lawrence Berkeley National Laboratory in Berkeley (California, USA). The here presented XES measurements were performed at the Beamline 8.0 (flux $\approx 10^{15}$ photons/s at $h\nu = 200$ eV). The spectra are recorded at the 8.0.1.1 soft x-ray fluorescence (SXF) endstation with a Roland circle x-ray spectrometer [68, 69]. The XES spectra are energy calibrated with several elastic scattered beams at the sample during the first experimental run in October 2012. For the following experimental runs the spectra were adjusted to fit the ones of the first run. The S $L_{2,3}$ x-ray emission spectra were shifted to align to the spectra from Bär *et al.* [70]. In order to prevent beam-damage, the S $L_{2,3}$ SO_x spectra which are shown in Fig. 6.30 were scanned. These measurements were performed at the solid-state manipulator at the SALSA endstation (open port endstation 8.0.1.2) [71]. All shown x-ray emission spectra were measured in the partial fluorescence yield mode and normalized to the respective ring current.

4

Chalcopyrite-based thin-film solar cells

Thin-film solar cells using chalcopyrite $Cu(In_{1-x},Ga_x)(S_{1-y},Se_y)_2$ (CIGSSe) absorbers have beneficial material properties compared to the currently market-dominating solar cells based on crystalline silicon (c-Si) or polycrystalline silicon (p-Si). Due to the direct band gap of the CIGSSe material [72] the absorption coefficient α is about two orders of magnitude larger than for Si-based solar cells which allows significant thinner absorber thicknesses of about $1-2\,\mu$m [73]. In addition, the band gap of this compound semiconductor can be tuned from 1.04 eV ($CuInSe_2$) up to 2.49 eV ($CuGaS_2$) [74, 75] by varying the composition [76] in order to match the terrestrial sun spectrum. The according theoretical efficiency limit of a single junction solar cell at the earth's surface in dependence of the band gap was first calculated by Shockley and Queisser [77] for a 6000 K black body spectrum. Fig. 4.1 displays the theoretical efficiency limit with respect to the band gap computed for the reference spectrum sun air mass (AM) 1.5 [78]. Please note, AM 1.5 accounts for the longer way of the sun rays through the earth's atmosphere for not perpendicular incidence. This yields a solar intensity of 1000 W/m^2 at the surface. Due to absorption bands in the earth's atmosphere, the theoretical efficiency η exhibits two maxima at 1.15 eV and 1.35 eV with 32.8 % and 33.0 %, respectively. The first band gap maximum is very close to the band gap of $CuInSe_2$.

By tuning the In/Ga and/or the S/Se ratio within the absorber and thus introducing material gradients, even significant higher theoretical efficiencies [80, 81] can be achieved. Already

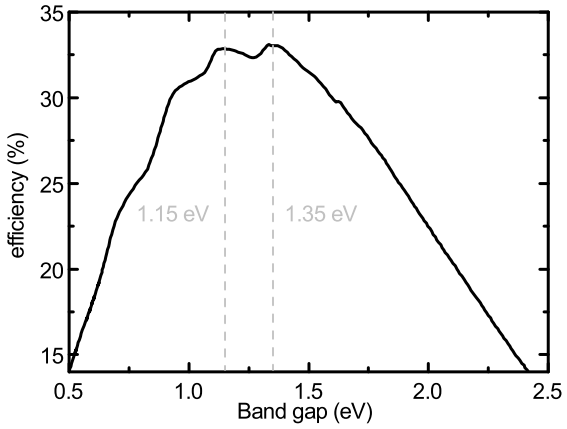

Figure 4.1: Theoretical efficiency η for a solar cell for the terrestrial sun spectrum AM 1.5 in dependence of the band gap. The two maxima are marked with gray dashed lines. Data taken from Ref. [79].

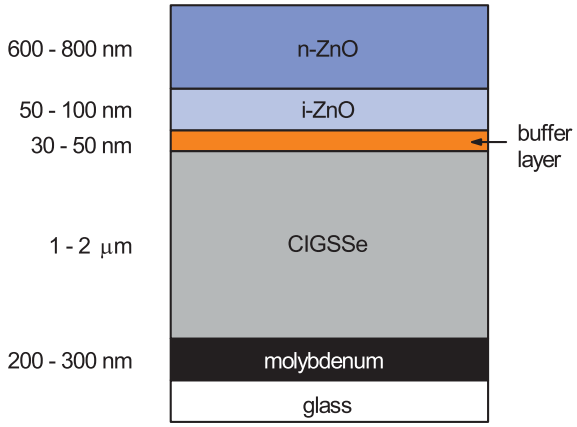

Figure 4.2: Layer stack of a typical CIGSSe solar cell. Each layer is denoted. Layers are not true to scale and typical thicknesses are shown left.

in 1991, Dimmler *et. al* reported "that the surface of CIS has to be highly In rich [(Cu poor), the author] to form reasonable heterointerfaces" [82]. An accompanied characteristic property of the copper-poor surface is the widening of the surface band gap. Thus, the p-type absorber becomes inverted at the surface. This means that the conduction band minimum is close to the Fermi level at the interface (i.e., the valence band maximum is far away). Here, the bulk minority carriers (electrons) become majority carriers at the surface and thus interface recombination is minimized [53].

The relative simple preparation technique for chalcopyrite-based absorbers and the promising potential for reduced costs due to large-scale production are reasons why CIGSSe-based solar cells are very attractive for mass production [83, 84]. A typical CIGSSe solar cell consists of a characteristic multi-layer structure, which is similar in most chalcopyrite-based solar cells. Such a multi-layer structure is illustrated in Fig. 4.2. The chalcopyrite based absorber is grown on a molybdenum (back contact) covered soda lime float glass as substrate (flexible polymer films [85] or metal foils [86, 87] as substrate have also been used). The CIGSSe is covered by a few nanometers thick buffer layer. As transparent front contact, a ZnO layer is used, consisting of a not-deliberately doped i-ZnO and an (aluminum) doped n-ZnO.

4.1 The Cu(In,Ga)(S,Se)$_2$ absorber

All absorbers investigated in this thesis were processed at the pilot line of the "AVANCIS GmbH" (till 2001 "Siemens Solar" and from 2001 - 2006 "Shell Solar") in Munich. The schematic process sequence of the AVANCIS pilot line is shown in Fig. 4.3.

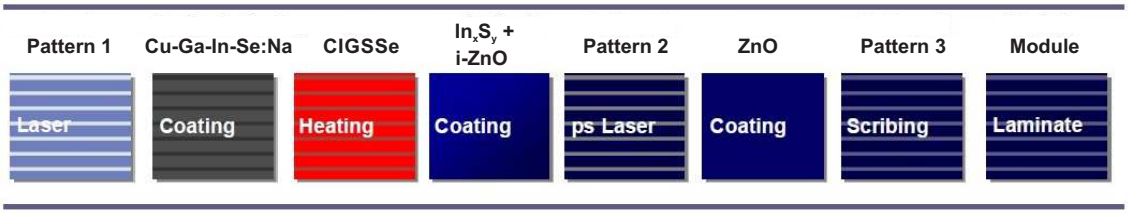

Figure 4.3: Schematic drawing of the AVANCIS pilot line process sequence. Picture adapted from Ref. [6].

A special soda lime float glass with a high strain point serves as substrate. The glass is covered with an alkali barrier (SiN-based) preventing the uncontrolled diffusion of sodium from the glass into the absorber [88]. The Na content is an important parameter for the growth of the absorber. In fact, it promotes the formation of large grains [89] and increases the conductivity via an increasing hole concentration [90] as compared to Na-free films. For reproducibility, a controlled amount of Na is provided during the growth of the absorber. The back contact consists of a molybdenum layer stack and is optimized for a good ohmic contact [6]. Subsequently, the sodium dopant and several alternating layers of Cu-In-Ga are deposited by DC-magnetron sputtering. A selenium layer is thermally evaporated on top of the Cu-In-Ga layers. Afterwards, the layer stack is heated by infra-red lamps in a sulfur-containing atmosphere to a maximal temperature of 600 °C with heating ramps of about 10 °C/s. During this rapid thermal process (RTP) the poly-crystalline CIGSSe phase is formed. The described process is called SEL-RTP (**s**tacked **e**lemental **l**ayer – **r**apid **t**hermal **p**rocess). The process steps in Fig. 4.3 labeled with "Pattern 1, 2, and 3" are introduced to form an internal serial connection. A more detailed description of the process can be found elsewhere [91–93].

As shown in Fig. 4.4, a gradient profile develops during the SEL-RTP. The gallium and sulfur gradients within the absorber are known to improve the solar cell performance. In general, Ga and S increase the band gap. The Ga-gradient towards the back contact develops an electrical field accelerating electrons towards the p-n junction and thus the interface recombination at the back interface is reduced [81, 94]. Furthermore, Ga reduces the defect density concentration in CIGSSe absorbers [95]. By adding sulfur, the energy distance of

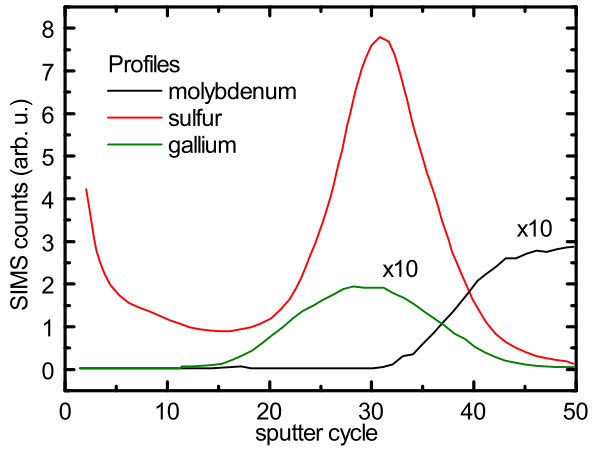

Figure 4.4: SIMS depth profile of a CIGSSe absorber from the AVANCIS pilot line. The Ga and Mo intensities are magnified by a factor of 10. Data taken from [91].

the valence band maximum with respect to the Fermi level is reduced and that of the conduction band minimum is increased [74]. The gradient towards the absorber surface increases the inversion at the surface due to a larger surface band gap and thus the interface recombination is reduced [53]. From the depth-profile analysis in Fig. 4.4, it becomes evident that the surface of the AVANCIS CIGSSe absorber is Ga-free. This is in accordance with several publications [8, 96, 97]. Thus, the surface will be named CISSe in this thesis.

After the thermal process is conducted on the absorber, it is necessary to let the absorber cool down. Subsequent, the p-type absorber is coated with an n-type buffer layer. The demands on the buffer layer will be explained in more detail in section 4.2. Afterwards, the transparent ZnO front window, consisting of an intrinsic ZnO (i-ZnO) and an aluminum doped ZnO (n-ZnO) layer stack, is deposited. Finally, the solar cell is encapsulated protecting the solar cell from environmental influences.

4.2 The buffer layer

It is commonly accepted that a buffer layer is needed for high efficiencies in chalcopyrite-based solar cells [98] and many positive aspects are ascribed to it. The buffer has to fulfill several demands, in particular it has to be

- n-type in order to form the p-n junction with the p-type absorber
- transparent for the range of the solar spectrum to minimize absorption [99]

- create a good band alignment between absorber and front contact [100]
- enhance the inversion at the absorber surface [53]
- protect the absorber from sputter-induced damage during the (sputter) deposition of the front contact [101]
- prevent shunt paths of pin-holes between back and front contact (a certain thickness of the buffer is a necessity) [102]
- enable lattice matching at the buffer/absorber interface to prevent structural defects [103]
- in some cases clean the absorber surface (during a chemical bath deposition process) [104]

Already in 1974, the first chalcopyrite-like solar cell was buffered with a thermal deposited CdS film [43]. In the following decades, CdS was usually prepared using a chemical bath deposition and achieved the best efficiencies compared to alternative buffer layers. Thus, CdS evolved to the state-of-the-art buffer layer for chalcopyrite-based solar cells. However, cadmium is a heavy metal and thus CdS is not the best choice in terms of cost and environment compatibility. Furthermore, the chemical-bath deposition (CBD) of CdS is the only process step which cannot be included in a vacuum in-line production.

Correspondingly, one of the most challenging task for CIGSSe solar cells is the replacement of CdS by a dry in-line processable and less toxic buffer layer material. Strong efforts have been made to find an alternative buffer layer. Review paper on alternative buffer layers can be found elsewhere [3, 4, 99, 105]. (Zn,Mg)O, Zn(O,S), or In_2S_3 emerged as most promising alternatives. These materials have been processed with a variety of deposition methods, including ion-layer gas deposition (ILGAR) [101, 106, 107], magnetron sputtering [108], CBD [109] and co-evaporation [110]. Despite many promising results on alternative buffer layers, until recently it was not possible to replace the CBD deposited CdS. This had several reasons, e.g., the lower efficiency of alternative buffer layers compared to CdS (called efficiency gap) and the large-scale process stability.

Table 4.1 compares the best efficiencies of different buffered chalcopyrite-based solar cells (and silicon-based solar cells as reference). It has to be stated that the different buffers are grown on different absorbers, the quality of which also influences the efficiency and therefore the value of this comparison is limited. Intensive research on the most promising alternatives was performed and it turned out that indium sulfide is the best-performing alternative for the AVANCIS absorber. In fact, this material system achieves high efficiencies

Table 4.1: Certified efficiencies measured under the AM 1.5 spectrum. Unless otherwise specified the data were taken from Ref. [2].

Classification	laboratory efficiency (%)	large-area efficiency (%)
Silicon		
c-Si	25.6	22.9
p-Si	20.8	18.5
Cu(In,Ga)(S,Se)$_2$		
CdS buffered	21.7 [1]	15.7
Zn(O,S) buffered	20.9 [111]	17.5
In_2S_3 buffered	17.1 [112]	16.6 [111]
(Zn,Mg)O buffered	18.1 [113]	-

and fulfills the requirements for the scalability for industrial demands. Hence, this thesis focuses on indium sulfide as alternative buffer layer for the AVANCIS CIGSSe absorbers.

The In_xS_y and Na:In_xS_y buffer layer

Indium sulfide exists (at room temperature and ambient pressure) in three different phases, i.e., In_2S_3, In_6S_7, and InS [114–116]. In_2S_3 can be found in three modifications: the tetragonal β-In_2S_3 for stoichiometric compositions, a cubic α-In_2S_3 for In-rich compositions, and the γ-modification existing for temperatures above 750 °C. Both, the β- and α-phase have vacant sites which are not completely occupied by indium atoms. However, the cation vacancies of α-In_2S_3 are disordered [117]. The $\beta \rightarrow \alpha$ (order $\rightarrow$ disorder) transition occurs for In-contents of 40.1 % [117] or 40.5 % [118]. In a large region between $\approx$ 41.5 % - 46 % indium content α-In_2S_3 and the monoclinic In_6S_7 coexist. A more detailed description can be found elsewhere [118, 119].

All buffer layers investigated in the framework of this thesis were processed at the AVANCIS pilot line in Munich. The indium sulfide layers were grown by a physical vapor deposition process. Prior to this deposition, the CIGSSe substrate was heated to temperatures below 150 °C. The different buffer layer thicknesses were estimated from the deposition time.

In the scope of this thesis, the integral S/In ratio of the indium sulfide layers and the resulting chemical and electronic properties are a major part and will be discussed in chapter 6. The S/In ratio was adjusted by a proprietary process which is based on the thermal evaporation

of the In_2S_3 compound source material [6]. Thus, the indium sulfide buffer layer is better described as In_xS_y. Furthermore, it has to be stated that In_2S_3 releases a characteristic H_2S smell [120]. This suggests that the surface of In_xS_y becomes sulfur-poor as compared to the nominal S/In ratio. This prediction is confirmed by XPS measurements and will be discussed later.

The properties of In_xS_y thin films depend critically on the admixture of other elements and the deposition method used [121]. Consequently, several publications discuss the influence of doping indium sulfide [122–124], e.g., to widen the buffer band gap in order to tailor the band offset at the buffer/absorber interface. Furthermore, an advantage of a band gap widening is the higher transparency of the buffer layer and thus reducing the absorption of high-energy photons.

It is known that copper and sodium diffuse from the absorber towards the buffer during deposition [70] or upon an additional annealing step [125]. Thus, the incorporation of copper and sodium into In_xS_y becomes attractive for manipulating optical and electronic properties. While an incorporation of Cu leads to a significant smaller band gap and a reduction of the n-type character, doping In_xS_y with Na increases the band gap [126]. In fact, the band gap can be varied between 2.15 and 2.90 eV by adding sodium. Despite this large change, all films are n-conducting [124]. Another inevitable contaminant/dopant is oxygen from the residual gas in the evaporation chamber. Oxygen also has the benefit of increasing the band gap of In_xS_y up to 2.9 eV (for a doping concentration of 8.5 atom percent (at.%)) while the films remain n-conductive [127]. However, since indium sulfide is hygroscopic and the evaporation takes place in a non-clean environment (from a surface scientist's perspective), doping with oxygen is not controllable. Thus, doping of Na into In_xS_y is very attractive. The latter is realized by a thermal co-evaporation of a Na compound and In_2S_3 [6]. In the following, the resulting layer is named Na:In_xS_y.

Sodium doping into In_xS_y is very important in order to close the efficiency gap towards CdS-buffered solar cells. A further optimization of these films calls for a fundamental understanding of their electronic and chemical properties. An in-depth study of these properties will be presented in chapter 6.2.

5

Impact of environmental conditions on the CISSe surface

The impact of environmental conditions on a solar cell absorber during the production is an important aspect in the run to achieve highest efficiencies. In fact, for the production of high efficient solar cell absorbers the exposure to the ambient environment or bad vacuum conditions lead to a significant amount of surface adsorbates which may act as recombination centers at the buffer/absorber interface. For the case of the CdS buffer layer, this is probably not so critical as it is generally known that the CdS-CBD process removes adsorbates from the absorber surface reducing the defect density at the interface and thus the interface recombination rate [7, 104, 128].

However, the replacement of CdS as buffer material by a vacuum-deposited dry buffer has extensive consequences because the "natural" surface cleaning step provided by the chemical bath is not conducted anymore. Accordingly, adsorbates, oxidation, and segregation of absorber elements have to be taken into account. Indeed, several studies confirm degradation effects, e.g., decreasing carrier lifetimes of the full device after exposing the absorber to air on the minute timescale [128]. Moreover, changes of the electrical properties of chalcopyrite absorbers after annealing in oxygen [129, 130] and storage in damp heat have been published [131]. In addition, photo-induced oxidation [132] as well as oxidation induced

by ambient environments [133, 134] and the formation of sulfates at the water/absorber interface [135] have been found.

In order to study the time-dependent degradation of a CISSe surface, a $(10 \times 10)\,\mathrm{cm}^2$ absorber sample was cut into several pieces and each was stored under one of three different environmental conditions for different storing times up to 14 days. At the University of Würzburg, one set was kept in a glovebox under dry nitrogen atmosphere (NA) (room temperature (RT); $O_2 < 0.1$ ppm; $H_2O < 1.0$ ppm), while a second set was stored under ambient air conditions (AA) (RT; approx. 45 % rel. humidity). The third set was stored at AVANCIS in Munich under damp heat (DH) conditions (85 °C; 85 % rel. humidity). The DH conditions are standardized by the international electrotechnical commission (IEC 60068-2-78) and are often used to accelerate aging processes [131, 136]. The absorbers were transported in a sealed bag which was filled with N_2.

5.1 Impact on the chemical surface composition

To reduce an additional oxidation during the transfer from the treatment environment to the vacuum chamber, each absorber piece was investigated once.

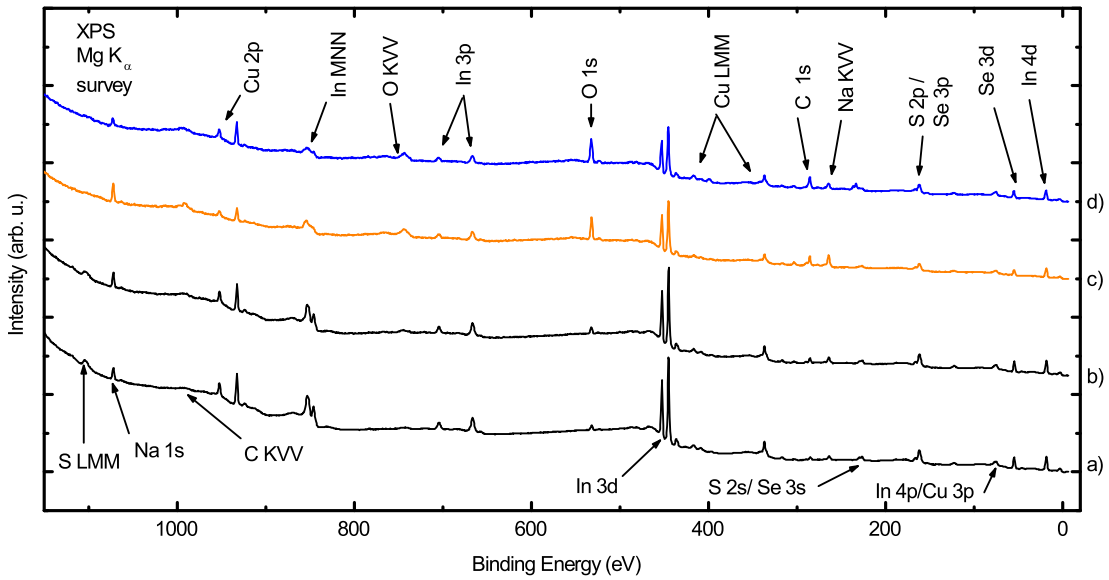

Figure 5.1: XPS survey spectra of the a) as-received absorber and the absorber after 14 days in b) nitrogen atmosphere, c) ambient air, and d) damp heat environment. Photoemission and Auger signals are labeled.

Fig. 5.1 shows the XPS survey spectra of the as-received (pristine) absorber a) and after exposing the absorbers to three different environmental conditions b)-d) for 14 days. All expected photoemission signals, i.e., the absorber elements can be found and prominent core level lines and Auger features are labeled. Compared to the pristine absorber, the other spectra show significant changes which can be related to the increase of the O 1s and C 1s signals and thus decreasing signals of all absorber-related elements. In the following, a detailed investigation of the chemical structure of the absorber as a function of time will be given. For this purpose, the XPS intensities of absorber and adsorbate elements were evaluated. The increase of adsorbate signals is depicted in more detail in Fig. 5.2. After 14 days of storing the absorber in NA, the O 1s a) and C 1s b) signals increase only slightly compared to the as-received sample. In contrast, after 14 days at AA and DH conditions the O 1s peak is increased by a factor of 6 and 7, respectively. Moreover, additional intensity at higher binding energies appears, which can be assigned to more oxygen species, e.g., adsorbed water at 533.7 eV binding energy [137]. For the C 1s signals, a similar intensity increase can be detected. The NA treatment causes only a small increase of the signal, whereas the AA and the DH treatment induce a large increase of the C1s photoemission line. The C 1s consists of two regions: the main intensity belongs to carbons and hydrocarbons ($\approx$ 284 - 287 eV) [138, 139] and the additional intensity at $\approx$ 288.5 - 292 eV, [90, 140] can be assigned to carbonates. A significant increase of the carbonate intensity is only found for the AA treatment.

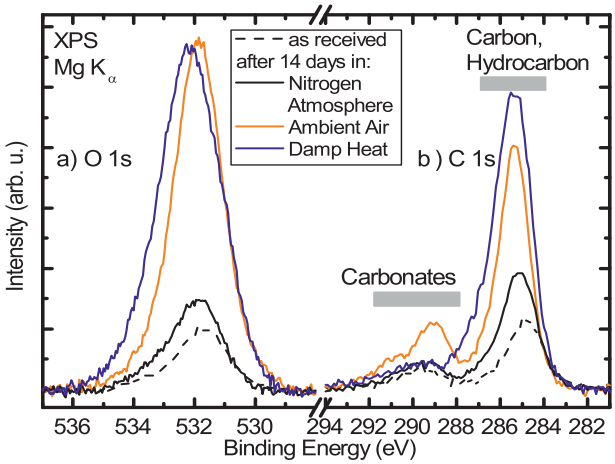

Figure 5.2: Detailed XPS spectra of a) O 1s and b) C 1s of the untreated sample (dashed black line), and after 14 days of NA (black), AA (orange), and DH (blue). Gray bars indicate the energy ranges found for carbonate and hydrocarbon species [90, 138–140]. Graph reprinted with permission from Hauschild *et al.*, J. Appl. Phys. **115**, 183707 – 183707–5 (2014). Copyright (2014), American Institute of Physics.

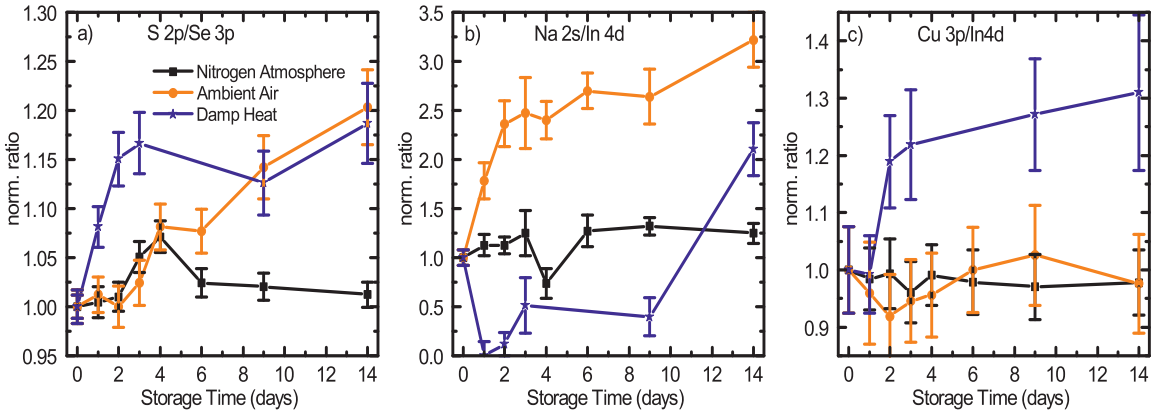

Figure 5.3: Different normalized surface ratios as a function of treatment time. a) S 2p/Se 3p, b) Na 2s/In 4d, and c) Cu 3p/In 4d. The copper error bar is larger than the others due to the energetically overlapping signals of Cu 3p and In 4p. Graphs reprinted with permission from Hauschild *et al.*, J. Appl. Phys. **115**, 183707 – 183707–5 (2014). Copyright (2014), American Institute of Physics.

In addition, the line intensities of selenium- and indium-related core levels show different behaviors for the three treatments. For the NA storage the absolute line intensity remains constant while for AA and DH treatment a small decrease is observed. This decrease is consistent with an expected attenuation of a carbon and oxygen contamination layer which suggests that the indium and selenium concentration at the surface remains constant. Hence, indium and selenium are used as reference for the different surface ratios which are depicted in Fig. 5.3.

Sulfur

The nitrogen atmosphere does not significantly alter the S/Se ratio (within errors), except for the samples of the third and the fourth day (Fig. 5.3 a)) which likely can be explained with inhomogeneities of the absorber plate. The damp heat treatment significantly increases the sulfur content by about 15 % within the first two days. A longer treatment shows no additional effect and the ratio stays constant. Finally, for the ambient air treatment an analog increase can be observed but the increase does not start until the fourth day.

Sodium

Similar to sulfur, storing the samples in NA only leads overall to a slight increase of the sodium concentration (except of day four for which a decrease is observed, see Fig. 5.3 b)). In contrast to this, the AA and DH show a complete different behavior. Under AA, the sodium is increased by 150 % after the first three days and rises to more than a factor of three after 14 days. For the treatment under damp heat conditions an opposite trend is observed. Already after the first day the sodium is almost completely vanished. (The Na 2s disappears in the noise. However, a very small Na 1s signal is detectable.) It returns after the second day and further increases to about twice of the starting amount after 14 days.

The observation made for these different storing conditions can be explained to be due to the humidity present under the latter two storing conditions. In fact, humidity-induced sodium diffusion towards the surface is in accordance with the finding of Braunger *et al.* [141]. This explains the strong growth of the sodium signal at the surface for the AA treatment as well as the slight increase in the nearly humidity-free NA environment. For the DH treatment the time-dependent trend of the sodium concentration at the surface can possibly be explained by a condensation of humidity at the surface leading to a dissolvation of the Na. A similar behavior is known when chalcopyrites are dipped into water [96]. Subsequently, the humidity of the DH treatment promotes the diffusion of Na from the bulk towards the surface.

To identify the chemical surrounding of the sodium atoms, the modified sodium Auger parameter α'_{Na} (see section 2.1) was computed. Fig. 5.4 illustrates the modified Auger parameter of sodium for the three treatments (NA, AA, and DH) as a function of treatment duration. The error bars originate mainly from the uncertainty of the determination of the position of the Auger peaks. Due to a small sodium signal, the error bar is larger for the DH treatment. For the NA, a small continuous decrease of α'_{Na} from (2061.84 ± 0.07) eV by approximately 0.4 eV after 14 days is detected. This process can be explained by the residual humidity in the glovebox leading to the observed decrease of α'_{Na} due to oxidation of sodium. In contrast, the AA environment leads to an abrupt decrease by ≈ 0.6 eV after the first day. Afterwards, the modified Auger parameter stays constant within the error bar during the remaining 13 days. For the DH treatment α'_{Na} drops by ≈ 1 eV within the first three days. Afterwards α'_{Na} increases to roughly the same value (2061.5 ± 0.1) eV as for NA and AA storage. In general, a decrease of α'_{Na} is assigned to oxidation of sodium partners [7, 25, 90, 139, 141, 142]. The fact that the three different storing treatments lead to a common final α' value suggests that the same sodium surface compound is formed. According to Fig.

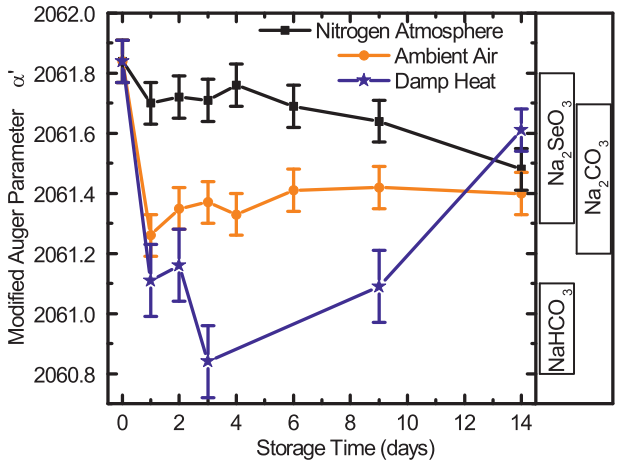

Figure 5.4: Modified Auger parameter α' of sodium for the three different storage conditions as a function of storage time. Expected values of α' are marked in the right panel as guide to the eye [7, 25, 90, 139, 141, 142]. Graph reprinted with permission from Hauschild *et al.*, J. Appl. Phys. **115**, 183707 – 183707–5 (2014). Copyright (2014), American Institute of Physics.

5.4 the Auger parameter of $\alpha'_{Na} = (2061.5 \pm 0.1)$ eV can either be attributed to Na_2SeO_3 or Na_2CO_3.

Since for all treatments (at least) a small increase of the carbonate-related peak occurs (see Fig. 5.2 b)), the sodium surface compound is tendentially assigned to Na_2CO_3 (sodium carbonate). This assignment is further supported by the prominent increase of the carbonate-related peak which is accompanied by a strong increase of the sodium line intensity for the AA treatment (Fig. 5.3 b)). Despite sodium being an important parameter for the performance of a solar cell, the creation of sodium carbonate may act as recombination center for charge carriers at the subsequent buffer/absorber interface.

Furthermore, for the DH treatment the dissolving of sodium is accompanied with the initial drop of the modified sodium Auger parameter. The remaining Na is strongly oxidized (Na_2HCO_3). Within the second day the Na/In ratio starts to rise which is assigned to humidity-induced diffusion of Na towards the surface.

Copper

As seen from Fig. 5.3 c), the copper concentration stays constant within the error bar for the low and medium humidity environments (NA and AA, respectively).

In contrast, within the first three days of the DH treatment an increase in the copper concentration of about $\approx$ 20 - 25 % is measurable. The continued treatment has no further effect on the concentration. The increase of the copper concentration at the surface may lead to a reduction of the surface band gap widening [8, 143, 144] and thus to a potentially bad band alignment of the future interface.

5.2 Surface oxidation of absorber elements

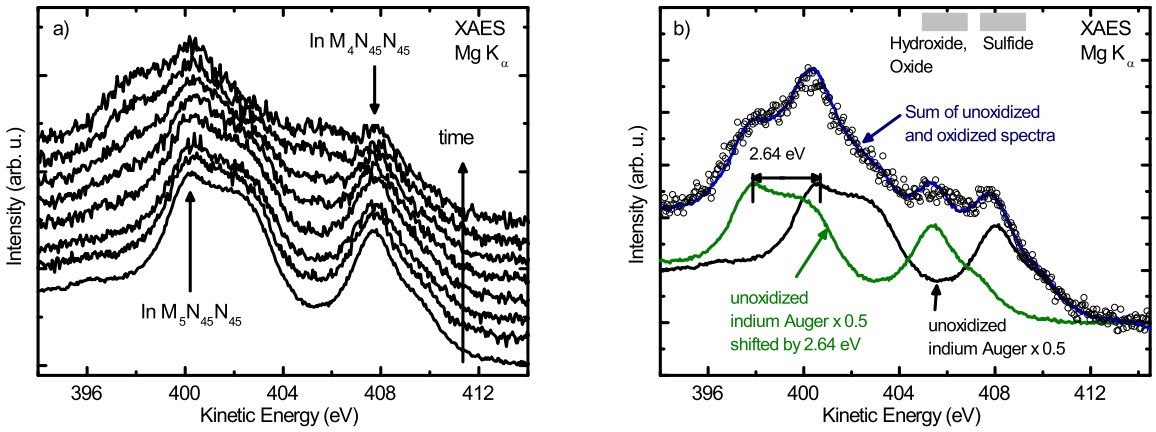

Figure 5.5: a) Indium MNN XAES spectra for the ambient air treatment. Two additional features appear at 405 eV and 398 eV kinetic energy as a function of time. b) 14 day's spectrum of the AA treatment (black circles). The spectrum can be reproduced (blue line) by the sum of the untreated indium Auger spectrum (non-oxidized, black line) and a shifted component representing the oxidized indium (green line). The gray bars illustrate kinetic energies of sulfides, oxides, and hydroxides commonly found in literature [7, 62, 138, 145]. Graphs reprinted with permission from Hauschild *et al.*, J. Appl. Phys. **115**, 183707 – 183707–5 (2014). Copyright (2014), American Institute of Physics.

Besides the (sometimes strong) changes of the surface composition, an oxidation of indium, copper, and selenium is observed as will be discussed in the following. In order to determine the degree of the indium oxidation, the In MNN Auger transition was analyzed. Fig. 5.5 a) exemplarily shows the In MNN of the absorber for the AA storage. The bottom spectrum reveals the non-oxidized indium Auger intensity, consisting of the $M_5N_{45}N_{45}$ and $M_4N_{45}N_{45}$ transitions. Two features appear at 405.3 and 397.5 eV with increasing storing time, which can be related to an oxidized indium species. This is illustrated exemplarily in Fig. 5.5 b) for the sample which was stored for 14 days in AA. The 1:1 sum (blue line) of the non-oxidized (black line) and the identical spectrum (shifted by 2.64 eV) (green line) reproduces the 14 day's spectrum (black dots). A literature survey assigns the shifted component to oxidized indium (most likely In_2O_3[7]). Thus, after 14 days in AA the indium oxide fraction is $(50.0 \pm 4.5)\,\%$. Reiterating this procedure for all environments leads to Fig. 5.6 a). It is found that the NA treatment leads to no oxidation. During the 14 days of AA treatment, a continuously increasing amount of indium surface oxides can be observed.

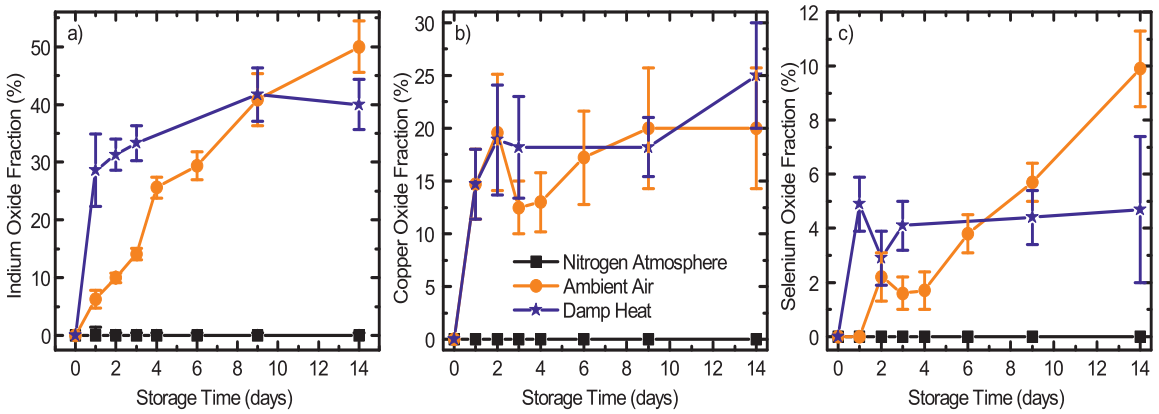

Figure 5.6: Oxide fraction for a) indium, b) copper, and c) selenium in percent of absorber components for the three storage environments. Graphs reprinted with permission from Hauschild *et al.*, J. Appl. Phys. **115**, 183707 – 183707–5 (2014). Copyright (2014), American Institute of Physics.

The DH treatment leads to a faster increase within the first day ($\approx 29\,\%$) but saturates for the subsequent treatment time. After 14 days the indium oxide fraction stays at about 40 %.

To extract the copper oxide fraction the Cu $L_3M_{45}M_{45}$ Auger line was analyzed by using a corresponding procedure to the one which was described for the In MNN Auger transition. The calculated result is shown in Fig. 5.6 b). Again, no oxide is detected for the NA storage, while AA and DH show similar behaviors. Both treatments lead to a rapid increase of the oxide fraction within the first two days and then do not show further changes.

In order to identify whether copper exists as Cu(II) (e.g., CuO) or as Cu(I) (e.g., Cu_2O) the Cu $2p_{3/2}$ and Cu $L_3M_{45}M_{45}$ signals are analyzed in the following. In Fig. 5.7 a) and b) the untreated absorber and the absorber after 14 days of AA treatment is shown, respectively. After fitting the two Cu $2p_{3/2}$ spectra with Voigt profiles, with the same width and shape, a clear additional peak occurs at higher binding energies for the AA treated sample (Fig. 5.7 b)). To clarify, which oxid is formed, Cu_2O and CuO reference spectra are plotted in Fig. 5.7. In the CuO reference spectra, two features occur at about 943 eV and 933.2 eV, which originate from different final states in the photoelectron process, while for Cu_2O only one final state exists. This can be explained as followed: in the ground state, CuO is in a $|c3d^9L\rangle$ and Cu_2O in a $|c3d^{10}L\rangle$ configuration. Here c denotes the core level, $3d$ the d-shell, and L the occupied 2p oxygen ligand shell. In the CuO case, the photoexcited core hole pulls the unoccupied d-level and an unoccupied copper sp-band down below the top of the ligand shell L. Due to screening of the core hole, a charge transfer from the occupied L shell into the Cu sp-band may occur (the $3d^9$ ground state is approximately intact (satellite

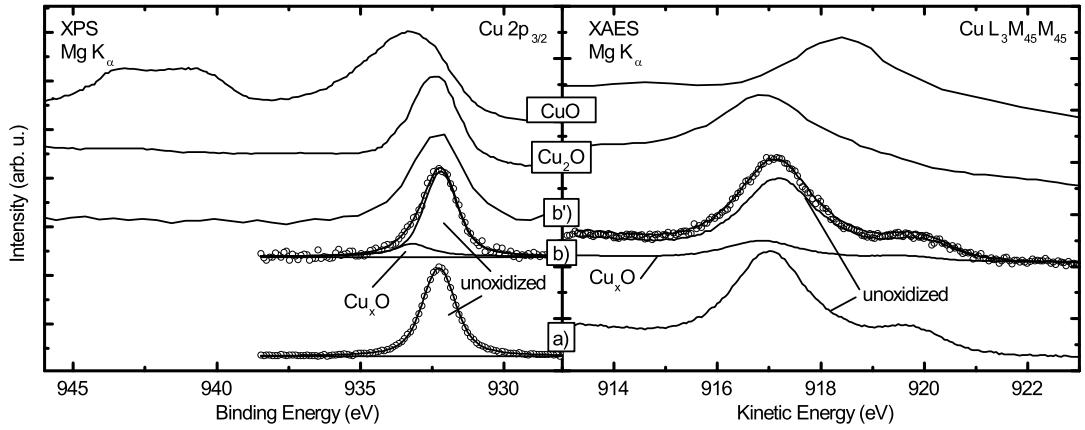

Figure 5.7: The left panel shows the Cu $2p_{3/2}$ and the right panel the Cu $L_3M_{45}M_{45}$ features. a) untreated CISSe absorber, b) CISSe absorber after 14 days under AA, the spectrum (circles) consists of an unoxidized and an oxidized component, b') same sample as shown in b), but extracted from the survey spectrum. The Cu_2O and CuO reference spectra are taken from Ref. [146].

structure)). The structure in the satellite line is due to a multiplet splitting of the 2p and 3d final state [146]. A second final state occurs due to screening by charge transfer from the ligand shell L into the Cu d-shell, leading to a $|c^{-1}3d^{10}L^{-1}\rangle$ configuration (main peak). In contrast, since the d-shell of Cu_2O is filled, only the main spectral line is observed.

By comparing the CuO spectrum with the 14 days AA treated sample (Fig. 5.7 b')) it occurs that no satellite structure is present. (Fig. 5.7 b') was extracted from the survey spectrum which was measured with an analyzer pass energy of 50 eV and therefore the resolution is not as good as for the detailed spectrum b).) In Fig. 5.7 b), Cu_xO is about 20 % of the copper signal and the satellites of CuO have a relative intensity of 0.55 [146] of the main peak. Hence, a Cu_xO satellite intensity of about 10 % of the Cu $2p_{3/2}$ peak is expected. In contrast, no satellite-related signal is observed in spectrum b'). Furthermore, the Cu LMM spectrum of CuO is significantly different to those of CISSe and additionally the Cu_2O reference Auger spectrum resembles the 14 days AA sample. Thus, the copper oxid which is created during the storing process can be identified as Cu_2O.

The selenium oxide fraction was determined by using the Se 3d and the additional SeO_x component at accordingly higher binding energies [62, 133]. The result is depicted in Fig. 5.6 c). Similar to the other absorber elements, no oxidation was found for the NA storage. For AA and DH the oxide fraction is found to be a function of the storage time. Again, the DH treatment causes an increase within the first day to ≈ 4.5 % and subsequently it saturates

at this value. In contrast, the AA treatment leads to a delayed but steady increase over the duration of the treatment. After 14 days an Se oxide fraction of about 10 % is measurable.

To summarize, it can be stated that for a humidity-free environment (nitrogen atmosphere) neither changes of the CISSe surface stoichiometry nor oxidation of absorber elements were found. In contrast, for humidity-containing environments (ambient air and damp heat), significant changes of the surface stoichiometry and strong oxidation of absorber elements were monitored as a function of the presence of water and oxygen. The modifications of the surface stoichiometry may lead to a change of the absorber surface band gap, e.g., a copper accumulation at the surface might decrease the surface band gap. For the damp heat conditions, indium exhibits the biggest oxide fraction (50 %), followed by copper (25 %), and selenium (10 %). The presence of oxides at the buffer/absorber interface tentatively increases the recombination probability of charge carriers. In addition, it is believed that oxidation at an absorber surface has a negative effect on the band bending, e.g., the reduction of the surface charge carrier type inversion [130, 147] (here, no aging-induced band bending was observed). Hence, the environmental conditions have a huge impact on the chemical properties of the CISSe surface and therefore humidity and/or oxygen containing environments should be avoided during the storage or the solar cell production process.

6

Interfaces in the CIGSSe thin-film solar cell

Indium sulfide buffers have emerged as one of the most promising alternatives for CdS buffers for CIGSSe solar cells. Accordingly, a variety of studies were published, e.g., [148–152]. However, significant variations of the film properties can be found therein. In fact, for a single crystal a band gap of 2.0 eV is reported whereas for different deposition methods In_2S_3 thin films yield a wide range of band gaps, starting from 2.0 eV up to 2.8 eV [150, 152–154]. Though direct as well as indirect transitions are reported, all of these films are n-conductive. An important aspect of In_2S_3 is the dependence of its conductivity on the sulfur concentration. To be more precise, a lack of sulfur increases the n-type character [153, 155]. Furthermore, the best-performing indium sulfide devices are exposed to temperatures of (at least) about 200 °C during the preparation process [10]. Several groups observed a strong copper and sodium diffusion from the absorber into the buffer upon such a thermal treatment [70, 125, 156, 157].

Overall, independent on the deposition technique used it is not entirely clear why In_2S_3-buffered solar cells are performing so well. In this context, it is surprising that negative conduction band offsets are determined at the In_2S_3/absorber interface. In fact, Schulmeyer *et al.* [158] found for the In_2S_3/$CuGaSe_2$ interface a cliff-like CBO of (-0.56 ± 0.10) eV and Sterner *et al.* [150] found for In_2S_3/CIGSe a CBO of (-0.45 ± 0.20) eV. However, these

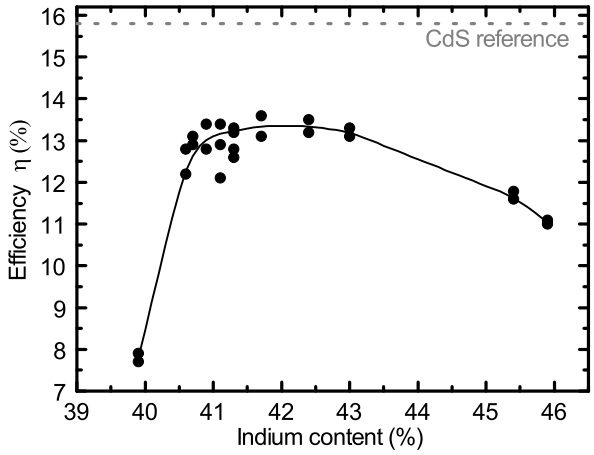

Figure 6.1: Solar cell efficiency η on laboratory scale of the In_xS_y buffered solar cell for different indium contents (data points). A guide to the eye (black line) highlights a distinct maximum at about 42 %. As a comparison, the most efficient CdS buffered cell is plotted as a gray dashed line. Data points provided by S. Pohlner [159]. Error of the indium content about 0.3 % and η about 0.1 %.

studies used an indirect approach to determine the conduction band minimum by measuring the valence band maximum at the surface (with XPS) and calculating the CBO using the bulk-sensitive optical band gap. This approach is especially problematic in real samples like the investigated thin film solar cells, in which the properties (including the band gap) at the surface significantly differ from the bulk (see, e.g., [8, 9])

In the scope of this chapter, the In_xS_y/CISSe interface is investigated to understand the conversion efficiency dependence on the *nominal* S/In ratio of the indium sulfide films which is illustrated in Fig. 6.1. Correspondingly, buffer layers with different S/In ratios were investigated in terms of the chemical properties by means of the surface-sensitive XPS, XAES, and bulk-sensitive XES. Furthermore, the conduction band offset in dependence of the S/In ratio was directly measured using a combination of UPS and IPES resulting in a detailed picture of the chemical and electronic properties of the In_xS_y/CISSe interface.

6.1 The In_xS_y/CISSe interface

In order to get insight into the properties of the In_xS_y/CISSe interface as a function of the S/In ratio, sample series with x = 40.2 %, 41 %, 42 %, and 43.2 % were processed. In each sample series, buffer layers of different thicknesses (i.e., very thin films, for which the substrate lines can still be detected by XPS and a sample of full thickness) were prepared. The full thickness samples have a thickness of 50 nm for x = 40.2 %, 80 nm for x = 41 %, 50 nm and 80 nm for 42 %, and 50 nm for 43.2 %. After the initial data sets were taken, the thickest buffer layer sample was annealed for 30 min at $(100 \pm 3)\,^{\circ}$C and for another 30 min at $(200 \pm 2)\,^{\circ}$C in UHV to reflect the impact of heat treatments by subsequent process steps.

6.1.1 Chemical properties in dependence on the nominal S/In ratio

Due to the large number of samples and correspondingly the large number of survey and detailed spectra, only the spectra of the best-performing In_xS_y (x = 42 %) sample series are exemplary outlined in the following. However, where necessary, selected spectra with different S/In ratios are compared. Finally, numerical results extracted from the data for all samples are shown and discussed.

All samples show a small amount of oxygen- and carbon-related signals in the XPS survey spectra. It should be noted that the pure CISSe absorbers exhibit the highest amount of oxygen and carbon throughout all sample series. With increasing buffer layer thicknesses, the amount of C 1s and O 1s signal decreases which can be explained by the long storage time of the absorbers at AVANCIS whereas the samples with increasing buffer layer were measured shortly after deposition.

Fig. 6.2 shows the low binding energy region of the pristine absorber and of the buffer/ absorber samples with increasing In_xS_y (x = 42 %) buffer layer thickness. As a reference a co-evaporated In_2S_3 spectrum is shown (gray spectrum, topmost) where the In 4d was aligned to the 50 nm In_xS_y In 4d signal. In this spectrum, the In 4p signal which overlaps energetically with the Cu 3p can be identified. With increasing In_xS_y thickness the indium-related signals increase, whereas the copper and selenium signals decrease, e.g., only small buffer-related signals are visible for 6 nm buffer layer thickness. The Se signal of the 9 nm buffer layer sample exhibits about (2 ± 1) % of CISSe Se 3d intensity. Taking the large IMFP λ of about 2.5 nm in this energy region into account (the relative variation between the IMFP of Cu 3p and In 4d is smaller than 4 %) [160], this result suggests that the overlayer

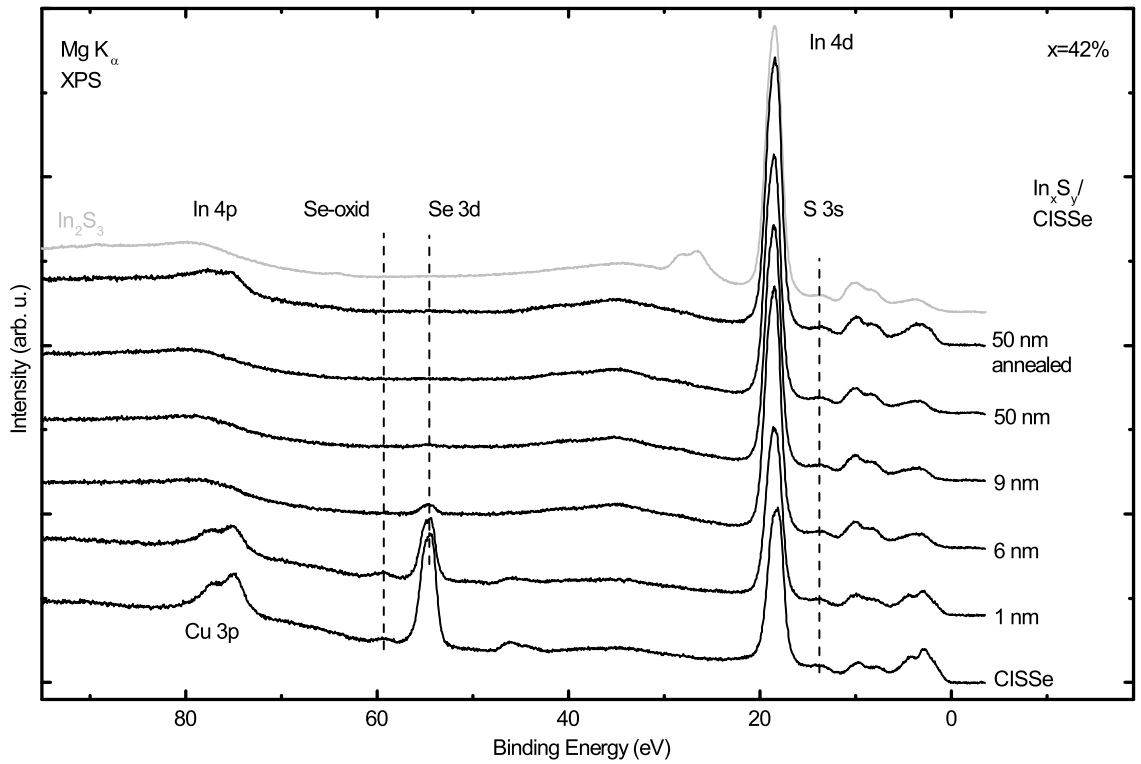

Figure 6.2: Mg K_α excited XPS spectra in the low binding energy region of a CISSe absorber, the buffer/absorber samples with increasing buffer layer thicknesses, and an annealed In_xS_y/CISSe sample. The gray spectrum corresponds to a co-evaporated In_2S_3 reference (topmost). XPS signals are labeled.

is closed and that upon deposition of the In_xS_y buffer layer no strong diffusion of absorber elements occur. The similarity between the 9 nm and 50 nm spectra of In 4d (Fig. 6.2) and S 2p (Fig. 6.3) serves as further indication that the overlayer is closed for thicknesses larger than ≈ 10 nm. After annealing of the 50 nm In_xS_y/CISSe sample a clear copper diffusion is observed (see Fig. 6.2), which is displayed by the reappearing Cu 3p signal. In contrast, no selenium signal is detected. The latter result rules out a possible inhomogeneous film, e.g., formation of islands and/or the desorption of the complete film.

For a further qualitative evaluation, the detail spectra of Na 1s, Cu $2p_{3/2}$, and S 2p/Se 3p are combined in Fig. 6.3. A linear background was subtracted for all spectra. With increasing buffer layer thickness, the S 2p peaks (163 eV and 162 eV for S $2p_{1/2}$ and S $2p_{3/2}$, respectively) increase in intensity while the Na 1s, Cu $2p_{3/2}$, and Se 3p (166.5 eV and 160 eV for Se $3p_{1/2}$ and Se $3p_{3/2}$, respectively) signals decrease. No indication for a formation of SO_x was found. Due to the small IMFP of Na 1s ($\lambda = 0.7$ nm [160]) and Cu $2p_{3/2}$ ($\lambda = 0.9$ nm

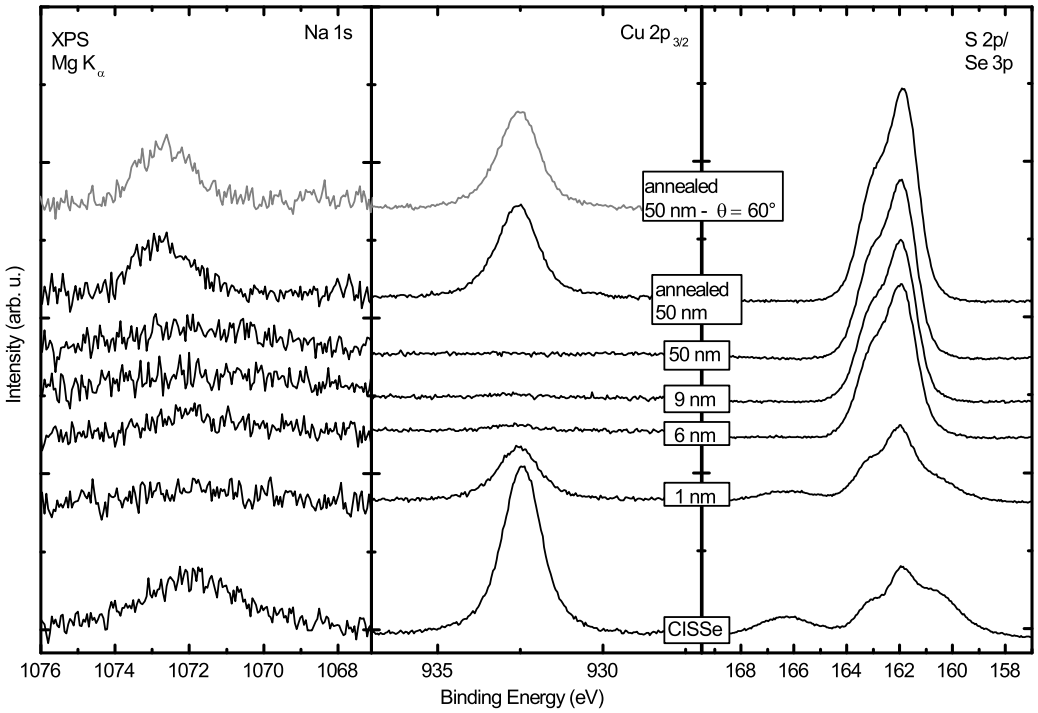

Figure 6.3: Na1s, Cu $2p_{3/2}$, and S 2p/Se 3p XPS spectra of a CISSe absorber surface, In_xS_y/CISSe samples with varying buffer layer thicknesses, and the 50 nm In_xS_y/CISSe sample after annealing at 200 °C. The gray spectra show the annealed Na1s and Cu $2p_{3/2}$ signals at grazing emission ($\theta = 60\,°$).

[160]) the intensity should attenuate faster than e.g., Cu 3p and Se 3d. However, while the sodium signal vanished for 1 nm thickness in the noise, even a (very) small Cu $2p_{3/2}$ signal is detectable at 6 nm and possibly at 9 nm In_xS_y. A floating of sodium on the In_xS_y surface during the layer deposition [125] can be ruled out in the present case. The Cu $2p_{3/2}$ signal implies a weak copper diffusion into the buffer layer up to about 10 nm In_xS_y. This copper diffusion will be discussed later in dependence of S/In ratio in this section.

After the annealing step at 200 °C, the Na 1s and Cu $2p_{3/2}$ intensities reappear in agreement with earlier publications which also found an interdiffusion of Cu starting at such high temperatures [10, 125, 161]. The copper intensity as well as the sodium intensity exhibit about 60 - 80 % of the bare CISSe surface intensity for all investigated interfaces. Furthermore, the sodium signal of the CISSe absorber is very broad implying at least two sodium species, e.g., a Na compound on the CISSe surface (1072.3 eV) and Na_2CO_3 (1071.5 eV) [133]. In contrast, the annealed sample shows only one species. Bär *et al.* proposed the formation of a sodium film and/or Na_xS islands at the surface. In order to find out which sodium

Table 6.1: S/In surface ratios of different In_xS_y films and the corresponding surface content determined from the XPS data. All compositions are sulfur-poor compared to stoichiometric In_2S_3. The annealing step induces a prominent copper diffusion of about 4 % at the surface while in parallel the S/In ratio increases.

In_xS_y	x = 40.2 %	x = 41 %	x = 42 %	x = 43.2 %
as-received				
In (%)	48.2 ± 2.2	46.2 ± 2.7	47.1 ± 2.7	45.9 ± 2.2
S (%)	51.8 ± 2.4	53.8 ± 3.2	52.9 ± 3.0	54.1 ± 2.6
S/In	1.07 ± 0.07	1.16 ± 0.09	1.12 ± 0.09	1.18 ± 0.08
annealed				
In (%)	42.2 ± 1.9	43.0 ± 2.3	42.0 ± 1.9	42.2 ± 2.4
S (%)	53.6 ± 2.5	52.5 ± 2.8	53.7 ± 2.4	53.9 ± 2.6
Cu (%)	4.1 ± 2.0	4.4 ± 1.7	4.3 ± 1.8	4.0 ± 2.0
S/In	1.27 ± 0.08	1.22 ± 0.09	1.28 ± 0.08	1.28 ± 0.09
Cu/In	0.10 ± 0.05	0.10 ± 0.04	0.10 ± 0.04	0.09 ± 0.05

compound is formed, the modified sodium Auger parameter α'_{Na} and a more surface sensitive measurement are discussed. For the 50 nm annealed In_xS_y/CISSe sample α'_{Na} equals (2063.71 ± 0.15) eV. In literature it is speculated that this value corresponds to a Na-S bond without any further bonding partners [141, 142]. The surface sensitive measurement (60 ° emission to the surface normal; topmost spectrum in Fig. 6.3) shows the identical intensity distribution for the Na 1s signal as for the normal emission measurement and thus ruling out the formation of Na_xS islands. In fact, the formation of an homogeneous distribution of a possible Na-S layer at the surface is likely.

A further common characteristic of all investigated core levels is a small shift of the absorber-related peaks (see Figs. 6.2 and 6.3) with increasing buffer thickness. These shifts suggest a relative shift of all bands/core levels with respect to the Fermi level due to the interface formation and will be evaluated in section 6.1.2.

Table 6.1 summarizes the chemical surface composition of the In_xS_y and annealed In_xS_y buffer layer as determined by analyzing the different core level peaks (i.e., In 4d, Cu 3p, and S 2p) according to section 3.1. For the annealed samples, the adjusted copper-free In_2S_3 (see Fig. 6.3 top) spectrum was subtracted from the In_xS_y/CISSe samples to remove the In 4p intensity from the spectrum and allow the determination of the Cu 3p intensity. A striking result of this quantitative analysis is the sulfur-poor surface of the In_xS_y films compared

with stoichiometric In_2S_3 (S: 60 % and In: 40 %) *independent* of the nominal S/In ratio. Moreover, all investigated samples have the same S/In ratio within the error bar. Thus, statements of possible changes of the surface content for the investigated indium contents are at the detection limit of XPS.

In section 4.2 and Refs. [162, 163], it is suggested that an indium sulfide surface is sulfur-poor which is confirmed by these measurements. The fact that the measured In_xS_y films have the same S/In ratio suggests that for all In_xS_y films ($40.2 \leq x \leq 43.2$) a similar or even identical In-S phase is formed at the surface. A possible candidate for this phase is In_6S_7. The S/In ratio of In_6S_7 is $7/6 \simeq 1.17$ and agrees well with the determined the S/In surface ratio. However, a mixture of the three structures In_2S_3, In_6S_7, and InS cannot be excluded. In fact, a direct correlation between an increasing In content in the In_xS_y films and an increasing contribution (integral) of In_6S_7 and InS was found [159]. After the annealing step, the sulfur concentration of all investigated indium sulfide films stays constant within the error. In parallel, a pronounced decrease of indium is observed which leads to a significant higher S/In ratio compared to the as-deposited films. This is accompanied with a distinct enhancement of the copper signal. The computed Cu contents is independent for all In_xS_y films and amounts to (4 ± 2) %, which is approximately the same value as the indium reduction. This Cu content is in good agreement with the reported 5 atomic percent of Pistor *et al.* after a post heat-treatment at 200 °C [125]. The impact on the electronic properties of the presence of Cu in In_xS_y films will be discussed later in this chapter.

In the literature the formation of a $CuIn_5S_8$ [10, 164], or $Na_xCu_{1-x}In_5S_8$ [126] phases are proposed. The sodium content, derived from the Na 1s line, is about (1.0 ± 0.8) % at all annealed In_xS_y surfaces. Thus, the sum of the copper and sodium concentration at the surface of (5.0 ± 2.2) % agrees within the error bar with the model of $\frac{1}{1+5+8} = 7.1$ %. However, the indium composition is significant higher and the sulfur composition somewhat lower than the proposed 1:5:8 composition. One possible explanation of the sulfur-poor annealed In_xS_y films is the sulfur-poor surface of the non-annealed samples. Furthermore, the surface of indium sulfide films tends to be sulfur depleted, which might be an alternative explanation of the data.

In literature it is found that the crystallinity of the films decreases with increasing indium content, i.e., the grain size decreases [6, 159]. The reduction of the crystallinity reduces the ability of copper to diffuse [6]. However, for $40.2 \leq x \leq 43.2$ the copper contents at the surface are similar after annealing which suggests that the crystallinity of the investigated films play a minor role for the copper concentration at the surface.

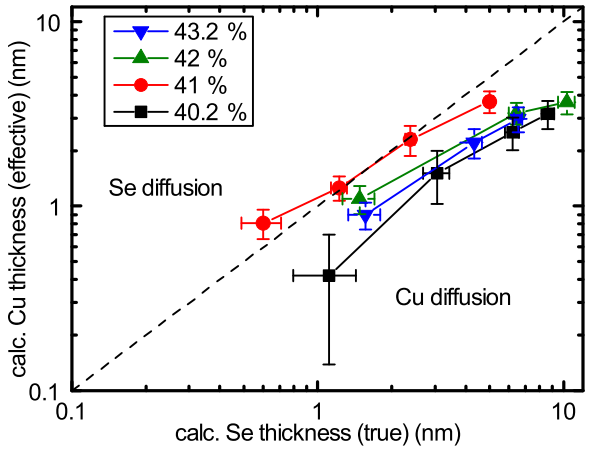

Figure 6.4: "Effective" In_xS_y buffer layer thickness (calculated from the attenuation of the Cu $2p_{3/2}$ signal) versus the "true" thickness (calculated from the attenuation of the Se 3d signal) for different indium contents of the buffer layer.

Copper diffusion for not annealed In_xS_y

In Fig. 6.3, a small Cu $2p_{3/2}$ signal is visible for an In_xS_y thickness of 9 nm which implies a copper diffusion into the indium sulfide buffer layer. In the following, a more detailed picture of the copper-related interdiffusion phenomena of the In_xS_y/CISSe interface in dependence of the nominal indium content upon deposition is given. For a quantification a "true" buffer thickness was calculated using the attenuation of the Se 3d signal. Figs. 6.2 and 6.3, as well as several publications [10, 70, 158] suggest that selenium is not diffusing into the In_xS_y buffer during the deposition and hence the assumption of using Se 3d to determine a "true" buffer thickness seems a good choice. In Fig. 6.4, the "effective" thickness is plotted (which was computed using the attenuation of Cu $2p_{3/2}$ signal) for indium contents of $40.2 \leq x \leq 43.2$. If copper diffuses into the buffer layer the "effective" thickness is smaller than the "true" thickness and hence the data points will be located below the diagonal dashed line, which separates the "Se diffusion" from the "Cu diffusion". As expected, the data highlight a copper diffusion up to about 5 - 10 nm buffer thickness. Indium contents close to the maximum conversion efficiency η (see Fig. 6.1) show the smallest diffusion (for $x = 41$ % only the 5 nm point suggests a weak Cu diffusion).

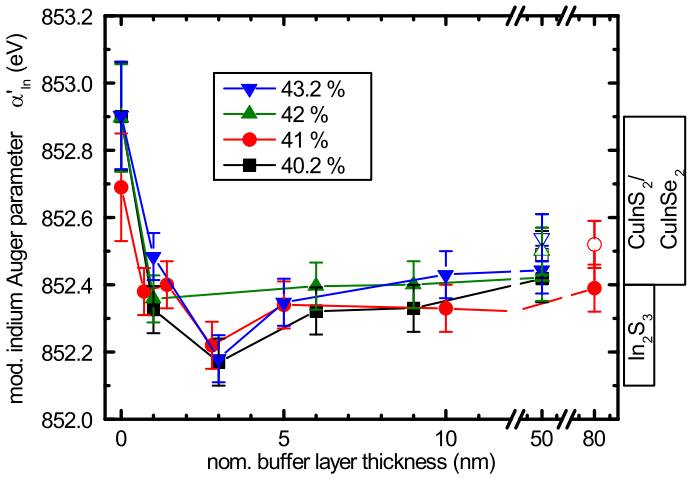

Figure 6.5: Modified indium Auger parameter α'_{In} for the investigated indium contents for different indium sulfide buffer layer thicknesses. The open data points identify the respective annealed samples. Bars on the right-hand side mark the range commonly found for possible compounds [62, 150, 165–167].

Chemical environment of indium

To further investigate the chemical structure of the In_xS_y buffer layer, the modified indium Auger parameter α'_{In} was calculated using the In $M_4N_{45}N_{45}$ and In $3d_{5/2}$ signals for all investigated In_xS_y compositions and is displayed in Fig. 6.5. The error bar of α'_{In} stems mainly from the uncertainty of the determination of the position of the $M_4N_{4,5}N_{4,5}$ Auger transition. For the 0 nm data points (= pristine CISSe) the latter exhibit a second component which can be related to an oxidized indium. The determination of the CISSe component was conducted using a spectral decomposition according to Fig. 5.5. For $CuInS_2$ and $CuInSe_2$, a modified Auger parameter of $\alpha'_{CIS,CISe} = (852.9 - 852.4)\,\text{eV}$ [165–167] and for In_2S_3 $\alpha'_{In_2S_3} = (852.4 - 852.1)\,\text{eV}$ [62, 150] can be found in the literature. The Auger parameter for all investigated absorbers has a mean value of $(852.85 \pm 0.09)\,\text{eV}$. The difference between the absorbers can possibly be explained with a slightly different In/Cu ratio [168] but also lies within the error bar.

For increasing buffer thickness, α'_{In} decreases by $(0.46 \pm 0.10)\,\text{eV}$ (1 nm In_xS_y) and by 0.66 eV to $(852.19 \pm 0.02)\,\text{eV}$ for the 3 nm thick buffer layer. The decreasing α'_{In} can be assigned to a change of the chemical environment of the In atoms from a CIS(Se)-like to an In_2S_3-like environment. This suggests that the formation of the buffer layer already takes place upon deposition of the first layers of the buffer. For increasing In_xS_y thickness, α'_{In} stabilizes at about 852.4 eV and for the maximum buffer layer thickness α'_{In} yields a value of

(852.42 ± 0.02) eV. Please note that for x = 40.2 %, 42 %, and 43.2 % the maximum buffer thickness is 50 nm while for x = 41 % it is 80 nm, respectively. The determined value of α'_{In} for the thickest buffer layer is almost identical with the value of 852.4 eV of an atomic layer deposited (ALD) In_2S_3 buffer layer [150]. After the annealing step (open data points for each indium content) the modified Auger parameter increases for all samples to (in average) $\alpha'_{In} = (852.52 \pm 0.02)$ eV. This clear increase suggests a changing chemical environment from an In_2S_3-like environment to a Cu-In-S environment upon annealing.

In order to enhance the bulk sensitivity, XES measurements will be discussed below to illuminate the chemical properties of the bulk of the In_xS_y/CISSe samples in the following.

Chemical environment of sulfur

The In_xS_y/CISSe samples were irradiated with $h\nu = 200$ eV photons in order to excite the S $L_{2,3}$ edge non-resonantly. A selected XES S $L_{2,3}$ spectrum of a bare CISSe absorber is shown in Fig. 6.6 a). All spectra which are shown in the following are normalized to the S 3s → S 2s transition at about 147 eV. In Fig. 6.6 b) only the region of the upper valence band (153 eV - 163 eV) of the In_xS_y/CISSe (x = 42 %) interface is shown. For this XES analysis the 80 nm In_xS_y buffer series is investigated in order to clearly separate the buffer signal from the CISSe absorber signal, as 90 % of the signal stems from the upper 76 nm (calculated for excitation with 200 eV photons at an incident angle of 45 ° and emitted photons of ≈155 eV at an exit angle of 45 ° using [169, 170]). For x = 41 %, a 80 nm thick In_xS_y buffer layer was investigated, while for x = 40.2 % and x = 43.2 % the maximum buffer layer thickness was about 50 nm.

The pristine CISSe spectrum (bottom) exhibits four features. The first three features (1) at ≈ 155 eV, ≈ 156.3 eV, and ≈ 157.7 eV stem from electrons decaying from the In 5s-derived valence states into the S 2p hole [136]. Transitions of the valence band of Cu 3d-derived states into the S 2p hole can be seen in the region of ≈ 159 eV - 161 eV [171]. The main intensity is marked with a vertical line (2) and serves as an indicator of Cu-S bonds. With increasing buffer thickness, the CISSe-related features decrease especially the Cu 3d-derived states. For 80 nm In_xS_y buffer layer thickness, the spectrum strongly resembles the spectrum of the co-evaporated In_2S_3 reference. The small differences between these spectra can possibly be explained with small deviations in the chemical environment (as discussed for the buffer layer surface above). Furthermore, the indium sulfide spectra exhibit only the three In 5s → S 2p peaks but not the Cu 3d → S 2p intensity. After the annealing step, the feature (2) reappears, which suggests a formation of Cu-S bonds due to the diffusion of copper.

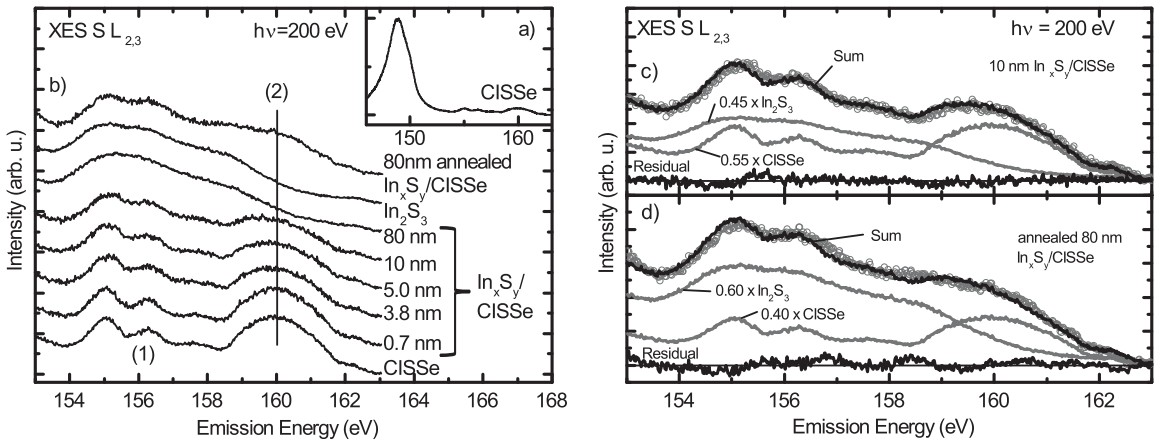

Figure 6.6: S $L_{2,3}$ ($h\nu = 200$ eV) spectra of a) a CISSe absorber (including the S 3s $\rightarrow$ S 2s transition) b) different as-deposited In_xS_y/CISSe interface structures with x = 42 % and the annealed 80 nm In_xS_y/CISSe sample showing the upper valence band. c) and d) show the spectra of the 10 nm and annealed In_xS_y/CISSe samples and a two-component fit using the spectrum of the CISSE absorber and the In_2S_3 reference. Spectra c) and d) were reprinted with permission from Hauschild *et al.*, J. Phys. Chem. C **119**, 10412 – 10416 (2015). Copyright (2015) American Chemical Society.

To quantify the S $L_{2,3}$ XES data, all spectra were fitted with a sum of the spectra of the pristine CISSe and the In_2S_3. This is exemplarily performed for the 10 nm In_xS_y/CISSe and the annealed 80 nm In_xS_y/CISSe samples in Fig 6.6 c) and d), respectively. The as-deposited 10 nm In_xS_y/CISSe sample can be reproduced by (0.55 $\times$ CISSe + 0.45 $\times$ In_2S_3) and with the determined factors the Cu/In ratio can be estimated (assuming that no other phases are present and that the overall cross section in the spectra is identical):

$$\frac{\mathrm{Cu}}{\mathrm{In}} = \frac{I\left[\mathrm{S\ L_{2,3}(CISSe)}\right]}{I\left[\mathrm{S\ L_{2,3}(CISSe)}\right] + 2 \cdot I\left[\mathrm{S\ L_{2,3}(In_2S_3)}\right]} \,. \tag{6.1}$$

Here, $I\left[\mathrm{S\ L_{2,3}(CISSe)}\right]$ and $I\left[\mathrm{S\ L_{2,3}(In_2S_3)}\right]$ denote the intensity of the CISSe and the In_2S_3 components, respectively. This ratio only takes the copper and indium atoms into account which are chemically bound to sulfur. For the 80 nm sample, the Cu/In ratio determined this way is (0.03 ± 0.01). This small Cu amount stems probably from the CISSe substrate suggesting no diffusion of Cu after the buffer layer deposition. For the annealed 80 nm In_xS_y/CISSe sample a Cu/In ratio of (0.25 ± 0.03) is computed. This value is significantly larger than the XPS-derived ratios of Cu/In ≈ 0.1 (see Tab. 6.1) and even larger than the proposed Cu/In = 0.2 of the $CuIn_5S_8$ phase. This finding can possibly be explained with a concentration profile from the substrate towards the In_xS_y surface, where the XES technique

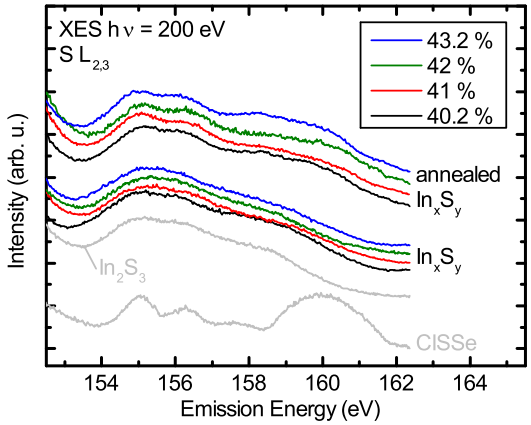

Figure 6.7: S $L_{2,3}$ emission spectra of different non-annealed and annealed In_xS_y buffer layers. The two bottommost spectra show the CISSe and In_2S_3 reference spectra. The x = 40.2 % and 43.2 % In_xS_y buffer layers are 50 nm thick whereas the x = 41 % and 42 % are 80 nm thick.

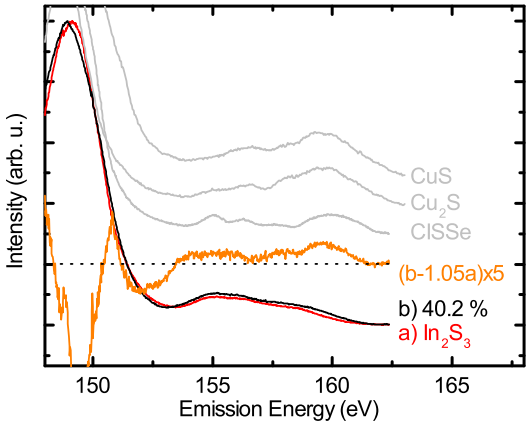

Figure 6.8: S $L_{2,3}$ emission spectra of the as-deposited 40.2 % sample a) and from co-evaporated In_2S_3 b). Deviation (orange) of (b$-1.05 \times$ a) scaled with a factor of five. The CISSe, Cu_2S, and CuS spectra are plotted as reference. The Cu_2S and CuS spectra are courtesy of L. Weinhardt.

integrates over the complete buffer thickness. Accordingly, the CISSe near-surface region acts as copper source and will be copper-depleted in the interface region.

Fig. 6.7 shows the XES S $L_{2,3}$ spectra of the valence region of the investigated In_xS_y and annealed In_xS_y samples. The bottommost CISSe and co-evaporated In_2S_3 spectra are used as reference. All non-annealed In_xS_y ($40.2 \leq x \leq 43.2$) spectra replicate the In_2S_3 well. A small exception is found for the x = 40.2 % sample. The intensity in the energy region between 158 - 159 eV is slightly higher in comparison with the other In_xS_y spectra. A closer investigation points out that the x = 40.2 % In_xS_y spectrum cannot be reproduced by a superposition of the CISSe and In_2S_3 contributions. For this purpose, the In_2S_3 reference spectrum was subtracted from the x = 40.2 % In_xS_y spectrum (scaled with a factor of 1.05) as shown in Fig. 6.8 c). The resulting spectrum is in the energy range 150 eV - 152 eV slightly higher pointing towards a shift of the S 3s $\rightarrow$ S 2p transition. Furthermore, the energy range commonly found for Cu-S bonds (159 - 161 eV) exhibits additional intensity. This suggests that during the deposition, In-S bonds were broken and new Cu-S bonds formed with the diffusing copper. This finding is in agreement with the reported higher crystallinity for In_xS_y films with $x \leq 40.5$ % and hence an enhanced copper diffusion is suggested [6]. Furthermore, additional intensity in the energy range of about $154 - 158$ eV is detected, which is not described by the In_2S_3 spectrum. For this purpose, a CISSe, a

Cu_2S, and a CuS reference spectrum are additionally plotted in Fig 6.8. All spectra exhibit intensity in the region $157-160$ eV and hence a Cu-S bond is possibly formed upon deposition of the x = 40.2 % In_xS_y buffer. Another explanation of the feature at about 158 eV is possibly a different chemical environment of the In_xS_y ($x \leq 40.5$ %) in comparison with the co-evaporated In_2S_3.

After the annealing step, a distinct copper diffusion can be seen in Fig. 6.7 (four upper spectra) for all samples. The spectra exhibit additional spectral weight at 160 eV which indicates Cu-S bonds. By superimposing the annealed sample spectra with the CISSe and In_2S_3 spectrum, it emerges that only the x = 42 % sample (see Fig. 6.6 d)) can be completely reproduced. For the x = 40.2 %, 41 %, and 43.2 % samples additional intensity is at about 158 eV which can possibly be explained by the formation of a Cu_xS- or CISSe-like phase as it was shown for the as-grown x = 40.2 % sample in Fig. 6.8.

In summary, the XPS data show similar chemical properties for the different In_xS_y/CISSe interfaces, like a sulfur-poor/indium-rich surface composition and a significant copper amount of about (4 ± 2) % which appears at the In_xS_y surface upon annealing. The XES data reveal for x = 40.2 % the formation of an additional Cu-S phase upon deposition, while for x > 40.2 % no extra Cu-S phase was found. After the annealing step a similar amount of copper was determined in the XES spectra for all samples. Hence, no reliable differences of the several sample sets were found which could explain the efficiency of the solar cell in dependence on the indium content. To get more insight into that topic, the electronic properties of the In_xS_y/CISSe interface are outlined in the following.

6.1.2 Electronic properties in dependence on the nominal S/In ratio

In order to reveal the conduction band and valence band alignment a combination of UPS and IPES was used. The valence band maxima (VBM) and conduction band minima (CBM) were determined with a linear extrapolation of the leading edges (see section 3.2). The as-received samples are contaminated with oxygen and carbon adsorbates due to the transport and storage in not humidity-free and oxygen-free environments. This leads to a superposition of the band edges of the adsorbates with the true band edges of the samples. The contaminants have thus to be removed which was carried out via a soft 50 eV Ar^+ ion treatment. Several cleaning steps need to be performed until the true band edges appear and the band edge positions do not change upon further cleaning. Between each sputter step the progress of the reduction of the O 1s and C 1s signals were carefully monitored by XPS. In

addition, the possible formation of metallic phases can be excluded with the help of XPS and XAES.

The cleaning steps for a typical CISSe absorber are illustrated in Fig. 6.9. The UPS/IPES spectra are normalized to the respective maximal intensity within the shown window. The bottom spectrum displays the as-received (non-sputtered) CISSe absorber and the spectra above the progress of the 50 eV Ar^+ cleaning procedure after 20 min, 40 min, and 60 min, respectively. The spectrum of the unsputtered sample is dominated by the adsorbate signal and hence displays a very large band gap of (1.84 ± 0.18) eV. With increasing sputter steps a feature at about 3 eV emerges which is indicative for Cu 3d-derived bands. Furthermore, the VBM position increases and the CBM position decreases with respect to the Fermi energy E_F (binding energy = 0 eV). After 60 min of sputtering, a CISSe VBM of (0.86 ± 0.05) eV and a CBM of (-0.59 ± 0.10) eV is observed. This results in a CISSe surface band gap of (1.45 ± 0.11) eV. A comparison with other published results of the surface band gap of chalcopyrite absorbers [8, 9] shows a good agreement. However, the surface band gaps are much larger than bulk band gaps (i.e., ≈ 1.1 eV [172–174]) underlining the necessity of the direct approach using UPS and IPES as opposed to use only XPS/UPS and bulk band gaps for the determination of the conduction and valence bands alignments. It is conspicuous that the distance of the CBM towards E_F is smaller than the VBM which demonstrates the type inversion (n-type at the surface while the bulk is p-type) of the absorber.

In order to understand the efficiency dependence of the *nominal* In content, the buffer layers with varying In content were stepwise cleaned and monitored for possible sputter damage. The cleaned In_xS_y spectra are plotted in Fig. 6.10. The two bottom spectra display the cleaned CISSe spectrum after 40 min (gray) and after 60 min (black) for comparison. The positions of the CBM and VBM are illustrated with the red extrapolated leading edges. All In_xS_y spectra exhibit a small foot in the valence regime at about 1.8 eV, which is larger than the experimental UPS resolution of about 100 meV. This might originate from defect states at the valance band edge or real In_xS_y states. Only a few reliable In_2S_3-related XPS/UPS spectra exist in the literature which also show this broadening [150, 158]. This suggest that the states probably belong to the density of states of the valence band. Correspondingly, the real VBM is expected to be somewhat closer to E_F than determined by the leading edge extrapolation. This is included in a larger error bar for the VBO and does not affect the determination of the CBO (the latter is the relevant property for the solar cells).

All In_xS_y buffer layers are n-conducting and have similar band gap values. However, the CBM moves closer to E_F with increasing indium (decreasing sulfur) content while the VBM shows no general trend. This is in agreement with the earlier mentioned increase of the n-conductivity due to a lack of sulfur [155]. In addition, the shape of the x = 40.2 % IPES

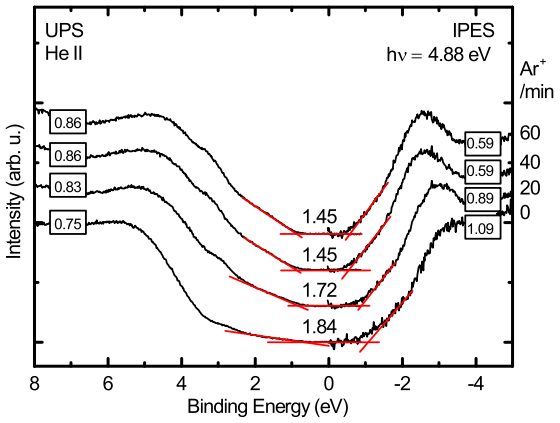

Figure 6.9: UPS/IPES measurements of the valence and conduction band of the CISSe absorber as-received and for increasing Ar^+ sputter times ($E = 50\,\text{eV}$, $j = 80 - 100\text{nA/cm}^2$). The determined VBM, CBM, and surface band gaps are depicted in eV.

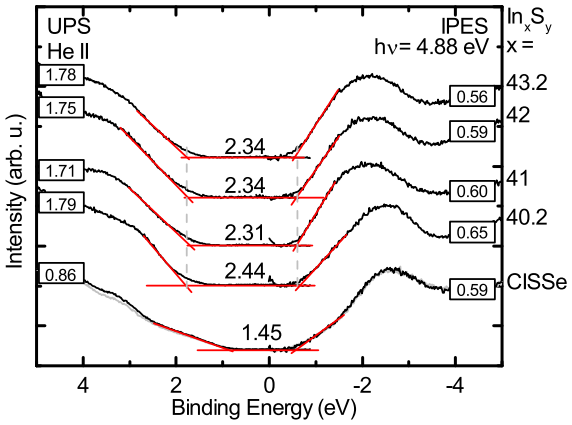

Figure 6.10: UPS/IPES measurements of the valence and conduction band of the cleaned In_xS_y/CISSe interfaces for different indium contents x. The bottom spectra show the 40 min and 60 min Ar^+-treated CISSe absorber in gray and black, respectively. The determined VBM, CBM, and surface band gaps are depicted in eV. As a guide to the eye, vertical gray dashed lines indicate the mean VBM and CBM of the In_xS_y buffers.

spectrum is different in comparison with the others which can tentatively be explained with the different indium sulfide phase (β-In_2S_3) for x $\leq$ 40.5 %. Kim and Kim [175] found an increasing band gap for increasing sulfur content, e.g., for $In_2S_{2.5}$ 2.15 eV and $In_2S_{3.5}$ 2.34 eV. Barreau *et al.* explained this by the identification of the valence band maximum to be mainly composed by S p orbitals while the lowest unoccupied states are formed by S p and In p states [155]. The latter findings might explain the reduction of the band gap from $E_{Gap}^{Surf} = (2.44 \pm 0.14)\,\text{eV}$ for sulfur-rich composition (x = 40.2 %) to $E_{Gap}^{Surf} = (2.34 \pm 0.14)\,\text{eV}$ for sulfur-poor composition (x = 43.2 %).

In order to determine the band alignments, the interface induced band bending (IBB) has to be considered in addition to the VBM and CBM positions (see section 3.2). For that purpose, thin buffer layer thicknesses in which the XPS substrate signals are still detectable can be analyzed. With an In_xS_y buffer this is challenging, since both, absorber and buffer contain indium and sulfur. Accordingly, the IMFP λ of the respective core levels are used as the criterion where the upper cover layer and substrate can be distinguished from each other.

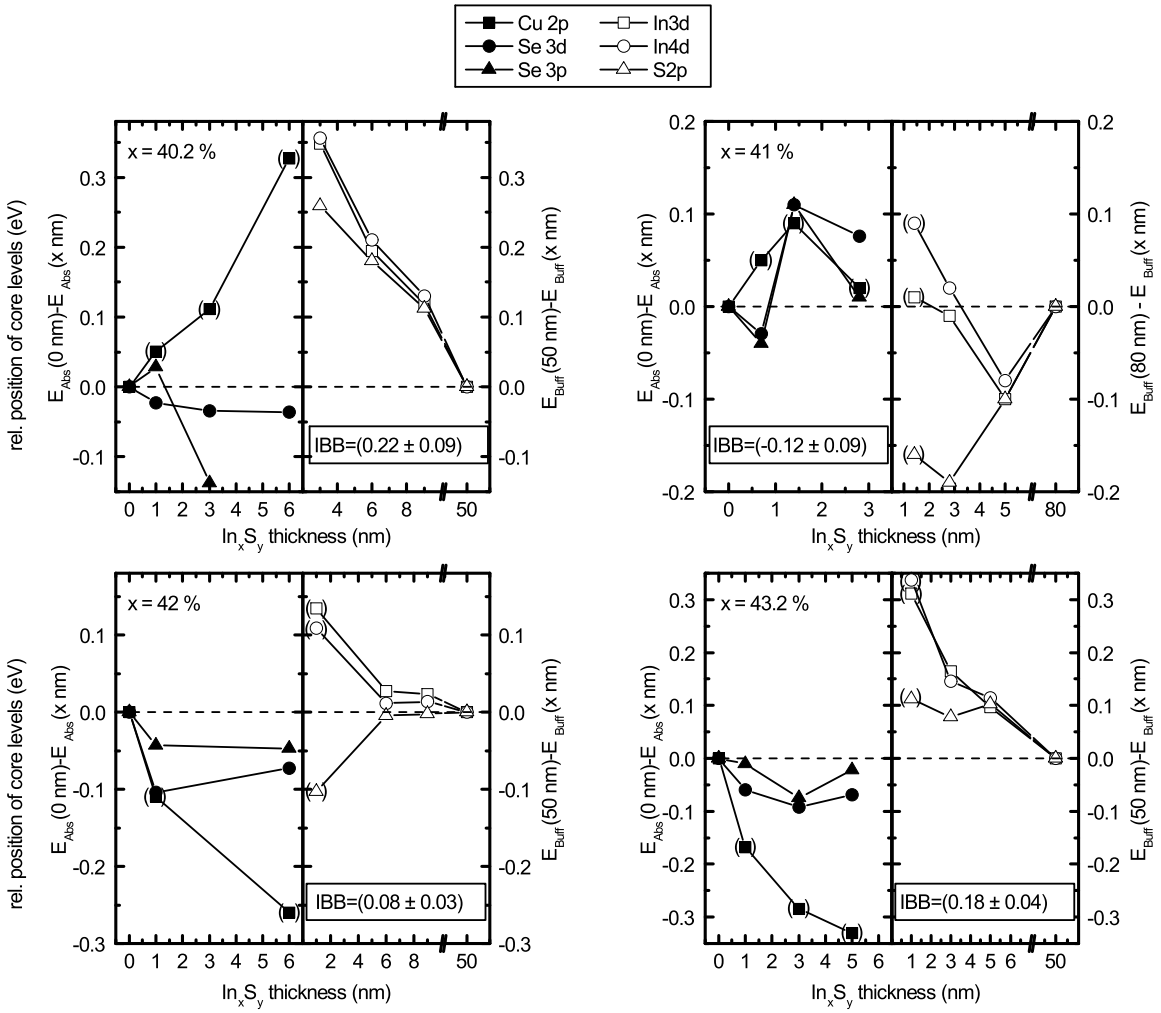

Figure 6.11: Relative shifts of the respective core levels needed to determine the IBB for increasing indium content of the buffer layer. Copper-related values are excluded due to possible chemical shifts. Buffer layers which are thinner than λ are also excluded for the determination of the IBB.

At this thickness, 63 % of the signal stems from the upper layer. The according values are 1.8 nm, 2.3 nm, and 2.5 nm for In 3d, S 2p, and In 4d, respectively [160]. Thus, buffer layer thicknesses smaller than λ are not considered for the determination of the IBB. In Fig. 6.11, the relative shifts of the absorber and buffer layer core levels are plotted for different nominal indium contents of the buffer layer. The substrate-related core levels shifts (selenium and copper) are displayed on the left-hand side, whereas the indium sulfide buffer-related shifts (indium and sulfur) are shown on the right-hand side. For the sake of completeness, the copper-related shifts are also plotted (copper-related values are put in brackets). However,

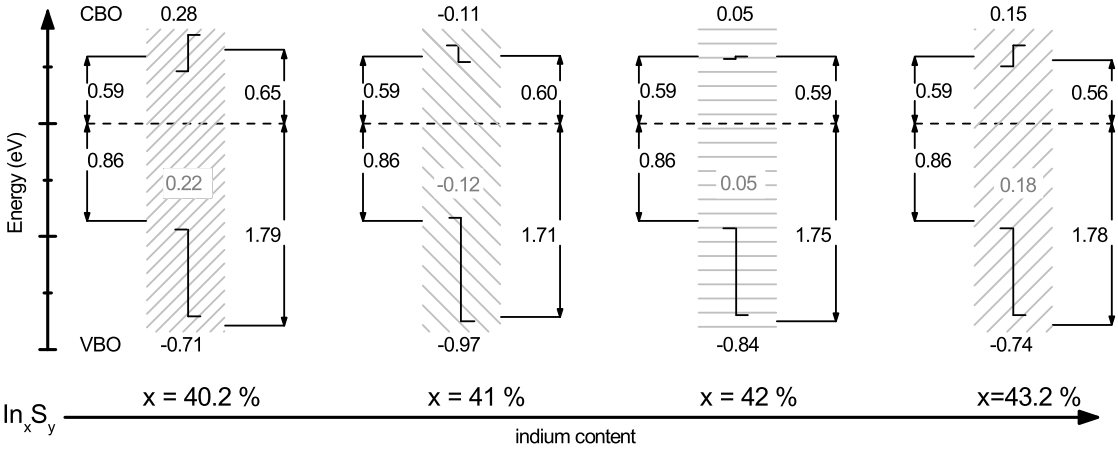

Figure 6.12: Schematic band diagrams of the abrupt In_xS_y/CISSe interface for increasing indium contents. The CBO and VBO are conveniently illustrated as step. The gray shaded boxes sketch the IBB.

these values are neglected for the calculation of the IBB because copper diffuses into the buffer upon deposition, causing potentially a chemical shift of the corresponding lines that can probably not be neglected.

The values for the IBB are computed as the mean value of each pair of values (the error bars arise from the respective standard deviation). In this way, the following IBB values are determined for In_xS_y/CISSe interfaces: (0.22 ± 0.09) eV, (-0.12 ± 0.09) eV, (0.08 ± 0.03) eV, and (0.18 ± 0.04) eV for x = 40.2 %, 41 %, 42 %, and 43.2 %, respectively. In addition, for x = 42 % the 80 nm sample series gives an IBB of (0.02 ± 0.06) eV (not shown). For x = 40.2 %, the IBB has a positive value. The increasing indium content and the corresponding $\beta \rightarrow \alpha$-phase transition of In_xS_y has a prominent impact on the IBB. In fact, for x = 41 % a negative IBB value is found and for further increasing indium content the IBB increases continuously. The final values of the CBO and VBO are calculated using equation 3.3 and 3.4. The schematic band structure is sketched in Fig. 6.12 in dependence of the nominal indium content. For convenience, the CBOs and VBOs are plotted as abrupt steps. Furthermore, gray lines illustrate the IBB.

The band diagrams of the not annealed In_xS_y/CISSe interface show a clear dependence on the nominal indium content. For x = 40.2 % a significant spike of about (0.28 ± 0.16) eV is monitored. For x = 41 % the CBO changes abruptly to a small cliff of (-0.11 ± 0.14) eV. For further increasing indium content of the buffer layer the CBO increases and correspondingly an almost flat alignment of (0.05 ± 0.13) eV and a small spike of (0.15 ± 0.12) eV can

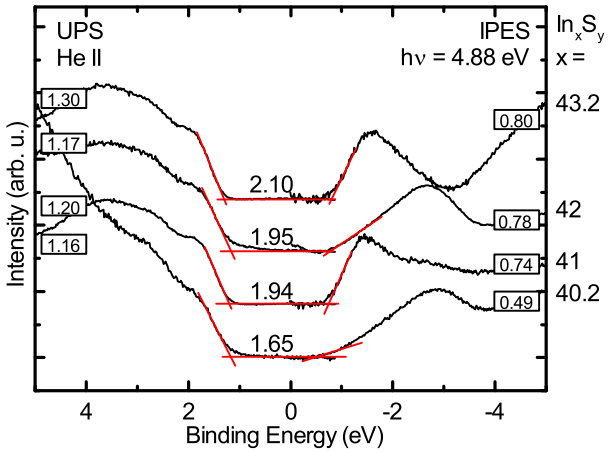

Figure 6.13: UPS/IPES measurements of the valence and conduction band of the annealed In_xS_y/CISSe interfaces for different indium contents x. The determined VBM, CBM, and surface band gaps are given in eV.

be found for x = 42 % and x = 43 %, respectively. A cliff-like conduction band alignment is expected to lead to a decrease in the open circuit voltage V_{OC} [53, 108], whereas a spike-like CB alignment reduces the short circuit current I_{SC} and thus the efficiency [41]. Correspondingly, the sketch gives a first hint to explain the S/In-ratio dependence of the efficiency. However, the described interfaces do not include the heat treatment as it occurs in the subsequent solar-cell process and the corresponding interdiffusion of copper. Hence, another set of UPS/IPES measurement was done *in-situ* after the annealing step and the result is shown in Fig. 6.13.

At first glance, significant spectral changes for different indium contents can be observed. The IPES spectra exhibit for x = 40.2 % and 42 % as well as for x = 41 % and 43.2 % the same spectral shape. The UPS spectra for x $\geq$ 41 % look similar while the spectrum of the 40.2 % sample differs significantly. In comparison with the non-annealed data, all spectra exhibit additional intensity at about $E_{Bind} = 3$ eV which can be related to copper 3d-derived states. Since copper primarily affects the valence band [123] this copper diffusion shift the VBM for all indium sulfide contents by approximately 0.5 eV towards the Fermi level. Furthermore, a small shift of the CBM is also observed by about 0.15 eV for x $\geq$ 41 %.

For increasing amount of copper within β-In_2S_3, a reduction of the optical band gap and a reduced n-conductivity is reported [121, 176]. However, only the x = 40.2 % sample (β-phase) fits with $E_{Gap}^{Surf} = (1.65 \pm 0.14)$ eV to the reported band gaps of the expected n-type $CuIn_5S_8$ band gap of 1.5 eV (single crystal) [177] or 1.6 eV (thin-film) [121]. For larger indium contents x $\geq$ 41 % the surface band gaps of the annealed samples are significant

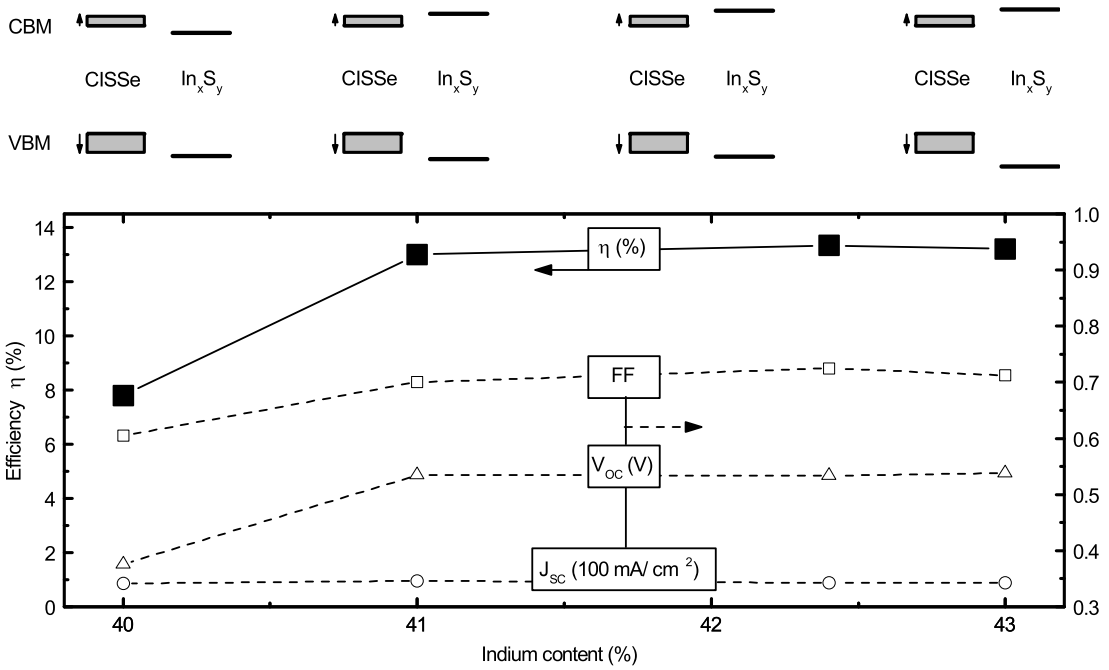

Figure 6.14: Top: schematic band diagrams of the annealed In_xS_y/CISSe interface as a function of the indium content x. The solid lines of the CISSe absorber illustrate the VBM and CBM in the non-annealed case. The gray areas indicate with arrows the band gap increase due to annealing. Bottom: Solar cell parameters (η, FF, V_{OC}, and J_{SC}) for different indium contents. The error bars are in the range of the data points. (Data taken from Ref. [159].)

larger. This can possibly be related to the different indium sulfide α-phase present before annealing. The interdiffusion of copper towards the In_xS_y/CISSe surface is expected to alter the hidden In_xS_y/CISSe interface significantly (= not accessible with PES in the laboratory due to the small IMFP). In fact, with destructive as well as non-destructive methods, indications for Cu-depleted absorber surfaces were found [10, 178, 179]. This copper-depletion of the former CISSe surface is expected to shift the VBM to higher binding energies which is accompanied by a reduced interface recombination [53]. Also a diffusion of Se due to annealing seems likely [70, 119] which is expected to shift the CBM away from E_F [47]. In Fig. 6.14, a model for the annealed In_xSy/CISSe interface band alignment in dependence of the indium content which takes these considerations into account is proposed. In this model, the determined position of the CBM and VBM are sketched as black lines for the CISSe and In_xS_y for each indium content. The expected increase of the band gap of the

absorber surface is schematically shown as a gray box, where arrows indicate the increase. For x = 40.2 %, a significant cliff appears in the conduction band alignment. With increasing indium content, the offset turns from a cliff-like to a slight spike-like alignment (i.e., 0.05 eV - 0.10 eV), which gets more and more pronounces with increasing In content. To support the proposed model, the solar cell parameters (efficiency, fill factor, V_{OC}, and J_{SC}) of the full device (absorber with In_xS_y followed by the transparent ZnO front contact) are also depicted at the bottom of Fig. 6.14. With increasing indium content, the efficiency first increases with a maximum at about x = 42 %, before it slightly decrease at higher In contents. This is caused by an increasing fill factor (FF) and open circuit voltage (V_{OC}). The short circuit current J_{SC} remains constant for all investigated indium sulfides. For the cliff-like alignment (x = 40.2 %) an increased interface recombination is expected, in accordance with the loss in V_{OC} [55, 180]. For x $\geq$ 41 %, V_{OC} is significantly higher and rather constant for higher In content, which can be understood taking the almost flat alignment respectively small spike into account and the copper-depleted absorber surface that reduces the recombination probability at the interface [53, 55]. Hence, a striking agreement of the proposed model and the solar cell parameters is detected.

Summarizing the measured UPS/IPES data, a clear picture of the In_xS_y/CISSe interface in dependence of the nominal S/In can be given. The absorber reveals a surface band gap of $E_{Gap}^{Surf} = (1.45 \pm 0.11)$ eV which is in accordance with earlier publications [8, 9]. The In_xS_y buffer layers have a similar band gap independent of the S/In ratio. However, including the interface induced band bending, the indium content x = 40.2 % shows a significant spike. For x = 41 % the conduction band offset is negative and with further increasing indium content it turns into a small spike-like conduction band offset. After the annealing step, the In_xS_y surface band gaps are significantly reduced due to the copper diffusion. Taking changes of the former absorber surface due to diffusion processes into account, a model is proposed which explains the S/In-ratio dependency of the solar cell efficiency. In fact, for x = 40.2 % a clear cliff can be connected to low efficiencies. For increasing indium contents the conduction band offset is flat or reveals a small spike which is in accordance with a high solar cell performance.

6.2 The Na:In_xS_y/CISSe interface

As apparent from Fig. 6.1, indium sulfide buffered solar cells still lack efficiency in comparison with CdS buffered solar cells. One reason for that might be the Cu diffusion which modifies the chemical and electronic properties of indium sulfide films as discussed in section 6.1. The Cu diffusion might lead to lower efficiencies due to a reduction of the buffer band gap after a thermal treatment. However, it was shown that the incorporation of sodium into the In_xS_y buffer layer increases the band gap significantly. Band gaps of up to 2.95 eV could be achieved for sodium contents of $> 6\,\%$ [181]. In literature it is also stated that sodium in the indium sulfide layer hinders the copper diffusion [121, 126]. Consequently, doping indium sulfide with sodium (Na:In_xS_y) is a promising route to reduce the copper diffusion and therefore to widen the band gap of the buffer layer. In fact, efficiencies of up to 17.1 % have been reported [111] thus overtaking CdS-buffered solar cells using the same absorber material which motivated the following study on the Na:In_xS_y/CISSe interface. The samples were processed as described in section 4.2 and transported from Munich to Würzburg in a sealed nitrogen environment until they were loaded into the vacuum chamber via a N_2-filled glovebag.

6.2.1 Chemical properties

The following analysis sheds light on the diffusion of absorber elements into the buffer layer prior and after the annealing step. In Fig. 6.15 XPS spectra of the Na:In_xS_y/CISSe sample series are plotted for energies $E_{Bind} \leq 90$ eV and several increasing buffer layer thicknesses. The copper- and selenium-related signals decrease while the In 4d peak increases with increasing buffer layer thickness, which is similar to the undoped indium sulfide interface which was discussed in section 6.1.1. The fact that the SeO_x intensity attenuates similar to the Se 3d intensity suggests that the buffer layer deposition does not alter the top layers of the absorber. For the pristine absorber, the Na 2s and Na 2p signals are below the XPS detection limit (even the Na 1s shows nearly no intensity). These features appear and gain in intensity with increasing buffer thickness and reach the maximum for the sample with the thickest buffer layer sample (d = 48 nm). An analysis of the Cu 2p (not shown) intensity suggests also a diffusion of copper up to a buffer layer thickness of ≈ 10 nm since the copper signal has not completely vanished at 9 nm. For the Cu 3p signal a statement is difficult since it overlaps energetically with the In 4p. In addition, the Cu 3p has a cross section which is one order of magnitude smaller than that of Cu 2p [38]. In contrast to the copper signal, the Se 3d attenuation excludes the diffusion of selenium upon deposition,

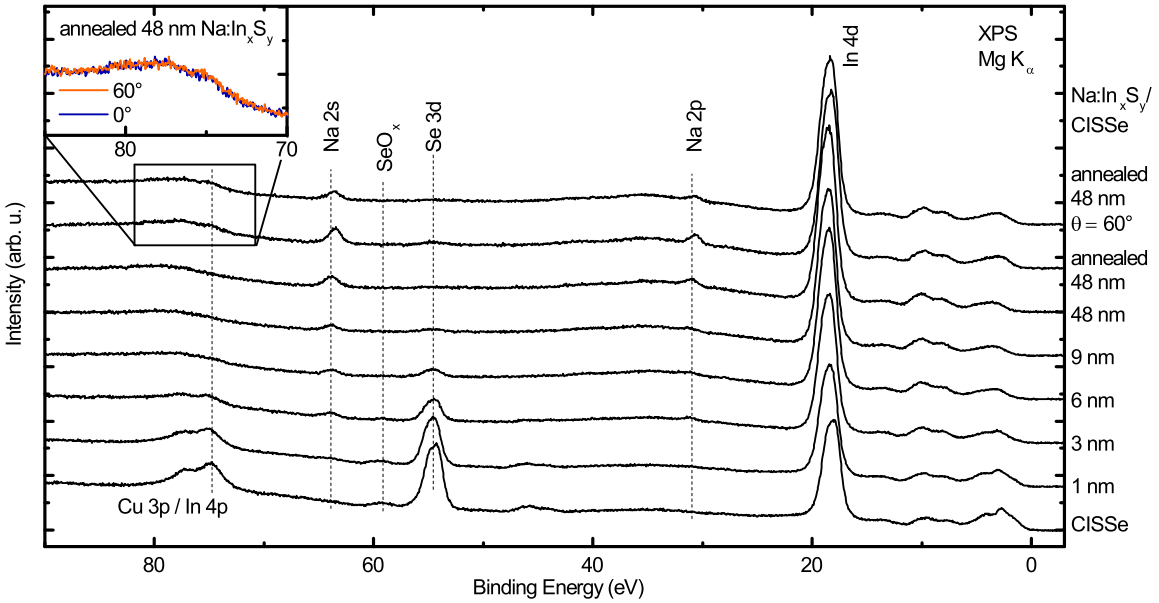

Figure 6.15: XPS survey spectra (Mg Kα excitation) of a CISSe absorber and of the Na:In$_x$S$_y$/CISSe interface for several buffer layer thickness. The thickness increases from the bottom to the top spectrum. The two topmost spectra show the 200 °C annealed 48 nm thick Na:In$_x$S$_y$/CISSe sample at normal and grazing emission ($\theta = 60\,°$). The Cu 3p region of these spectra is magnified in the top left inset. Photoelectron signals are labeled and marked with vertical dashed lines which are relevant for the data analysis.

ruling out the formation of islands. The latter results indicate that doping indium sulfide with sodium has no additional effect on the diffusion properties of the absorber elements. However, the annealing step points towards significant differences of the diffusion behavior of copper, sodium, and selenium (two topmost spectra in Fig. 6.15). A striking result is that almost no copper intensity is observed after annealing, while the sodium intensity increases slightly with respect to the unannealed buffer layer. In addition, a small but distinct Se 3d intensity appears after annealing. With a quantitative analysis an upper limit of the selenium content of about (0.6 ± 0.4) % can be estimated. A similar selenium amount at the surface of pure indium sulfide was found by Pistor [119]. A more surface sensitive measurement (performed at 60 ° to the surface normal) shows a small decrease in intensity for the In, S, and Cu core levels which can be related to the attenuation by residual carbon and oxygen at the surface. The inset in Fig. 6.15 exhibits the Cu 3p/In 4p region of the annealed 48 nm Na:In$_x$S$_y$ spectrum at 0 ° and 60 °. The spectra were normalized to the In 4d showing a constant Cu/In surface ratio. Furthermore, the S/In ratio remains constant which implies a homogeneous copper, indium, and sulfur distribution at the surface of the annealed Na:In$_x$S$_y$

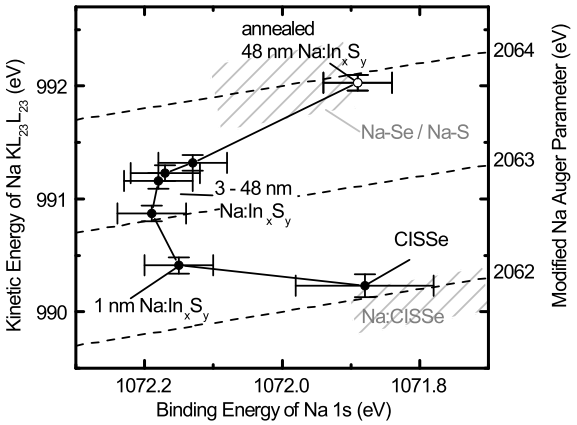

Figure 6.16: Wagner plot for sodium. Diagonal dashed lines indicate values of the modified Auger parameter. With increasing buffer thickness a significant increase of the modified Auger parameter α'_{Na} can be found (black data points). An additional increase after the heat treatment is illustrated by the open data point. Common literature values for sodium compounds are positioned as gray shaded areas [7, 141, 142, 150].

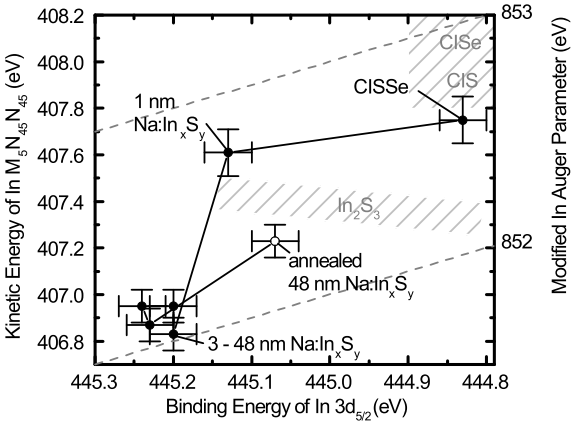

Figure 6.17: Wagner plot for indium. Diagonal dashed lines indicate values of the modified Auger parameter. With increasing buffer layer thickness α'_{In} first increases and afterwards decreases and remains constant for 3 - 48 nm Na:In_xS_y thickness. An additional increase after the heat treatment is illustrated by the open data point. Common literature values for indium compounds are positioned as gray shaded areas [62, 150, 165–167].

buffer. In addition, the sodium and selenium intensities are reduced by a factor of two, implying that these elements are buried below the upper indium-sulfur layer which comprises a small amount of copper, too. In fact, a copper accumulation at the surface was found for In_2S_3 buffers [178, 179] and was also verified for the here used samples with a ToF-SIMS (time-of-flight secondary ion mass spectrometry) measurement by S. Pohlner [159].

Since sodium acts as dopant in the buffer layer, it is desirable to investigate its chemical state. For this purpose, the modified Auger parameter of sodium is investigated and composed in a Wagner plot in Fig. 6.16 as a function of the Na:In_xS_y buffer thickness. The value of the modified sodium Auger parameter of $\alpha'_{Na} = (2062.11 \pm 0.14)$ eV found for the CISSe surface is similar to the value found in literature for a sodium compound on CISSe surfaces [7]. Upon deposition of 1 nm Na:In_xS_y buffer layer the Na 1s binding energy increases by about 0.3 eV, indicating a different chemical environment. For further buffer layer deposition, the position of the Na 1s feature remains constant within the error bar, while the kinetic energy of the Na KLL line increases. A direct assignment of the chemical Na species is diffi-

cult since no literature values are reported with corresponding Auger parameters. However, the change of the position of the Auger transition suggests a small alteration of the surface during the deposition process, which is not detectable with XPS. In general, this shift of the Auger kinetic energy can be assigned to a decrease in the Coulomb interaction U (see equation 2.5) during the deposition process.

After the heat treatment, the binding energy position of Na 1s decreases with respect to E_F while the kinetic energy position of the Na KLL Auger transition increases further. This leads to an annealing-induced increase of α'_{Na} by 0.47 eV to (2063.92 ± 0.07) eV. It was speculated that such a high α'_{Na} can be attributed to a compound, which consists of, e.g., Na-S or Na-Se bonds [62, 141, 142].

The modified indium Auger parameter is also investigated and plotted in Fig. 6.17. In comparison with the sodium Auger parameter the observed changes are small, i.e., 852.58 eV and 852.03 eV for CISSe (maximum) and for 3 nm Na:In_xS_y (minimum), respectively. The Auger parameter of the pristine CISSe absorber is in good agreement with literature values found for CIS and CISe. During Na:In_xS_y deposition α'_{In} first increases by 0.12 eV (for 1 nm Na:In_xS_y), which fits the value of In_2S_3 found by Sterner *et al.* [150]. For further increasing buffer layer thickness α'_{In} decreases to (852.1 ± 0.1) eV and remains constant until the maximum buffer layer thickness of 48 nm is reached. The determined modified In Auger parameter fits the one found by Moulder *et al.* for an In_2S_3 environment [62], though the respective binding and kinetic energies are slightly different. Furthermore, the α'_{In} of In_xS_y, i.e., sodium-free indium sulfide, is about 0.3 eV larger than the one found here. Hence, the influence of sodium for α'_{In} might explain the discrepancy with the literature values. Upon annealing, the modified In Auger parameter is increased by about 0.2 eV (open data point in Fig. 6.17). This increase is accompanied by a copper diffusion and hence the increase can be assigned to a Cu-In-S-like environment.

To quantitatively evaluate the chemical composition of each sample of the series, different peaks with similar kinetic energies, i.e., Se 3p and S 2p as well as In 4d and Se 3d and Cu 3p, were fitted simultaneously with Voigt profiles in order to minimize the error of possible adsorbates and analyzer transmission according to section 3.3. The computed results are plotted in Fig. 6.18. The filled points indicate the XPS intensity while the open data points illustrate the bulk-sensitive x-ray fluorescence (XRF) content. The XRF measurements were performed by S. Pohlner from AVANCIS with an S8 Tiger from Bruker which is equipped with a Rhodium anode. The XPS intensities behave as expected: the intensities of In, S, and Na increase with increasing buffer thickness while the ones of Cu and Se decrease. The surface S/In ratio stays constant above 6 nm Na:In_xS_y thickness at a value of about (1.2 ± 0.1) while the bulk S/In ratio is found to be 1.5 for the 48 nm thick sample. This

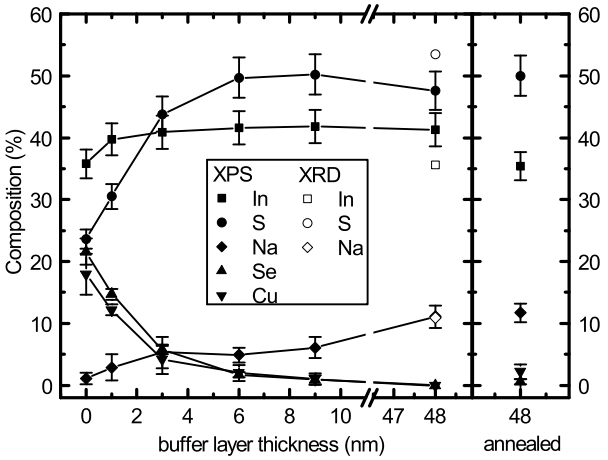

Figure 6.18: Surface composition of the sample sets determined with XPS (filled data points). Bulk composition measured with XRF (open points). The surface stoichiometry after annealing is shown in the right panel.

demonstrates again the sulfur-poor surface of the indium sulfide buffer layers. In addition, the bulk and surface sodium contents are in perfect agreement for the maximal buffer thickness. An XPS measurement with gracing emission ($\theta = 60\,^\circ$, not shown) reveals that the sodium distribution is homogeneous at the surface. This is in contrast to measurements performed by Barreau *et al.* [110], where an amount of sodium above 5 % accumulated at the surface of the investigated indium sulfide film, probably leading to a high surface oxidation and a decrease of the S/In ratio since oxygen is implemented on sulfur sites. Therefore, it is not surprising that only residual amounts of oxygen were found at the surface (see e.g., the Na:In_xS_y survey spectrum in Fig. 6.27). This demonstrates the excellent sample handling, where the total air exposure time of the samples was less than 15 min.

As indicated by the right panel in Fig. 6.18, the annealing step increases the surface S/In ratio to (1.4 ± 0.1) mainly due to a reduction of the indium content. In parallel, the sodium content stays at the same level as before the annealing step. Moreover, a weak copper and selenium diffusion occurs, increasing the surface contents to (2.2 ± 1.2) % and (0.6 ± 0.4) %, respectively. A striking result is that less than half of the copper is found at the surface in comparison with an undoped In_xS_y buffer layer (see section 6.1.1), which corroborates the reduction of the copper diffusion due to the introduction of sodium into the In_xS_y buffer layer.

To investigate the buried Na:In_xS_y/CISSe interface with particular focus on the copper diffusion into the buffer layer, XES measurements of the S $L_{2,3}$ and Cu $L_{2,3}$ edges were performed and are plotted in Figs. 6.19 and 6.20, respectively. The S $L_{2,3}$ spectra are

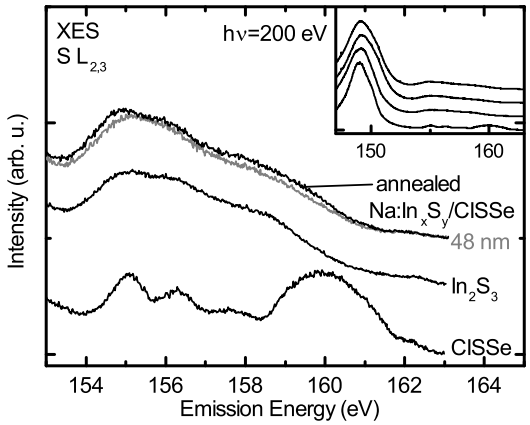

Figure 6.19: Non-resonantly ($h\nu = 200\,\text{eV}$) excited S $L_{2,3}$ emission of (from bottom to top): CISSe, co-evaporated In_2S_3, 48 nm Na:In_xS_y/CISSe (gray), and annealed 48 nm Na:In_xS_y/CISSe. The inset shows the same spectra with a wider energy range window including the S 3s $\rightarrow$ S 2p transition which was used for normalization.

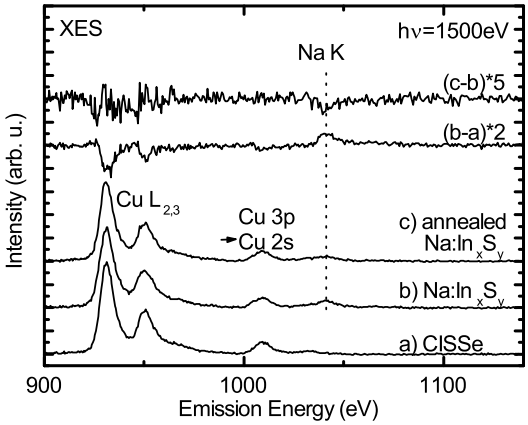

Figure 6.20: Cu $L_{2,3}$ and Na K XES spectra (excited with $h\nu = 1500\,\text{eV}$) of a) CISSe, b) Na:In_xS_y, and c) annealed Na:In_xS_y. The two topmost spectra show the deviation of (b-a) $\times 2$ and (c-b) $\times 5$. The spectra are aligned to the Cu $L_{2,3}$ emission and normalized to the measurement time and photon flux.

normalized to the S 3s $\rightarrow$ S 2p transition at 148 eV (see inset of Fig. 6.19). The spectrum of the 48 nm thick Na:In_xS_y/CISSe film is almost identical to the co-evaporated In_2S_3 spectrum. However, at about 155 eV emission energy, the Na:In_xS_y buffer exhibits some additional intensity, while the intensity is somewhat lower at 158 eV in comparison with the co-evaporated In_2S_3. Hence, the local chemical environment of the probed sulfur is similar to In_2S_3 but not identical. In addition, no Na_2S- or Na_2SO_4-related signals can be observed since both, sulfides and sulfates have a characteristic structure in this emission energy region. The changes of the spectrum after annealing are very small in comparison with the 48 nm thick Na:In_xS_y/CISSe sample. The slight spectral changes can be observed at about 154 eV and 159 eV where some additional intensity is found. These intensities can be assigned to the S $L_{2,3}$ CISSe spectrum and a superposition of $0.04 \times$ CISSe and $1.05 \times In_2S_3$ amount to the annealed spectrum. Using equation 6.1, a Cu/In ratio of (0.02 ± 0.01) can be computed. This value is slightly smaller than the XPS-derived value of 0.06 and significantly smaller than the Cu/In ratio of the pure annealed In_xS_y/CISSe interface of (0.25 ± 0.03). This result confirms the reduced copper diffusion due to the incorporation of sodium into In_xS_y.

Bulk-sensitive ($\lambda_{h\nu=1500\,eV} \approx 275$ nm) XES measurements of the Cu $L_{2,3}$ and Na K emission of the CISSe absorber, the 48 nm thick Na:In_xS_y/CISSe interface, and the annealed 48 nm thick Na:In_xS_y/CISSe interface are shown in Fig. 6.20. In addition, this energy window contains the Cu 3p $\rightarrow$ Cu 2s transition at about 1010 eV emission energy and the Ga $L_{2,3}$ emission lines are expected at about 1090 eV [182]. No gallium-related emission is detectable for all samples, pointing towards a Ga-free surface-near bulk region within the absorber, as it is well known for the AVANCIS absorber. For the CISSe spectrum (Fig. 6.20 a)), a prominent Cu $L_{2,3}$ emission and only a marginal Na K intensity can be observed. Upon deposition of the 48 nm Na:In_xS_y this copper signal is reduced by 10 %. This is demonstrated by subtracting a) from b) (see Fig. 6.20) with a magnification of two, where a "valley" occurs at the Cu $L_{2,3}$ energy position. This is accompanied by a strong Na K XES signal exhibiting additional intensity at about 1040 eV, which is due to the sodium containing buffer layer. Hence, the reduction of the copper signals can be understood due to the attenuation of the (almost) copper-free buffer layer. Although XPS and S $L_{2,3}$ XES measurements suggest some copper diffusion, the Cu $L_{2,3}$ emission stays constant upon annealing. This is visualized by the difference spectrum (c-b) $\times$ 5 (topmost in Fig. 6.20). Since at these high photon energies the attenuation plays only a minor role and the Cu interdiffusion is weak, the Cu peak is not affected by the annealing. A further observation is made when comparing the Na K signal from the annealed c) with the non-annealed b) spectrum. The difference spectrum demonstrates a clear reduction of the sodium-related intensity upon annealing, although the XPS intensity remains constant. This could tentatively be explained by a sublimation of a sodium compound, e.g., Na_2S into the vacuum or by diffusion of the Na into the absorber or towards the back contact.

6.2.2 Electronic properties

In the following, the band alignment of the Na:In_xS_y/CISSe interface is determined before and after annealing. As already confirmed in section 6.1.2, the diffusion of copper into the indium sulfide leads to a reduction of its band gap, while the incorporation of sodium in In_xS_y is expected to enhance the band gap. Correspondingly, optical measurements reveal a band gap which increases from $E_{Na:In_xS_y} = 2.1$ eV to 2.95 eV for sodium contents from 0 % to about 6 % (Na/In = 0.17), respectively [181]. A further increase of the sodium content shows no increase of the optical band gap. It should be noted that the here investigated Na:In_xS_y films have a larger sodium content than the ones studied from Barreau *et al.*, which are processed by a coevaporation of In, S, and NaF [110, 181]. Consequently, it is expected that the here investigated samples have different electronic and optical properties.

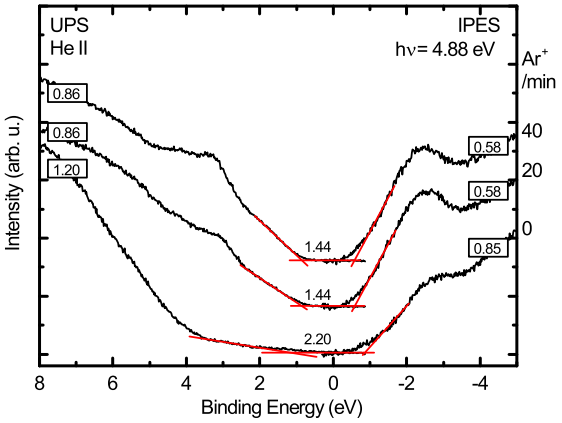

Figure 6.21: UPS/IPES spectra of the valence and conduction band of a CISSe absorber for increasing Ar^+ sputter times (50 eV, 80 nA/cm^2). The determined VBM, CBM, and surface band gaps are given in eV.

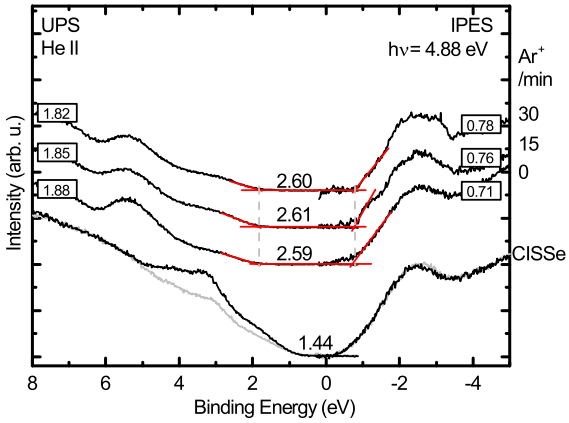

Figure 6.22: UPS/IPES spectra of the valence and conduction band of the Na:In_xS_y/CISSe interface as-received and for increasing Ar^+ sputter times (50 eV, 80 nA/cm^2). The bottommost spectra show the 20 min (gray) and 40 min Ar^+ (black) treated absorber as reference.

In addition, no direct UPS/IPES measurement of the band alignment of the Na:In_xS_y/CISSe interface has been published yet.

All investigated samples contain small amounts of carbon and oxygen contaminations at the surface due to the short ambient air exposure. To remove this contamination layer, the CISSe and Na:In_xS_y samples were cleaned with 50 eV Ar^+ ion treatment. In figures 6.21 and 6.22 the recorded valence band and conduction band spectra of the CISSe and Na:In_xS_y/CISSe samples are depicted, respectively. The band edges were determined via a linear extrapolation of the leading band edges. The CISSe sample was cleaned in several 20 minutes long treatment steps, while 15 minutes long steps were used for the Na:In_xS_y sample. Already after the first ion treatment step, a significant alteration of the shape of the valence band spectrum of the CISSe sample can be observed, which manifests in an increase of the intensity of the Cu 3d-derived band at about 3 eV. After a second sputter step the derived band gap value of $E^{Surf}_{Gap,CISSe} = (1.44 \pm 0.11)$ eV does not change further, but the intensity of the copper 3d-derived band increases, indicating an environment with even less contaminations. The surface band gap of the CISSe absorber is in good agreement with the absorber surface band gap of (1.45 ± 0.11) eV derived in section 6.1.2. However, for the unoccupied regime a clear foot at about $E_{Bind} = -0.50$ eV can be noticed, which is possibly due to indirect transitions or defect states.

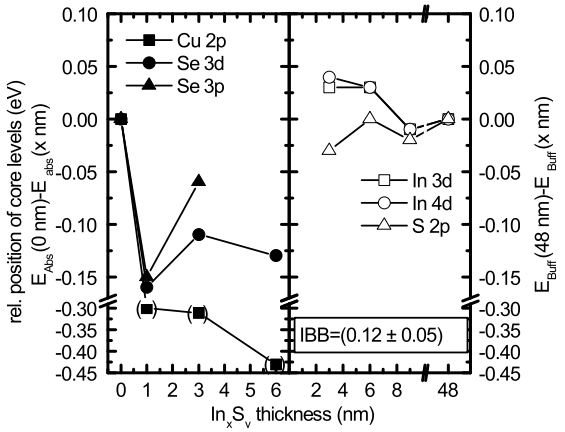

Figure 6.23: Interface induced band bending of the Na:In_xS_y/CISSe interface. The relative shifts of the core levels of the CISSe and Na:In_xS_y samples were determined.

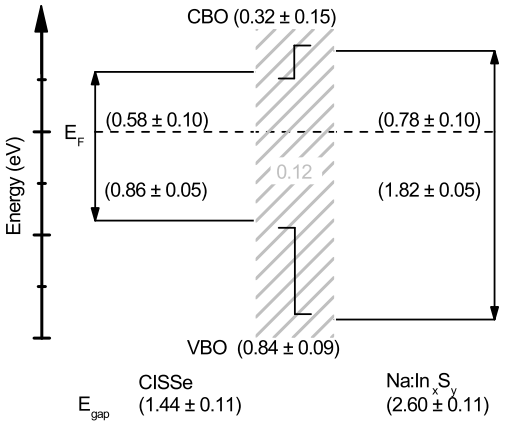

Figure 6.24: Schematic band diagram of the abrupt Na:In_xS_y/CISSe interface. The determined CBM and VBM are shown left and right for the absorber and Na:In_xS_y sample. The gray shaded area shows the IBB. Calculated band offsets are sketched as steps.

The Na:In_xS_y UPS/IPES spectra are shown in Fig. 6.22 for several sputter times. For comparison, the bottommost spectra show the absorber after 20 minutes (gray) and 40 minutes (black) of sputtering. For all Na:In_xS_y spectra only minor changes are noticed after each sputter step, which suggests an already clean surface of the as-received sample. At about $E_{Bind} = 5.4\,\text{eV}$ a prominent feature can be noticed, corresponding to In 5s- and In 5p-derived bands but also a small contribution of sulfur p states is reported [183]. After the second sputter step a surface band gap of $E^{Surf}_{Gap,Na:In_xS_y} = (2.60 \pm 0.11)\,\text{eV}$ is identified. From calculations by Lafond *et al.* [122] it is expected that the introduction of sodium into In_xS_y shifts the conduction band as well as the valence band away from E_F compared to pure indium sulfide. In fact, the UPS/IPES measurements show a significant increase of the VBM by almost 0.6 eV towards higher binding energies, whereas the CBM is shifted by $\approx 0.2\,\text{eV}$ to lower binding energies. Hence, the here determined band gap value is much larger than the one from indium sulfide and, despite the larger sodium amount (Na/In = 0.27), the determined band gap is in between the two in literature mentioned band gap values of 2.1 eV (Na/In = 0) and 2.95 eV (Na/In = 0.17) [181].

By comparing the CISSe CBM with the Na:In_xS_y CBM in Fig. 6.22, a first estimation of the band alignment at the Na:In_xS_y/CISSe interface can be given. With the values $\text{CBM}_{CISSe} = 0.58\,\text{eV}$ and $\text{CBM}_{Na:In_xS_y} = 0.78\,\text{eV}$, a clear spike of $(0.20 \pm 0.14)\,\text{eV}$ is calculated. However, the interface induced band bending has to be taken into account. Hence,

thin buffer layer thicknesses with not completely attenuated absorber core levels are used in order to follow the relative shift of the absorber and buffer core levels. As already mentioned for the determination of the IBB of pure In_xS_y in chapter 6.1.2, the indium and sulfur core levels of the CISSe absorber and the Na:In_xS_y buffer layer cannot be distinguished. Consequently, only the Se 3d absorber core level is taken whereas the copper core levels are neglected due to possible falsifying interdiffusion effects. For the buffer layer In- and S-related core levels were taken. Here, the IMFP λ is used as the minimal thickness at which the signal of the buffer significantly dominates that of the absorber. Accordingly, buffer layer thicknesses smaller than λ are not included in the determination. Fig. 6.23 displays the absorber-related shifts (left-hand side), as well as the shifts of the buffer core levels (right-hand side). In summary, a mean value of (0.12 ± 0.05) eV for the IBB of the Na:In_xS_y/CISSe interface is identified. This IBB increases the inversion of the absorber surface which is generally regarded to be beneficial for the solar cell performance [53]. The resulting band alignment is composed in Fig. 6.24. From this sketch a significant spike in the conduction band of (0.32 ± 0.15) eV and a valence band offset of (-0.84 ± 0.09) eV can be seen. It is argued that a moderate spike in the conduction band up to 0.3 - 0.4 eV is not deteriorating the performance of a solar cell [53, 55, 98].

In addition, the situation of the band alignment of the Na:In_xS_y/CISSe interface in real solar cells is even more complicated. As mentioned earlier, an annealing step is conducted during the subsequent solar cell process. As discussed above, this leads to a copper and a selenium diffusion. Accordingly, UPS/IPES measurements were also performed on an *in-situ* annealed 48 nm thick Na:In_xS_y/CISSe sample. They are shown in Fig. 6.25 c). The clean CISSe and non-annealed Na:In_xS_y samples are depicted as reference spectra in Fig. 6.25 a) and b), respectively. In general, the annealed Na:In_xS_y spectrum has a similar spectral shape as the non-annealed Na:In_xS_y. However, the annealed spectrum c) exhibits a broad feature at about 2 eV, resulting in a significant smaller VBM of (1.32 ± 0.05) eV. This feature can be related to Cu 3d-derived bands [123]. Hence, already the small amount of copper (about 2 %) leads to a significant reduction of the VBM. In addition, the CBM remains constant at (-0.79 ± 0.10) eV, which is in contrast to the findings by Barreau *et al.* [121]. Based on indirect methods (XPS and optical measurements) they proposed that the CBM moves closer to the Fermi level due to an intercalation of copper in $NaIn_5S_8$ films [123]. However, as it is stated in section 6.2.1, the annealed Na:In_xS_y samples show a small increase of sulfur/decrease of indium which suggest a decrease of the n-character of indium sulfides [155]. Both findings could explain why the position of the CBM does not change after annealing. With the CBM and VBM of the annealed Na:In_xS_y and the band edges of the CISSe absorber a significant spike-like conduction band offset of (0.21 ± 0.14) eV is calculated. For the valence band, an offset of (-0.46 ± 0.07) eV is derived. The band

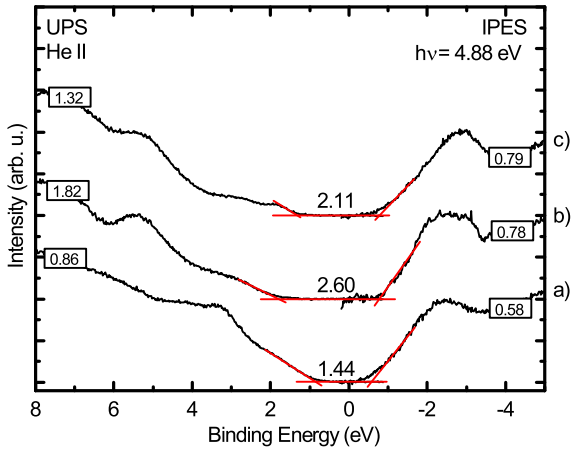

Figure 6.25: UPS/IPES spectra of the clean valence and conduction band of a) CISSe, b) Na:In_xS_y, and c) annealed Na:In_xS_y. The annealing step reduces the band gap significantly. Determined values are given in eV.

alignment at the hidden interface is sketched in Fig. 6.26. A complete description of the interface is, however, difficult. On the one hand, the copper diffusion is still apparent, but at the surface reduced in comparison with the In_xS_y buffer. On the other hand, the observed selenium diffusion might also alter the hidden interface. Hence, a Se and Cu depleted CISSe surface is suggested. It is assumed that both increase the absorber surface band gap, in which the Se shifts the CBM [47, 184] and the Cu the VBM [47, 100] away from the Fermi level. In consequence, the CBO and the VBO are reduced. Furthermore, the incorporation of Se and Cu in the Na:In_xS_y buffer in the vicinity of the interface probably makes the buffer more CISSe-like suggesting that the band edges of the absorber and buffer approaching to each other.

The impact of the Se diffusion is illustrated by the gray bar at the conduction band absorber site in Fig. 6.26. However, it can only be speculated about the size of this shift. As an upper limit, the band structure a of selenium-free absorber, e.g., Cu(In,Ga)S_2 can be taken. UPS/IPES measurement revealed a surface band gap of a Cu(In,Ga)S_2 absorber of (1.76 ± 0.15) eV with a CBM of (0.86 ± 0.1) eV [184]. This value is very similar to the conduction band extremum of the annealed Na:In_xS_y sample. Hence, a small spike e.g., up to 0.2 eV [61] or even a flat conduction band alignment might occur, which is in agreement with the reported high performance of up to 17.1 % [6]. Such a small spike might merely act as a tunneling barrier or might even be overcome thermally by electrons [52, 61]. The impact of the Cu diffusion is also indicated as a gray bar at the valence band absorber site in Fig.

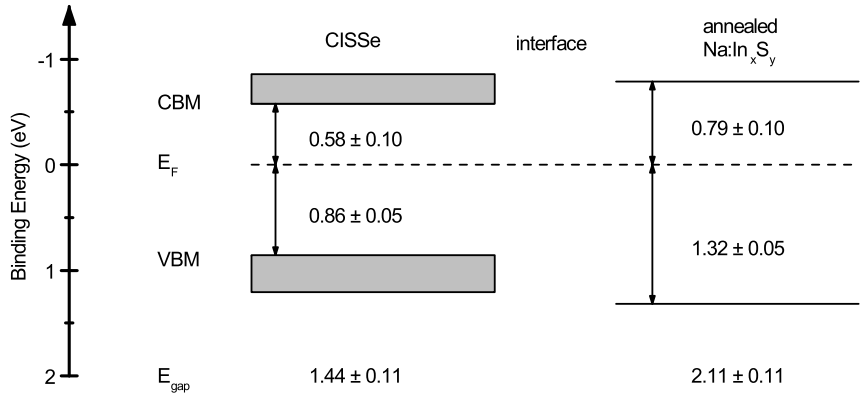

Figure 6.26: Schematic band diagram of the annealed Na:In_xS_y/CISSe interface. The solid lines of the CISSe absorber illustrate the VBM and CBM in the non-annealed case. The gray areas indicate possible alterations upon annealing at the hidden interface.

6.26. A band gap widening for a $CuInSe_2$ absorber due to a copper depletion was estimated to be about 0.3 eV [100].

Tab. 6.2 summarizes the derived VBM and CBM positions of the In_xS_y and Na:In_xS_y buffer layer as well as the CdS reference buffer layer. In the following, it is discussed why Na:In_xS_y buffered Cu(In,Ga)$(S,Se)_2$-based solar cells are performing better than In_xS_y buffered and even better than CdS containing solar cells. The high-performance of cells with a CdS buffer layer is often attributed to i) a cleaning of the absorber surface during the chemical bath deposition and ii) a flat band alignment at the CdS/CISSe interface [9]. A flat alignment (or modest spike-like offset) was also measured for an In_xS_y buffer (e.g., 42 % indium content) in section 6.1.2. However, in this case the surface band gap of the In_xS_y layer after the annealing step is significantly smaller than the CdS band gap, leading to a lower optical transmission in the low wavelength regime and hence to a smaller efficiency. Furthermore, contaminations of the absorber surface have to be taken into account since no additional cleaning step is provided during the solar cell production. These possibly act as recombination centers at the interface.

For the Na:In_xS_y buffer, the band gap at the surface after annealing is larger than the one of In_xS_y, but it is still smaller than the CdS band gap. In addition, a clear spike-like band alignment was measured at the Na:In_xS_y/CISSe interface. However, it is likely that the copper accumulation at the indium sulfide buffer surface [178, 179] leads to a smaller surface band gap, while the bulk band gap is significantly larger. Moreover, a copper-depleted CISSe surface is expected which is accompanied by reduced interface recombination [53]. In addition

Table 6.2: Comparison of the determined band edge values, surface band gaps, and the efficiency of the best certified solar modules obtained with a Na:In_xS_y and In_xS_y buffer layer. As reference, results for a CdS buffer layer are listed.

buffer layer	Na:In_xS_y	In_xS_y	CdS
cleaned			
CBM (eV)	0.78	0.59	0.5 [9]
VBM (eV)	1.82	1.75	1.9 [9]
E_{Gap}^{Surf} (eV)	2.60	2.34	2.4 [9]
annealed			
CBM (eV)	0.79	0.78	
VBM (eV)	1.32	1.17	
E_{Gap}^{Surf} (eV)	2.11	1.95	
η (%)	16.6 [6, 111]	13.4 [6, 159]	15.8 [93]

to the copper diffusion, a pronounced selenium diffusion from the absorber into the buffer layer is found. This might shift the conduction band of the absorber away from E_F leading to a better band alignment at the buffer/absorber interface. All these facts might explain the higher transmission in the low wavelength regime [6] of Na:In_xS_y in comparison with CdS buffered and hence the better solar cell efficiency of Na:In_xS_y buffered chalcopyrite absorbers.

6.3 The i-ZnO/Na:In_xS_y interface

A transparent front contact, i.e., a window layer, should primarily transmit light which is then available for creating charge carriers at the absorber's site. Further demands on such a window layer are: 1) a low resistant contact and 2) preventing shunts [185]. In order to fulfill these requirements a layer stack of i-ZnO (not deliberately doped = intrinsic) and n-ZnO (aluminum doped) is deposited onto the buffer, as mentioned earlier in section 4.1. Typically, the $\approx$ 100 nm thick i-ZnO window is deposited via sputtering onto the buffer. Here undoped ceramic targets are used, which allow only radio frequency (r.f.) magnetron sputtering [94]. Details concerning r.f. sputtering can be found e.g., in Refs. [93, 186, 187] and references therein. Although the i-ZnO is important for reproducibility, it acts as diffusion barrier of the n-ZnO dopant into the buffer, and it prevents degradation, the full role of the i-ZnO layer is still not fully understood [56, 185, 188, 189].

In this context it is somehow surprising that the ZnO and especially the more important i-ZnO/buffer interface has not attracted a lot of research interest. In the few existing studies, for the i-ZnO/CdS interface a flat band alignment was found [190] as well as the creation of ZnS/ZnSe at the ZnO/$CuIn(S,Se)_2$ interface [191]. Moreover, it was revealed that for an $In(OH_x,S_y)$ CBD deposited buffer a deterioration of all solar cell parameters are caused by the ZnO/$In(OH_x,S_y)$ interface [192]. Furthermore, for a PVD deposited In_xS_y buffer it was suggested that the solar cell improvement by a post-annealing treatment is related to the ZnO/In_xS_y interface [163]. As the i-ZnO/Na:In_xS_y interface plays an important role for the efficiency of the solar cell, the chemical and electronic properties of this interface are investigated in the following section. For that purpose, samples with different r.f. sputtered i-ZnO thicknesses (1 nm, 3 nm, 5 nm, 10 nm, 50 nm, and 100 nm) are deposited onto a 48 nm Na:In_xS_y/CISSe sample at the AVANCIS pilot line in Munich. This sample stack was sealed under a nitrogen atmosphere and sent to Würzburg to minimize the influence of the ambient environment.

6.3.1 Chemical properties

Selected i-ZnO/Na:In_xS_y XPS survey spectra compared to that of a 48 nm thick Na:In_xS_y/CISSe sample are depicted in Fig. 6.27. For increasing i-ZnO thickness the buffer lines (i.e., indium and sulfur) are attenuated and at 10 nm i-ZnO the most prominent In 3d signal vanished, implying a closed i-ZnO cover layer. In parallel, the Zn-related and oxygen-related peaks increase. For thicknesses larger than 10 nm i-ZnO, the spectra are almost

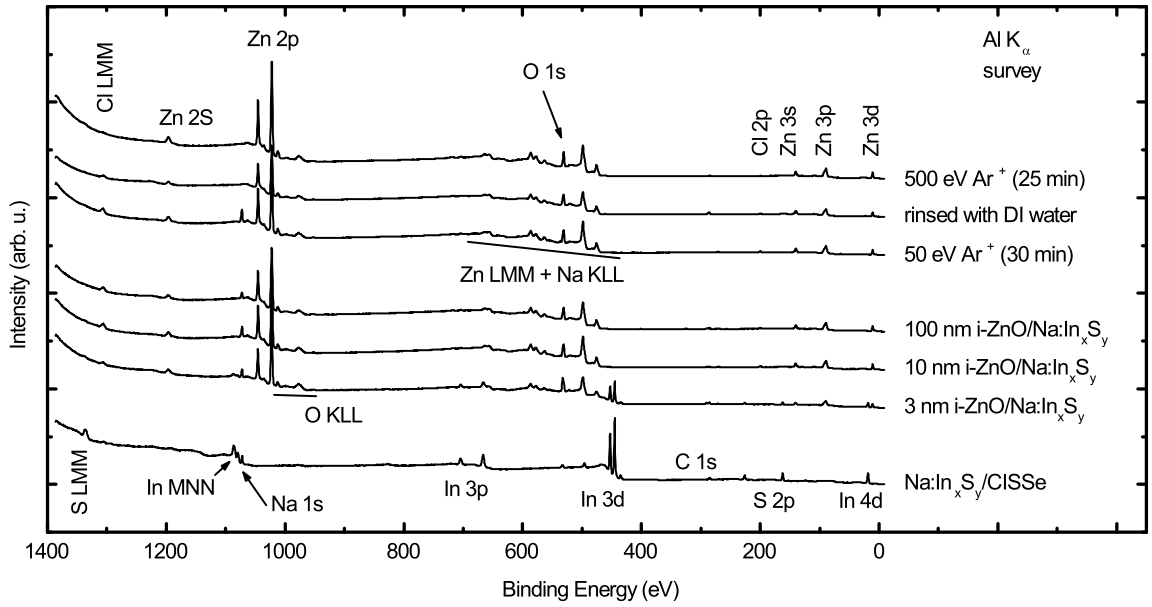

Figure 6.27: Al K_α excited XAES/XPS survey spectra of Na:In_xS_y/CISSe and of different thicknesses of the i-ZnO window layer. The three uppermost spectra show different cleaning treatments of the 100 nm i-ZnO sample. Prominent signals are labeled.

identical (except for carbon contamination). In contrast to the indium and sulfur signals which are attenuated with increasing window layer thickness, the Na 1s line intensity even increases and reaches a maximum at 5 nm i-ZnO. For further increasing i-ZnO thickness, the Na 1s intensity decreases and at 100 nm i-ZnO reaches a value which is about 80 % that of the Na:In_xS_y buffer reference. This result suggests that sodium of the Na:In_xS_y buffer layer is floating to the surface of the i-ZnO layer. It is well known that sodium accumulates at surfaces and grain boundaries of chalcopyrite absorbers [11, 141, 193, 194]. In addition, diffusion of sodium towards the ZnO surface was observed by Erfurth [41] and the elevated temperatures of, e.g., the sputtering processes may also lead to an enhanced segregation of sodium [194]. However, a negative effect for the solar cell's efficiency is reported when ZnO is directly sputtered onto Na-containing CISSe which is possibly due to a reduced crystallite creation [41]. Hence, a possible influence on the solar cell performance of the sodium on the growth properties of the i-ZnO has to be taken into account.

Besides that, one should also note the remarkable appearance of chlorine-related peaks for all i-ZnO samples visible for instance as the Cl LMM Auger line at $E_{Bind} \approx 1307$ eV (for Al K_α), corresponding to $E_{Kin} \approx 146$ eV. A second series of the sample series exhibits the same amount of chlorine in the XPS survey spectra suggesting a non-deliberated built-in contamination. In order to remove this contamination, several attempts were executed on

the 100 nm i-ZnO sample, which are shown in the three upper spectra in Fig. 6.27. In fact, sputtering for 30 min with 50 eV Ar^+ ions leads to a more pronounced Cl LMM Auger line due to the removement of surface adsorbates. After a subsequent *ex-situ* rinsing of the sample with deionized (DI) water several changes appear. On the one hand, the sodium intensity has completely vanished. This finding of a H_2O induced removement of sodium is in agreement with Ref. [96]. On the other hand, the chlorine intensity is reduced. However, this probably originates from more surface contaminations. Therefore, the sample was again sputtered, now with 500 eV for 25 min. This finally removed the chlorine from the surface (topmost spectrum), implying that the chlorine is chemically bound at the surface of i-ZnO. However, this does not clarify the origin of the chlorine. The sputter targets have a Cl contamination in the ppm-range, which is probably too small to explain the surface contamination. Accordingly, the residual gas of the production chamber has to be taken into account which might incorporate chlorine during the ZnO sputtering process. However, in this case no negative effects for the solar cell efficiency are known suggesting that the influence of chlorine is negligible for the performance of the solar cell.

Chemical environment of zinc

At the interface between ZnO and sulfur-containing absorbers, the creation of ZnS as well as an interdiffusion of zinc atoms are reported [191, 195]. Correspondingly, the formation of, e.g., sulfides and/or sulfates at the i-ZnO/Na:In_xS_y interface is investigated in the following. For this purpose, the Zn $L_3M_{45}M_{45}$ and Zn $2p_{3/2}$ signals are plotted as a function of increasing window layer thickness in Fig. 6.28 a). The samples are shortly cleaned with a 50 eV Ar^+ ion treatment for minimizing the influence of adsorbates. For the pure buffer layer, the Na KLL signal is observed, which overlaps energetically with the Zn LMM. Hence, the Na KLL is visible for thick i-ZnO as a shoulder at higher kinetic energies and a possible influence for the determination of the Zn LMM peak position is considered by the error bar. From the 1 nm to the 100 nm i-ZnO sample the Zn LMM transition shifts by approximately 0.6 eV to smaller kinetic energies. This can be related to a changing chemical environment of the zinc atoms from a ZnS-like to a ZnO environment. This is illustrated by gray bars, which mark the energy ranges commonly found in literature for ZnS, ZnO, and $Zn(OH)_2$ [22, 24, 62, 195–197]. In addition, a comparison of the spectral shape of the Auger peaks reveals an asymmetric shape of the three thinnest layer spectra suggesting at least two Zn components, e.g., ZnS and ZnO. However, it is not possible to reproduce a thin layer spectrum with a superposition of a ZnO and ZnS spectrum which is possibly due to the non-negligible influence of the Na KLL transition. In the case of the Zn $2p_{3/2}$ peak, a clear shift to smaller binding energies by about 0.5 eV can be observed for i-ZnO thicknesses up

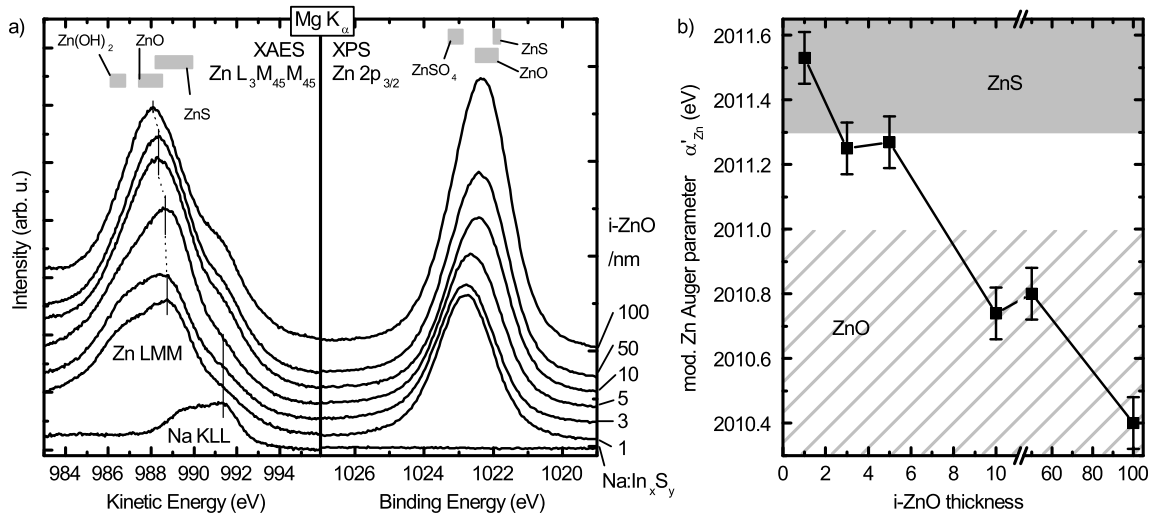

Figure 6.28: a) Mg Kα excited zinc XAES and XPS spectra for several i-ZnO layers with increasing thickness from bottom to top. The gray bars indicate energy ranges commonly found for $Zn(OH)_2$, ZnO, ZnS, and $Zn(SO)_4$ [22, 24, 62, 195–197]. b) Calculated modified Auger parameter α'_{Zn} for several i-ZnO thicknesses. For increasing i-ZnO thickness a clear decrease for α'_{Zn} is visible. The gray areas mark the energy ranges of the modified Zn Auger parameter calculated from literature for ZnS and ZnO.

to 10 nm. For higher thicknesses the peak position remains constant at $E_{Bind} = 1022.38$ eV indicating the formation of ZnO. The modified Zn Auger parameter α'_{Zn} is calculated from the shown Zn LMM and Zn $2p_{3/2}$ signals with the help of equation 2.6 and is plotted in Fig. 6.28 b). The gray and hatched areas mark the range for ZnS and ZnO, respectively, which were calculated from the literature [22, 24, 62, 195–197]. The three thinnest layers (from 1 nm - 5 nm) are in the ZnS energy range whereas the samples above 10 nm i-ZnO thickness can be assigned to ZnO. Although the Auger parameter of $Zn(OH)_2$ is also found in this energy region, its relevance can be ruled out since the kinetic energy of the Zn LMM Auger peak is too high (see the XAES spectrum in Fig. 6.28). Furthermore, the formation of $ZnSO_4$ cannot be ruled out since the expected Zn $2p_{3/2}$ core level position of $ZnSO_4$ [62] is similar to the found core level positions of the 1 nm and 3 nm i-ZnO layer thickness.

To further investigate possible intermixing at the interface as a result of the sputtering process, the sulfur-related spectra are analyzed. The evolution of the XPS S 2p signal is shown in Fig. 6.29. The main intensity at about 162 eV can be directly assigned to a S^{2-} (sulfide) bonding, e.g., indium sulfide (In_2S_3). This intensity decreases with increasing i-ZnO thickness in accordance with the nominal layer thickness. In addition, a second component can be observed at $E_{Bind} \approx 170$ eV, for 1 nm to 5 nm thickness indicating the formation of

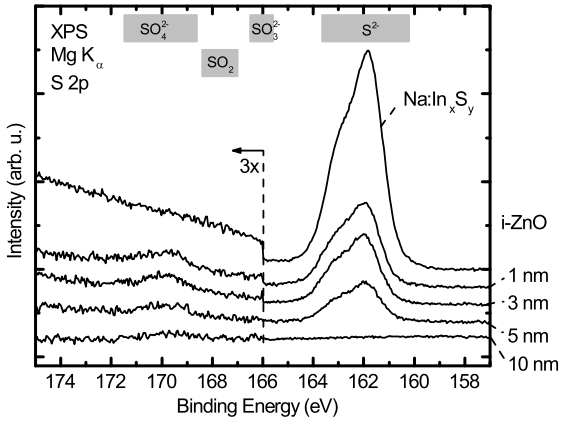

Figure 6.29: S 2p spectra for Na:In$_x$S$_y$ and different i-ZnO thickness. Binding energies $\geq$ 166 eV are magnified by a factor of three. Upon i-ZnO deposition a clear sulfate formation is detected. Gray bars mark the energy range commonly found for typical sulfur compounds [62].

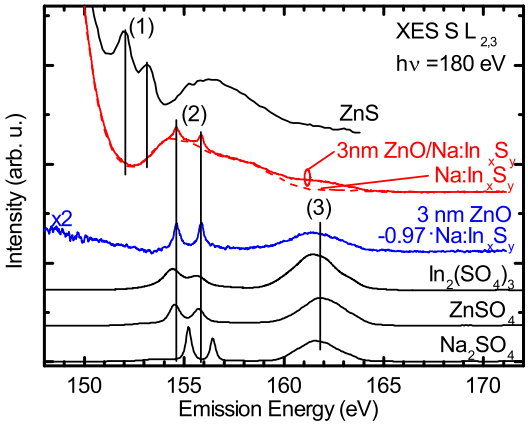

Figure 6.30: S L$_{2,3}$ XES spectra of a 3 nm i-ZnO/Na:In$_x$S$_y$ (red solid) and Na:In$_x$S$_y$ samples (red dashed). The deviation of the 3 nm i-ZnO from 0.97 $\times$ Na:In$_x$S$_y$ is illustrated by the blue line. The uppermost spectrum shows a ZnS spectrum (taken from Ref. [198]) and the three bottom spectra represent different sulfate references. For further details see text.

sulfate (SO_4^{-2}). For the 10 nm i-ZnO sample, however, a statement concerning sulfate is difficult since the signal is at the detection limit of XPS. Thus, the impact of Zn and O atoms probably breaks In-S bonds and form subsequent Zn-S and/or O-S bonds. This is further confirmed by S L$_{2,3}$ XES measurements of these samples which are shown in Fig. 6.30. The 3 nm i-ZnO/Na:In$_x$S$_y$ spectrum highlights the characteristic sulfate peaks (marked with (2)), as it reveals the formation of S-O bonds [136]. To be more precise, S 3s-related states decay into S 2p core holes, which are chemically shifted due to the bonding to oxygen. To isolate the sulfate component, the pristine Na:In$_x$S$_y$ (scaled with a factor of 0.97) is subtracted from the 3 nm i-ZnO/Na:In$_x$S$_y$ spectrum (dashed red spectrum). The resulting spectrum is shown underneath in blue. Here, a further characteristic feature at about 162 eV becomes obvious, which is marked with (3). This feature stems from S 3d-related states, which become occupied in the consequence of the S-O bonds [132, 171, 199]. A comparison of the determined spectrum with possible candidates that are formed at the interface, namely Na_2SO_4, $ZnSO_4$, and $In_2(SO_4)_3$, demonstrates that the S 3s transition into the S 2p$_{1/2}$ ($E_{Em} \approx 156$ eV) core hole is much stronger than expected. In addition, the S L$_{2,3}$ spectra from different sulfates appear very similar. However, small differences can be noticed, for instance the shift of

feature (2) for Na_2SO_4 by 1 eV towards higher emission energies. Hence, by comparing the spectral shape of the S $L_{2,3}$ XES spectra the most likely compounds which are formed are $ZnSO_4$ and/or $In_2(SO_4)_3$.

The topmost spectrum in Fig. 6.30 presents a ZnS S $L_{2,3}$ emission spectrum, which exhibits two characteristic features (labeled with (1)). These features stem from a transition of the Zn 3d-derived state to the S 2p core holes. In contrast to the modified Auger parameter α'_{Zn} presented in Fig. 6.28 no indication for a formation of ZnS in the S $L_{2,3}$ emission spectrum is found. This discrepancy can be explained as follows: during the i-ZnO sputter process zinc sulfide is formed. The Zn XPS measurements were conducted prior to the S 2p spectra. During this measurement time the x-ray gun provides energy leading to a slow transformation of ZnS to $ZnSO_4$. Hence, a ZnS-related Auger parameter and a sulfate-related peak can be observed in the XPS measurements (Figs. 6.28 and 6.29). In comparison, the much higher flux at the synchrotron facility leads to a much faster transformation from sulfide to sulfate in XES measurements and accordingly only SO_4^{2-}-related emission can be detected (Fig. 6.30). This explanation is further supported by photo-induced sulfate formation at a Zn(O,OH)/Cu(In,Ga)(S,Se)$_2$ interface with [135, 136] and without additional provided water [132, 136].

Influence of the temperature on the chemical properties of the i-ZnO layer

In the previous sections, the diffusion processes caused by a thermal treatment at the In_xS_y/CISSe and Na:In_xS_y/CISSe heterostructures were investigated without additional cover layer. However, a possible impact of the i-ZnO/n-ZnO window layer structure of the full device has to be taken into account, in particular, as the i-ZnO and n-ZnO layer are deposited at elevated temperatures. In order to shed light on the chemical properties of the buried i-ZnO/Na:In_xS_y interface, a sample with 100 nm i-ZnO was annealed in UHV at 150 °C for 30 min and cut into two pieces. One of these pieces was annealed at 200 °C for 30 min and divided again, whereas one piece underwent another thermal treatment at 250 °C for 30 min. Each left-over piece was mounted onto one sample holder, sealed under nitrogen atmosphere and shipped to the ALS, Berkeley for XES measurements.

As mentioned above, one major function of the i-ZnO layer is being a diffusion barrier for absorber and/or buffer elements. As it was already shown, sodium floats onto the i-ZnO layer. Fig. 6.31 shows the Cu $2p_{3/2}$ and O 1s signals of the as-received 100 nm i-ZnO sample and the sample which underwent 250 °C for 30 min. A linear background was subtracted for the spectra. As reference, also the Cu $2p_{3/2}$ of the annealed Na:In_xS_y is shown without an i-ZnO layer. Neither the as-received i-ZnO sample nor the 250 °C sample reveal any

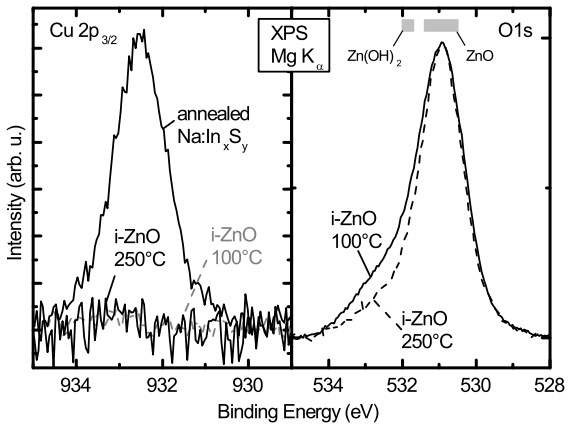

Figure 6.31: XPS Mg K_α Cu $2p_{3/2}$ and O 1s spectra of the 100 nm as-received i-ZnO and after an 250 °C treatment. For comparison the Cu $2p_{3/2}$ of the annealed Na:In_xS_y sample is plotted. Gray bars mark the commonly found literature values of ZnO and $Zn(OH)_2$ [200, 201].

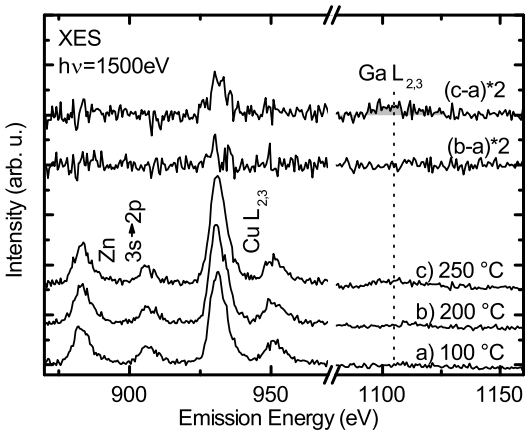

Figure 6.32: Cu $L_{2,3}$, Zn 3s → 2p, and Cu $L_{2,3}$ XES spectra excited with $h\nu =$ 1500 eV of 100 nm i-ZnO a) as-received ($\simeq$ 100 °C), b) annealed at 200 °C for 30 min, and c) annealed at 250 °C for 30 min. The two topmost spectra show the deviation of (b-a) and (c-a). For a quantitative analysis the spectra are aligned and normalized to the Zn 3s → 2p emission.

copper intensity. This is a first hint that no strong copper diffusion into the i-ZnO layer occurs upon annealing, since the copper intensity of the annealed Na:In_xS_y corresponds to a surface content of about (2 ± 1) %. The O 1s signal illustrates two main components: the main intensity at about 530.9 eV can be assigned to ZnO, whereas the second component belongs to $Zn(OH)_2$. The zinc hydroxide is transformed under x-rays into ZnO and water [198]. For better comparison the plotted spectra are normalized to the ZnO peak maximum. Analyzing the spectra reveals that the $Zn(OH)_2$ component is reduced due to x-ray radiation and the heat treatment. In addition, the reduction of the hydroxide component can possibly be referred to the desorption of water where the O 1s signal is located at 533.7 eV binding energy [137]. After the annealing step the i-ZnO layer exhibits a $Zn(OH)_2$ component of about (11 ± 2) %. This is in perfect agreement with the findings of L. Weinhardt [198] who found an upper limit of 12 % $Zn(OH)_2$ fraction.

In Fig. 6.32, the XES spectra of the 100 nm i-ZnO samples are shown (a) as-received, b) after heating to 200 °C, and c) after heating to 250 °C). The XES spectra exhibit the Zn 3s → 2p, Zn $L_{2,3}$, Cu $L_{2,3}$, Na K, and Ga $L_{2,3}$ emission in the energy range of 850 eV - 1160 eV. For the sake of clarity, the Zn $L_{2,3}$ and Na K emission lines are not shown. All

spectra are normalized to the Zn 3s → 2p transition. Note that the 150 °C sample shows a significant larger copper intensity compared to the 200 °C sample, even though the 200 °C underwent the 150 °C treatment, too. This is possibly due to a scratch at the sample towards the absorber leading to a larger copper intensity. Therefore, the 150 °C sample is not shown and neglected for this discussion. In order to disclose the chemical changes due to the heat treatment, difference spectra were calculated which are shown at the top of Fig. 6.32. After annealing to 200 °C, a clear increase of the Cu $L_{2,3}$ signal ((b-a)×2) appears which can be attributed to the copper interdiffusion from the absorber into the buffer. By doing the same procedure at 250 °C ((c-a)×2, topmost spectrum) an even larger amount of copper can be seen. This is in accordance with Ref. [125], where a strong dependence of the copper intensity in the buffer on the annealing temperature was measured. In addition to the copper intensity increase, a small gallium-related signal is observed after the 250 °C annealing step. Since the buffer and window layer deposition does mostly not exceed the temperature of 200 °C, the here monitored Ga diffusion is not relevant for the final solar cell. In case of reaching or even exceeding the 200 °C in future developments, the Ga-diffusion has to be considered.

Combining the XPS and XES measurements it becomes apparent that copper diffuses into the buffer, but probably not into the i-ZnO layer. To shed light on the buried annealed i-ZnO/Na:In_xS_y interface, the window layer was etched with acetic acid (CH_3COOH), diluted with 50 % deionized water. Subsequently, the non-annealed and annealed 100 nm i-ZnO window layer was removed by dipping the samples into the diluted acetic acid for 1 minute and 5 minutes, respectively. Afterwards the samples were rinsed with deionized water and dried by nitrogen gas. The XPS low binding energy spectra of the non-annealed and annealed samples are plotted in Fig. 6.33. These spectra were satellite corrected in order to disentangle the Mg K$\alpha_{3,4}$ [202] excited Zn 3p lines from the Cu 3p signal. Spectrum a) shows the non-annealed 100 nm i-ZnO samples and b) the etched 100 nm i-ZnO. After the etching step of the non-annealed sample the Zn-related peaks vanish. Furthermore, the Na 2s and Na 2p signals are removed, which is in accordance with the removement of sodium from a chalcopyrite surface by an H_2O rinse [203], whereas it is not clear whether the acetic acid or the rinsing with deionized water removes sodium. In addition, the indium and sulfur intensities appear, which indicates that the complete ZnO layer has been removed. In contrast, no copper-related intensity is found. For a comparison of the etched i-ZnO with a cleaned 48 nm thick Na:In_xS_y sample the difference spectrum (c-b) × 4 is calculated. Spectrum b) was shifted by 0.11 eV prior to the subtraction in order to fit the In 4d peak of spectrum c). This clearly demonstrates the removal of sodium, as well as a decrease of the indium intensity. A small "valley" can be found at the Se 3d energy position (≈ 55 eV), which already suggests a selenium diffusion upon the 100 °C deposited i-ZnO layer. A possible etching

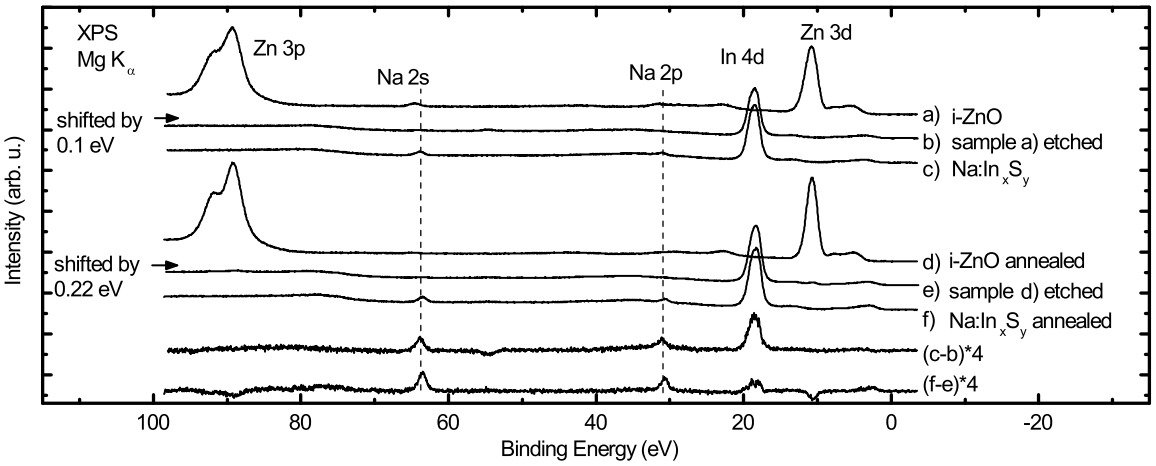

Figure 6.33: Mg K_α excited low binding energy regime of a a) 100 nm i-ZnO sample, b) an 50 % acetic acid etched i-ZnO sample, and c) a Na:In_xS_y buffer layer reference. d)-f) display the annealed samples of i-ZnO, etched i-ZnO, and the annealed Na:In_xS_y buffer, respectively. The difference spectra (bottommost) illustrate the deviations of the etched and reference samples. b) and e) were shifted in order to align the In 4d signal of each reference spectrum. Prominent photoemission signals are labeled.

towards the absorber surface and hence a Se signal originating from the absorber can be ruled out since no copper-related intensity is found in the difference spectrum.

The same procedure was performed for the 200 °C annealed i-ZnO sample d). After the etching step only residual Zn-related intensity is observed e). Similar to the non-annealed sample, the complete sodium has vanished and indium and sulfur peaks appear. Upon etching, the Se 3d and Cu 3p intensities are similar compared to the annealed Na:In_xS_y reference sample f). This is corroborated by the difference spectrum of (f-e) $\times$ 4. Here, no spectral changes at the Cu 3p and Se 3d energy positions are visible. In addition, at the energy positions of sodium and indium additional intensity is noticed, which is comparable with the non-annealed i-ZnO sample. At the Zn energy positions a "valley" occurs implying a residual amount of the window layer. By comparing the 1 nm ZnO/Na:In_xS_y spectrum with the Zn intensity here, the residual amount can be estimated to be less than a monolayer. The latter results clarify that copper and selenium diffuse throughout the Na:In_xS_y buffer layer but stop at the i-ZnO/Na:In_xS_y interface. Furthermore, no increased or reduced diffusion of these elements in comparison with the uncapped Na:In_xS_y buffer can be detected. Hence, the investigation of the different buffer layers without the ZnO window layer is justified.

6.3.2 Electronic properties

As discussed above, the role of the window layer, in particular the i-ZnO layer, is not fully understood yet. Besides the chemical properties, the band alignment at the buffer/window interface plays an important role since electrons have to be transported to the front contact (n-ZnO). For the (still) state-of-the-art i-ZnO/CdS interface a flat band alignment was determined directly with a combination of UPS and IPES by Weinhardt *et al.* [190]. Nguyen and coworkers found a huge amount of acceptor-like defect states for a chemical bath deposited In(OH_x,S_y) buffer at the ZnO/In(OH_x,S_y) interface leading to a bad solar cell performance [192]. It was suggested that the beneficial effect of the post-annealing step alters these defects [163]. However, for the sodium-doped indium sulfide buffer layer used here no investigation of the band alignment at the interface with i-ZnO is reported so far.

In the following, the band alignment of the i-ZnO/Na:In_xS_y interface as it is formed in the solar cell is investigated. An UPS/IPES study of the Na:In_xS_y buffer layer was already presented in section 6.2.2 and the derived values of the CBM and VBM of the clean (30 min Ar^+ treated) and annealed (200 °C for 30 min) Na:In_xS_y buffer are shown for comparison in Fig. 6.34 (bottom spectrum). For the measurement of the valence region, the 100 nm i-ZnO sample was excited with the He II line. However, the He II excitation has a strong satellite at higher excitation energy (He II β, about 7.4 eV higher than He II α [204]) which gives additional intensity from the Zn 3d level in the region of the VBM. This leads to a big foot at around $E_{Bind} \approx 3$ eV which makes it difficult to determine the true VBM. Furthermore, the 100 nm i-ZnO sample shows a bad conductivity ($\approx 7 \cdot 10^{-7}$ S/cm [205]). With this conductivity as well as the measured sample current of about 10^{-9} A and 10^{-6} A for UPS and IPES, respectively, a surface charging can be estimated which is in the order of one volt for the IPES measurement.

Correspondingly, the 10 nm i-ZnO/Na:In_xS_y sample is measured with UPS (He I) and IPES which is shown in Fig. 6.34. With this combination, no charging effects and additional excitations in the investigated region are observed. The untreated 10 nm i-ZnO spectrum does not show a pronounced band edge, neither in the occupied nor in the unoccupied region. This suggests that the spectrum is dominated by surface contaminations. Therefore, the sample was cleaned and the band gap strongly decreases within the first cleaning step. Further sputtering does not alter the spectra significantly. Hence, the spectrum of the 10 nm thick i-ZnO sample after 30 min of Ar^+ treatment is used for the determination of the band alignment. The derived CBM is (0.59 ± 0.10) eV and the VBM is (3.03 ± 0.05) eV, which gives a surface band gap value of $E^{Surf}_{Gap,i-ZnO} = (3.62 \pm 0.11)$ eV. This determined band gap value is slightly larger than the common accepted optical bulk value of 3.3 eV - 3.4 eV [206,

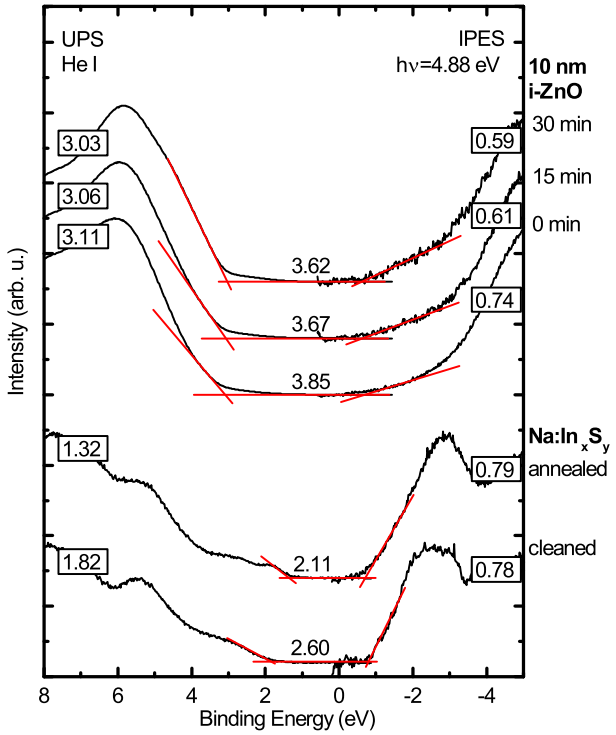

Figure 6.34: He I (left) as well as IPES (right) spectra of the cleaned and annealed Na:In_xS_y and i-ZnO samples. The i-ZnO samples were cleaned in 15 min steps with an Ar^+ treatment (50 eV, $\approx$ 80 nA/cm^2). For the 10 nm i-ZnO sample a surface band gap of 3.62 eV is determined. The determined VBM, CBM, and surface band gaps are given in eV.

207], but fits to the surface band gap of Ref. [190]. A slight overestimation of the band gap might originate due to the foot at about $E_{Bind} \approx (3-1)$ eV of the valence band maximum which can be related to defect states as well as to real states [190]. ZnO grows in crystallites which are not randomly distributed but have a preferred hexagonal orientation [208]. Hence, the photoemission signal is not k-integrated anymore and a possible lack of final states at the Γ-point can occur which might lead to a larger band gap derived from the data. For further study, experiments with different photon energies should be conducted in order to find a direct transition from the Γ-point (for details see e.g., Refs. [58, 60]).

A comparison of the CBM values of the cleaned Na:In_xS_y and 10 nm i-ZnO samples yields 0.78 eV and 0.59 eV, respectively. This points towards a clear cliff-like conduction band offset. In a further step, these CBM values have to be corrected for the interface induced band bending. For this purpose, three thin samples with 1 nm, 3 nm, and 5 nm i-ZnO thickness were used to follow the relative shift of the buffer core levels (i.e., S 2p and In 3d) and the window core levels (i.e, Zn 2p, Zn 3p, and the ZnO component of the O 1s). The

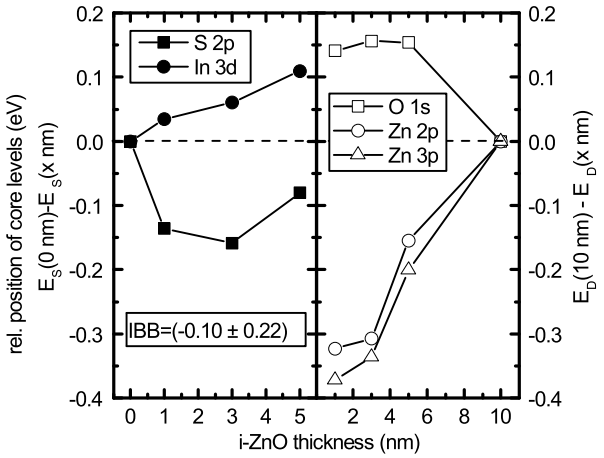

Figure 6.35: Relative shifts of the buffer- and window-related core levels for the determination of the IBB of the i-ZnO/Na:In_xS_y interface.

corresponding shifts are shown in Fig. 6.35. Here, a contrary behavior of the core levels can be monitored. In fact, while the S 2p shows a positive shift the In 3d shift is negative for the absorber site. For the window layer, the O 1s signal displays a positive shift and the Zn-related core levels a negative one. This opposite characteristic is reflected in the very large error bar of the IBB of (0.10 ± 0.22) eV. It is likely that the core levels undergo (in some cases strong) chemical shifts due to the formation of e.g., ZnS, $(SO)_4^{-2}$, and InO_x which superimposes the true interface induced band bending. Hence, the assumption of an abrupt non-intermixing interface cannot be used for the i-ZnO/Na:In_xS_y interface. Correspondingly, the determined IBB is neglected by approximation. In consequence, only the CBM values of the Na:In_xS_y and 10 nm i-ZnO samples are used for the following discussion. For the non-annealed interface a negative conduction band offset of (-0.19 ± 0.14) eV and a VBO of (-1.21 ± 0.07) eV is measured. For a comprehensive picture of the band alignment at the i-ZnO/Na:In_xS_y interface the intermixing process has to be taken into account. The formation of ZnS in the vicinity of the interface could lead to an increase of the conduction band minimum as follows. The optical bulk band gap of ZnS is $E_{Gap,ZnS} = (3.6 \pm 0.1)$ eV [196, 209, 210]. In comparison with ZnO, the VBM of ZnS is reported to shift up to 0.9 eV towards E_F and hence the CBM is shifted away from E_F by a similar amount [211]. This might reduce the cliff-like CBO or even transform it into a spike-like alignment. In consequence, the bands are smearing out in the interface region, possibly leading to a different band alignment. Since the annealing step does not significantly alter the CBM of the Na:In_xS_y buffer, a conduction band offset at the i-ZnO/Na:In_xS_y interface of CBO $= (-0.20 \pm 0.14)$ eV is measured after annealing while for the VB the offset is significantly increased to VBO $= (-1.71 \pm 0.14)$ eV. In addition to the change of the CBM

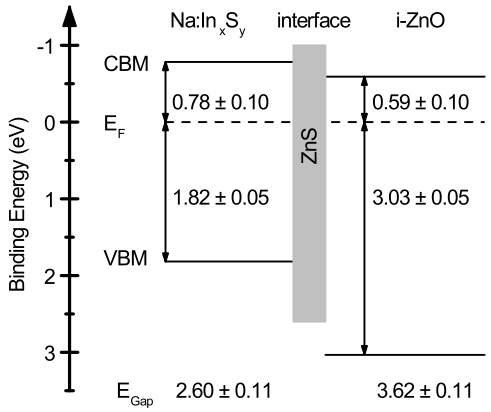

Figure 6.36: Schematic band diagram of the i-ZnO/Na:In_xS_y interface. The gray area indicates possible band positions of ZnS which is formed in the interface-near region. In consequence, the usually occurring cliff at the i-ZnO/Na:InxSy interface is reduced.

and VBM, the influence of the copper diffusion upon annealing has to be discussed. In Refs. [163, 192] it is stated that the annealing alters the ZnO/In_xS_y interface which results in a better performance of the solar cell. Since the copper enrichment at i-ZnO/Na:In_xS_y interface is reported to mainly affect the valence band [155], the only indication for an alteration of the interface found in this study is the formation of ZnS. One should note that this formation is related to the sputter process and not to the annealing step at 200 °C.

In summary, it was shown that the impact of the i-ZnO deposition induces the formation of ZnS in the i-ZnO/Na:In_xS_y interface-near region. A thermal treatment of the i-ZnO/Na:In_xS_y samples induces the copper diffusion from the absorber into the buffer layer capped with a window layer. Subsequently, the window layer was wet-chemical removed in order to get insight into the buried interface. The results indicate that the copper diffusion stops at the window/buffer interface. This verifies the approach of separately investigating the interfaces in CISSe solar cells. The occurring chemical intermixing at the interface implies that the band alignment between i-ZnO and Na:In_xS_y is more complex than the ideal abrupt interface suggests. Indeed, the formation of ZnS reduces the arising cliff-like CBO of about -0.2 eV, or forms even a small spike-like CBO in the interface-near region. Hence, the bands are smeared-out in the vicinity of the interface which leads to a band alignment that possibly improves the solar cell performance. These results suggest that the i-ZnO window layer plays an important role in the CISSe solar cell with indium sulfide buffers. For a further optimization of the i-ZnO/Na:In_xS_y interface, the impact of the sputter deposition on the chemical structure (and therefore on the electronic structure) has to be taken into account.

7

Electron energy loss spectroscopy of In_xS_y/CISSe samples

In the previous chapters, the main focus was set on the different surfaces and interfaces appearing in chalcopyrite-based solar cells. The electronic structure, especially at the buffer/ absorber interface is a crucial parameter for the performance of a solar cell. For example, an unusual large absorber surface band gap in comparison with optical bulk absorption of about 1.4 eV was revealed with the combination of UPS/IPES which was the only technique used to directly measure the surface band gap in thin-film solar cells directly to date.

In the following chapter, a complementary technique to the latter is used, namely reflective electron energy loss spectroscopy (REELS) which unveils electronic and optical properties of a sample by investigating the low-energy electron-loss region of a REELS spectrum. This region contains information of the characteristic excitations of a sample, e.g., the (excitonic) band gap, band transitions, and plasmon excitations, which are specified by the dielectric function $\varepsilon(\omega)$. With a tunable electron source the surface sensitivity can be tuned in the nanometer region which will be discussed in section 7.2. This calls for a utilization of the REELS technique for thin-film solar cells. For a CISSe absorber, an In_xS_y buffer, and an annealed In_xS_y buffer (both investigated buffers have a nominal indium content of $x = 42\,\%$) surface electronic and optical properties are gathered and compared with results from bulk optical spectroscopies.

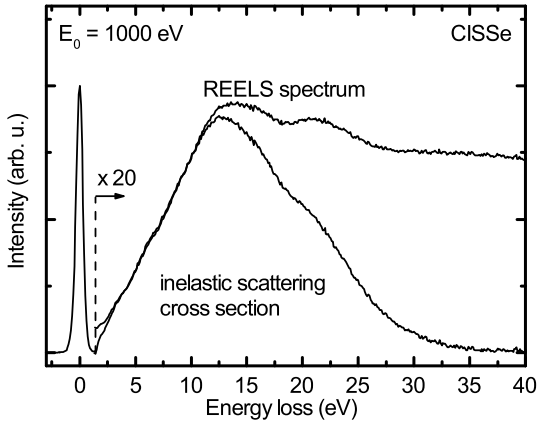

Figure 7.1: REELS spectrum and the derived inelastic scattering cross section $\lambda K(E)$ of a cleaned CISSe absorber ($E_0 = 1000\,\text{eV}$). The inelastic region is magnified by a factor of 20.

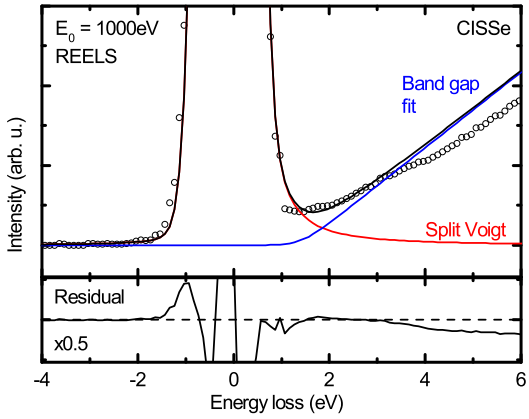

Figure 7.2: Fit of the onset of the CISSe REELS spectrum from Fig. 7.1 with a split Voigt (red) and the band gap fit function (blue). An absorber surface band gap of $(1.4 \pm 0.2)\,\text{eV}$ is determined. The bottom spectrum shows the residual, scaled with a factor of 0.5.

7.1 Optical properties of surfaces

A typical REELS spectrum of a CISSe absorber measured with a primary energy of $E_0 = 1000\,\text{eV}$ is shown in Fig. 7.1. The spectrum can be separated into two regions. The first one at about zero loss energy is dominated by the elastic peak (Rayleigh line) which is caused by elastically scattered electrons. The second region at higher loss energies appears as low-intensity structure which is caused by the inelastically scattered electrons. In order to highlight this structure, the second region is magnified by a factor of 20 in Fig. 7.1. This region starts at the excitonic band gap and contains characteristic single scattering excitations as well as multiple scattering electrons. For a further evaluation of the REELS spectrum, the multiple scattering electronic losses have to be removed (see section 2.2). The remaining single scattering losses are also shown in Fig. 7.1 and for the sake of clarity it is enlarged in order to fit the magnitude of the multiple scattering losses. As expected, for low loss energies the single scattering events dominate, while for energies larger than $\approx 35\,\text{eV}$ the multiple scattering electrons dominate the spectrum.

For a further data evaluation, the elastic peak has to be subtracted from the REELS spectrum. In literature it is stated that the accurate removal of the Rayleigh line is crucial [212]. Ac-

cordingly, different approaches can be found in literature, e.g., subtraction of a power law, subtraction of a mirrored Rayleigh line, subtraction of a fitted logarithmic tail, deconvolution of the elastic peak, or fitting Voigt profiles [212–215]. However, most of the approaches are used for a transmission EELS setup, where the kinetic energies (typically 200 keV) and also the FWHM of the Rayleigh line is larger. In the following, a split Voigt profile is used to account for the asymmetric line shape of the Rayleigh line. This is due to phonon losses which occur in the energy region of the elastically scattered electrons favored due to a non-uniform thermal distribution of the electrons. The thus determined FWHM of the Rayleigh line is (840 ± 30) meV. In a subsequent step, the excitonic band gap is determined. In literature, the intersection of a constant with the onset of the inelastically scattered electrons is often used for the determination of the band gap in REELS experiments [216, 217]. This procedure, however, neglects the tail of the Rayleigh peak and can only be used for large band gap materials (i.e., $E_{Gap} \geq 3\,\text{eV}$), where the influence of the tail can be neglected [216]. In contrast, for small band gap materials as used in this thesis, the Rayleigh tail has to be taken into account. Correspondingly, a linear fit towards the inelastically scattered onset should be conducted after subtracting the Rayleigh line. However, such a fit does not yet account for the experimental broadening. For this purpose, a fit function is employed which corresponds to a convolution of a linear function with a Gaussian distribution. The derivation of this fit function is shown in the appendix A.1. The fit of the onset of the inelastic region is shown exemplarily in Fig. 7.2 for the absorber surface which was excited with $E_0 = 1000\,\text{eV}$. The broadening σ was set to fit the FWHM of the elastic peak. The main focus of the fit lies on the loss energy region between $1-4$ eV since the band gap is expected to be in this energy region. However, depending on the fit region, different band gaps can be identified determining the error bar which is about 0.2 eV. As shown in the residual in Fig. 7.2 a good fit can be achieved for loss energies $\leq 4\,\text{eV}$ leading to an excitonic band gap of $E^{Ex}_{Gap,CISSe} = (1.4 \pm 0.2)\,\text{eV}$. This result is in excellent agreement with earlier performed UPS/IPES measurements of the surface band gap of a Cu(In,Ga)(S,Se)$_2$ absorber [8, 9] and the UPS/IPES measurements of $E^{Surf}_{Gap,CISSe} = (1.45 \pm 0.11)\,\text{eV}$ of the same sample in section 6.1.2. This shows the necessity of using surface-related values, e.g., for determining the band offsets at a buffer/CIGSSe interface. The fact that the optical properties of the CISSe surface and CISSe bulk differ significantly will also be shown later in this chapter.

After conducting the subtraction of the Rayleigh line from the REELS spectrum, the inelastic scattering cross section $\lambda K(E)$ is computed with the help of the recursive equation 2.14. It has to be noted that the inelastic scattering cross section is area normalized in order to fulfill the Kramers-Kronig sum rule [29, 30, 32]. The determined inelastic scattering cross section of the CISSe, In_xS_y, and annealed In_xS_y for a primary energy of $E_0 = 1000\,\text{eV}$ are shown in Fig. 7.3 a)-c), respectively. In general, the shapes of the three $\lambda K(E)$ are similar

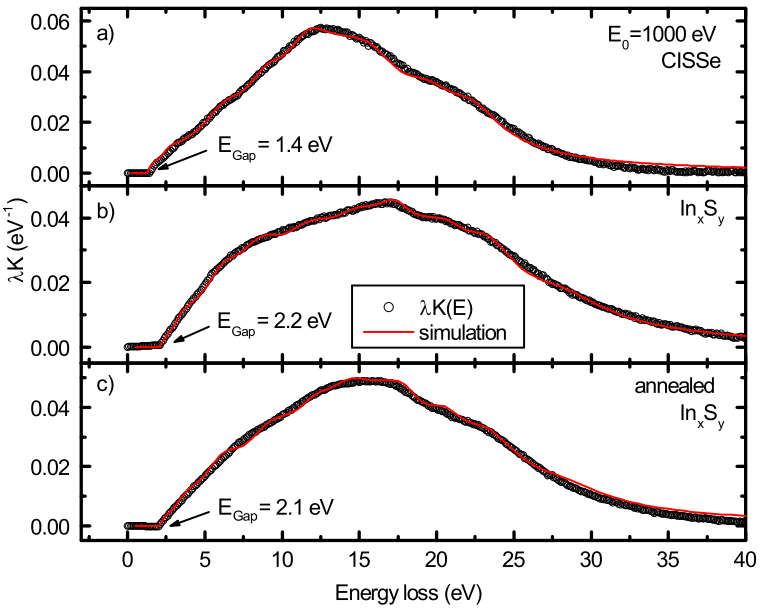

Figure 7.3: Inelastic scattering cross section $\lambda K(E)$ of a) CISSe, b) In_xS_y, and c) annealed In_xS_y. The simulated $\lambda K(E)$ spectra are shown in red. For each spectrum the surface band gaps are denoted.

to each other. However, the maximum for the CISSe sample is at about 12.4 eV, the In_xS_y maximum is at about 17.5 eV, and the maximum for the annealed In_xS_y is at 15.3 eV. Furthermore, the CISSe $\lambda K(E)$ has the highest intensity followed by the annealed In_xS_y and the In_xS_y sample. In the graphs the determined band gaps of the In_xS_y (2.2 eV) and the annealed In_xS_y (2.1 eV) samples are depicted, too. Table 7.1 compares them to the ones determined by the surface-sensitive UPS/IPES techniques. It turns out that the differently detected surface band gaps are within the error bar in good agreement with each other, especially concerning the trend of a decreased band gap upon annealing.

Table 7.1: Comparison of the determined EELS and UPS/IPES surface band gaps of CISSe, In_xS_y and annealed In_xS_y.

sample	EELS (eV)	UPS/IPES (eV)
CISSe	1.4 ± 0.2	1.45 ± 0.11
In_xS_y (x = 42 %)	2.2 ± 0.2	2.34 ± 0.11
annealed In_xS_y (x = 42 %)	2.1 ± 0.2	1.95 ± 0.11

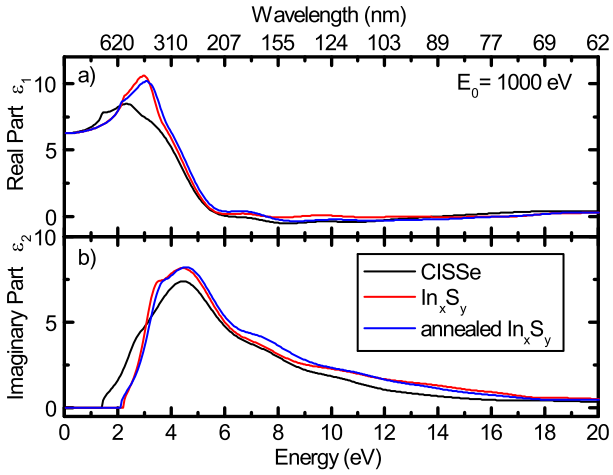

Figure 7.4: Real part ε_1 a) and imaginary part ε_2 b) of the dielectric function of the CISSe absorber (black), In_xS_y (red), and annealed In_xS_y (blue).

The inelastic scattering cross section $\lambda K(E)$ is closely related to the electronic loss function (ELF) $\mathrm{Im}\left[-\frac{1}{\varepsilon(\hbar\omega)}\right]$ [218–220] and thus to the complex dielectric function $\varepsilon(\hbar\omega)$. To further analyze the $\lambda K(E)$ spectra, the QUEELS-$\varepsilon(k,\omega)$ [220] software package was used to simulate the inelastic scattering cross section $\lambda K(E)$ of the CISSe, In_xS_y, and annealed In_xS_y with a sum of Drude-Lindhard oscillators (see section 2.2). For all samples a dispersion coefficient $\alpha_i = 0.5$ is used, since this value is typical used for low band-gap materials [221, 222]. The corresponding parameters for the oscillators are derived via a trial-and-error procedure until a good agreement between the experimental and the simulated inelastic scattering cross section $\lambda K(E)$ is found. The best-fit models of $\lambda K(E)$ are plotted as a red line in Figs. 7.3 a)-c). The parameter sets for the CISSe absorber, the In_xS_y buffer, and the annealed In_xS_y buffer are listed in appendix A.1 for three different primary energies $E_0 = 1000\,\mathrm{eV}$, 500 eV, and 200 eV, respectively. The best-fit oscillator models were used to determine the complex dielectric function $\varepsilon(\hbar\omega) = \varepsilon_1 + \mathrm{i}\varepsilon_2$ with the help of the Kramers-Kronig sum rule [29, 32]. For all samples, the boundary condition $n_0(\hbar\omega \to 0) = 2.5$ is used in the optical limit. The optical limit value for the CISSe absorber was taken from Ref. [173], while for the In_xS_y buffer an ellipsometry measurement was exploited. The ellipsometry measurement was performed by S. Pohlner using an SENTECH SE850 ellipsometer and a Xe arc lamp as light source. For the annealed In_xS_y buffer it was expected that n_0 is not changing significantly and thus the same value as for the In_xS_y buffer was used.

Fig. 7.4 a) and b) illustrate the calculated real $\varepsilon_1(\hbar\omega)$ and imaginary part $\varepsilon_2(\hbar\omega)$ of the dielectric function, respectively. At first glance, the In_xS_y and annealed In_xS_y spectra are similar, whereas the CISSe spectrum differs significantly, especially in the energy region

$E < 6\,\mathrm{eV}$. The real part $\varepsilon_1(\hbar\omega)$ starts for all samples at $\varepsilon_1(0) = 6.3$ which is related to the boundary conditions. The real part $\varepsilon_1(\hbar\omega)$ of CISSe rises for increasing energies and has three distinct maxima at 1.5 eV, 2.3 eV, and 3.5 eV. The most intensive maximum at 2.3 eV has a value of 8.5. The indium sulfide samples also show three maxima, but less prominent. The dominant feature is shifted by about 0.7 eV towards higher energies (In_xS_y 3 eV, annealed In_xS_y 3.1 eV). For further increasing energies all $\varepsilon_1(\hbar\omega)$ decrease significantly towards zero and the three spectra merge into each other. In spite of that, the CISSe spectrum has two zero-crossings, the first one at 6.3 eV and the second one at 13.9 eV. The second zero-crossing can be assigned to a bulk-plasmon. The requirements for such a plasmon are $\varepsilon_1(\hbar\omega) = 0$ and that $\varepsilon_2(\hbar\omega)$ does not have a maximum, whereas the ELF needs a maximum [28]. For the In_xS_y sample no zero-crossing is observed, whereas for the annealed In_xS_y sample two zero-crossings occur at 7.6 eV and at 16.2 eV. Analogue to CISSe, the annealed In_xS_y also show a plasmon at 16.2 eV. These findings suggest that the main parameter for the appearance of a plasmon in these compounds is copper, since copper diffuses into the indium sulfide upon annealing, which was shown in section 6.1.1. The imaginary part $\varepsilon_2(\hbar\omega)$ of the three samples starts at the corresponding band gap energy and rises continuously to a common maximum. The imaginary part ε_2 of the CISSe absorber further peaks at about 4.3 eV with a maximum value of 7.3. The indium sulfides maxima are shifted by about 0.3 eV to 4.6 eV with a maximum value of ≈ 8.2. For higher energies all $\varepsilon_2(\hbar\omega)$ curves decrease towards zero. For energies higher than 15 eV, the spectra decrease further towards zero while $\varepsilon_1(\hbar\omega)$ increases in parallel. This is accompanied by a higher transmission in this energy region [223].

From the dielectric function, the refraction index n, the extinction coefficient κ, and the absorption coefficient α were calculated and are plotted in Fig. 7.5 a), b), and c), respectively. The refraction index n exhibits a similar shape for all three samples. At high wavelengths (low energies), n is almost constant with a slightly increasing slope for decreasing wavelengths (normal dispersion; $\left\{\frac{\mathrm{d}n}{\mathrm{d}\lambda} < 0\right\}$). For CISSe the dispersion is anomalous below 500 nm. The maximum of n for the In_xS_y buffer layer sample is located at about 400 nm and for the annealed In_xS_y buffer the maximum is slightly shifted by 20 nm to lower wavelengths. For smaller wavelengths all indium sulfides show a decreasing refractive index. In Fig. 7.5, also a bulk ellipsometry measurement of the In_xS_y buffer is displayed for comparison as a green dashed line. The two differently determined refractive index spectra of In_xS_y are in good accordance with each other. The maximum of n is also at 400 nm, but the height is $\approx 5\,\%$ less. Only for energies above 3.5 eV the spectra differ slightly.

The extinction coefficients κ (Fig. 7.5 b) start for each spectrum at the corresponding band gap energy (as it is expected from the dielectric function $\varepsilon_2(\hbar\omega)$), increase to a maximum

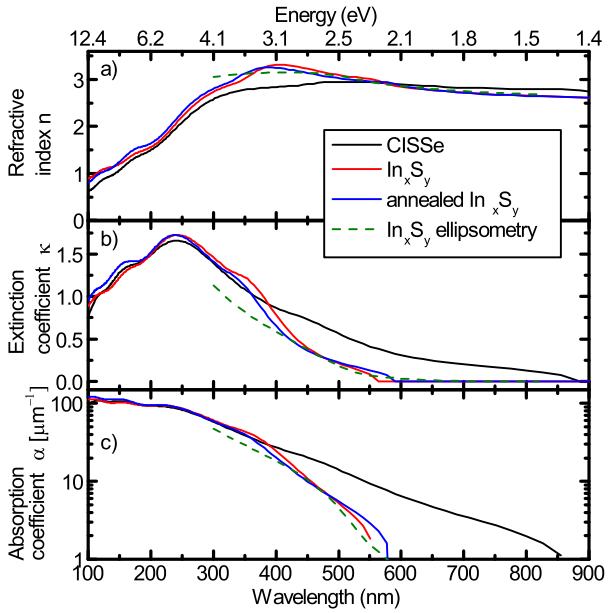

Figure 7.5: Optical values of CISSe (black), In_xS_y (red), and annealed In_xS_y (blue) as well as a (bulk-sensitive) optical measurement of In_xS_y (dashed green). a) Refractive index n, b) extinction coefficient κ, and c) absorption coefficient α as calculated from the dielectric function shown in Fig. 7.4.

at about (240 ± 10) nm and decrease for higher energies. However, the trend of the spectra is different. The CISSe extinction coefficient is higher than for the other samples for $\lambda > 400$ nm and κ of In_xS_y between $320 - 450$ nm is higher than the annealed In_xS_y. The annealing step might induce segregation of stronger absorbing phases in non-stoichiometric films or reduce intergranular defects due to an increase of the grain size [224, 225] which might explain the higher extinction coefficient in this region. The ellipsometry (green) and the REELS In_xS_y buffer (red) measurements have the same onset and a similar behavior for $\lambda < 400$ nm. This proves the linear extrapolation of the inelastic scattering region of the REELS experiment for the determination of the surface band gaps. However, the optically determined κ of In_xS_y deviates for $\lambda < 400$ nm in comparison with the REELS one. This points towards different compositions of the surface and the bulk, i.e., an indium sulfide phase with a better absorption probability at the surface (e.g., In_6S_7 with a band gap below 1 eV [115, 116]), which supports the XPS finding of an indium-rich surface composition. In general, the very good agreement between the REELS and ellipsometry measurements proofs the validity of the surface dielectric function determined with REELS.

Regarding the absorption coefficient α in Fig. 7.5 c), two different trends can be observed for wavelengths $\lambda > 350$ nm: the CISSe absorber exhibits a higher absorption coefficient

for wavelengths above 400 nm, which is desired for absorbing light. The indium sulfides show the same trend, but for about 400 nm the In_xS_y has a higher absorption coefficient than the annealed one which was already explained in terms of the extinction coefficient κ. For high energies the three spectra converge and α is about 100 μm^{-1}, determined by various interband transitions. The α value of CISSe is similar to reported bulk absorption values [173, 224]. An assignment of characteristic features in the optical properties to specific transitions in the band structure in the case of the CISSe absorber will be discussed in the following section.

In conclusion, the surface-related dielectric function and the corresponding optical properties of a CISSe absorber, an In_xS_y buffer layer, and an annealed In_xS_y buffer were investigated with the help of reflective electron energy loss spectroscopy. A good agreement between the surface-related and bulk-related optical values of In_xS_y is achieved. Furthermore, the excitonic surface band gaps were determined, leading for indium sulfide to similar band gaps as bulk literature references as well as optical determined values. For the CISSe absorber, the here identified surface band gap of (1.4 ± 0.2) eV confirms earlier findings that the surface band gap exceeds by far the bulk band gap. This highlights the importance of surface band gaps when band alignments between absorber and buffer are investigated.

7.2 Tuning the surface sensitivity

A further outstanding opportunity of REELS is the tunable surface sensitivity by using different primary electron energies. This allows to obtain a "depth-resolved" picture of the optical properties. For this purpose the CISSe, In_xS_y, and annealed In_xS_y were measured with primary electron energies of 200 eV, 500 eV, and 1000 eV (the latter energy spectra were shown in the previous section). These energies are in particular interesting since they are usually used in the photoelectron spectroscopy. With the primary electron energies used in this experiment, an inelastic mean free path (IMFP) λ of $\approx 20\,\AA$ and $\approx 7-10\,\AA$ for 1000 eV and 200 eV, respectively, is covered and thus the surface sensitivity can be varied by a factor of two. As it was shown in the previous section, the surface optical properties of the In_xS_y layer mainly fit the bulk one, while significant differences appear for the CISSe sample. Hence, the CISSe absorber sample is a promising candidate to investigate the depth-resolved optical properties since strong stoichiometric gradients appear at the surface.

For this purpose the three REELS spectra excited with different primary energies ($E_0 =$ 200 eV, 500 eV, and 1000 eV) are shown together with the inelastic scattering cross section λK(E) in Fig. 7.6. The first observation is a higher background for decreasing primary electron energies especially in the case of the 200 eV spectrum. The reason for that is a continuum of secondary electrons scattered multiple times which depends on the different primary energies [226]. The latter fact might explain the high background for the 200 eV spectrum and also why the 200 eV band gap extracted from the data is too small (≈ 0.6 eV), for both, the surface and the bulk band gap value. In general, values extracted from the REELS spectrum excited with 200 eV are not reliable and hence the data are shown but not discussed in the following. Besides the too small 200 eV surface band gap, the $E_0 = 500$ eV surface band gap value is in accordance with the $E_0 = 1000$ eV measured (excitonic) surface band gap of $E^{Ex}_{Gap,CISSe} = (1.4 \pm 0.2)$ eV.

The subtraction of the elastic peak and the removal of the multiple scattered electrons were performed according to section 7.1 resulting in the inelastic scattering cross sections $\lambda K(E)$ which are shown in Figs. 7.6 a)-c) for 1000 eV, 500 eV, and 200 eV, respectively. For decreasing primary electron energies the shape of $\lambda K(E)$ gets broader, i.e., from 30 eV for $E_0 = 1000$ eV to about 50 eV for $E_0 = 200$ eV. Correspondingly, the maximum intensity decreases due to the area normalization.

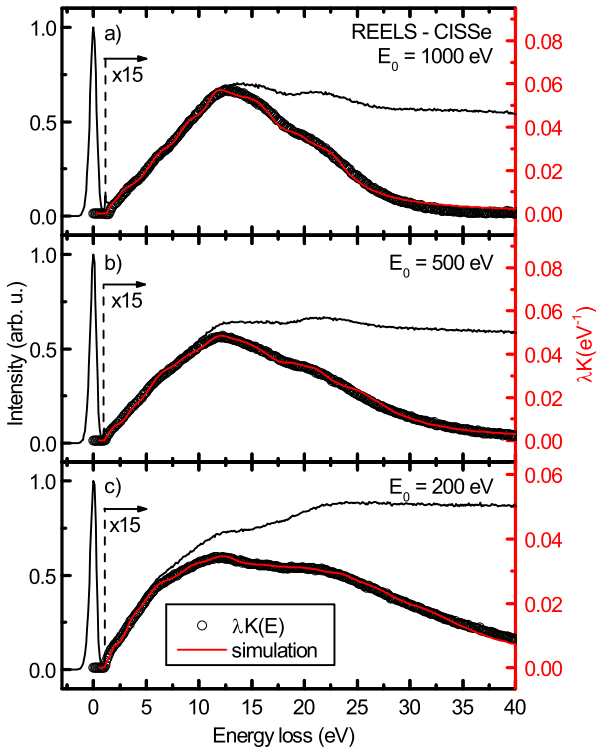

Figure 7.6: REELS spectra and the derived inelastic scattering cross section $\lambda K(E)$ of the CISSe absorber for three different primary electron energies a) $E_0 = 1000\,\text{eV}$, b) $E_0 = 500\,\text{eV}$, and c) $E_0 = 200\,\text{eV}$. The simulated $\lambda K(E)$ spectra are shown as a red line (right axis). For each spectrum the simulated surface band gaps were set to 1.4 eV (see text).

The three $\lambda K(E)$ spectra are simulated with a sum of Drude-Lindhard oscillators. For all samples a dispersion coefficient of $\alpha_i = 0.5$ is used. Despite the fact that the determined band gap for a primary energy of 200 eV is too small, for the simulation of $\lambda K(E)$ the value of the band gaps were set to 1.4 eV for all three primary energies. With a trial-and-error procedure a parameter set was found which reproduces the measured $\lambda K(E)$ well. The identified best-fit models for $\lambda K(E)$ are shown in Figs. 7.6 a)-c) as a red line and the corresponding parameters are listed in appendix A.1. On the basis of these Drude-Lindhard oscillators, the real and imaginary part of the dielectric function ε are calculated and plotted in Fig. 7.7. For comparison, literature values of the normal incidence dielectric function of stoichiometric (001)-oriented $CuInS_2$ (CIS) and (112)-oriented $CuInSe_2$ (CISe) single-crystals [227] measured by ellipsometry are also plotted as a green and purple dashed line. It should be noted that the CISSe surface investigated here has different properties in comparison with the stoichiometric CIS and CISe single-crystals. In particular, the CISSe surface is copper poor and comprises unique electronic properties, e.g., the larger surface

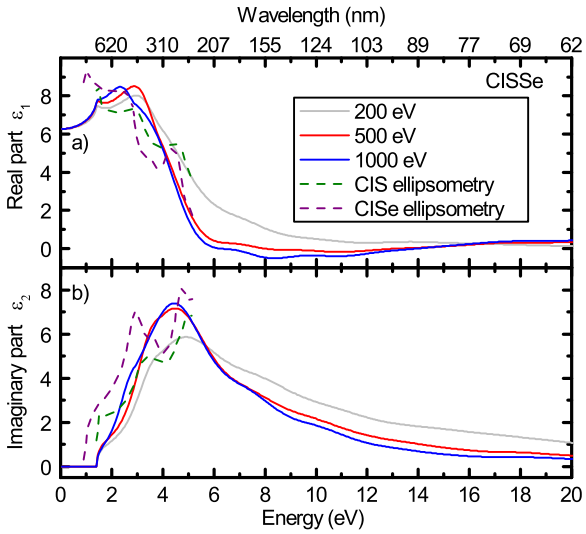

Figure 7.7: a) Real part ε_1 and b) imaginary part ε_2 of the dielectric function of the CISSe absorber for three different primary electron energies $E_0 = 1000\,\text{eV}$ (black), 500 eV (red), and 200 eV (gray). For a comparison, the dielectric functions of $CuInS_2$ (CIS) and $CuInSe_2$ (CISe) single-crystals (normal incidence) are plotted as a green and purple dashed line, respectively. The single-crystal data are taken from Ref. [227].

band gap. However, the different measured data will be compared in the following although the comparison is probably limited.

The real part ε_1 of the CISSe absorber exhibits a prominent maximum which is shifting from 2.9 eV for 500 eV by about 0.5 eV to 2.4 eV for 1000 eV primary electron energy. A comparison with bulk literature values exhibits a similar shift of this prominent feature from 2.8 eV to 2.3 eV for a CIS to a CISe environment, respectively. Thus, the evaluation of this peak position can be used as a measure for the S/Se ratio of the sample [6]. One may speculate that the different measurements probe a different S/Se ratio leading to shifts of this feature although no S/Se-related gradients are expected for the different probing depths. For energies $E \geq 3.5\,\text{eV}$ the EELS measured ε_1 decreases, while the literature values exhibit a local minimum at about 3.8 eV with a subsequent local maximum. For higher energies both, the CIS and the CISe dielectric function decrease significantly. For even higher energies ($E \geq 5\,\text{eV}$) no optical measurements were available and thus only the REELS measurements can be discussed. A second zero-crossing is observed at 13.1 eV ($E_0 = 500\,\text{eV}$) and 13.9 eV ($E_0 = 1000\,\text{eV}$). These zero-crossings can be assigned to a plasmon since the $\varepsilon_2(\hbar\omega)$ have not a maximum and the respective ELFs $\text{Im}\left[-\frac{1}{\varepsilon(\hbar\omega)}\right]$ have a maximum at the respective energies [28].

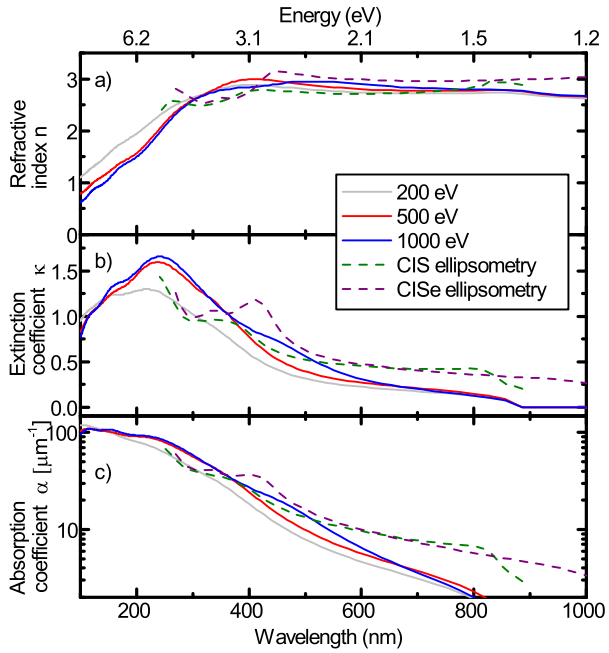

Figure 7.8: Optical values of the CISSe absorber for $E_0 = 200\,\text{eV}$ (gray), 500 eV (red), and 1000 eV (blue) primary electron energies. Bulk sensitive measurements of a CIS and CISe single-crystals [227] are shown as a dashed green and purple line, respectively. a) Refractive index n, b) extinction coefficient κ, and c) absorption coefficient α.

The imaginary part ε_2 of the CISSe spectra exhibits a prominent maximum at 4.5 eV for 500 eV and 1000 eV primary electron energy. Furthermore, at $2-3\,\text{eV}$ ε_2 has a higher intensity for $E_0 = 1000\,\text{eV}$ than for $E_0 = 500\,\text{eV}$. A comparison with the single crystal spectra illustrates that a similar intensity increase is associated with the increasing selenium content.

The refractive index n, the extinction coefficient κ, and the absorption coefficient α are computed with the help of the dielectric functions and are displayed in Figs. 7.8 a)-c), respectively. For energies in the region of the band gap the values of n and κ differ which can be related to the different surface properties, i.e., the larger surface band gap. The refractive index n is very similar for the investigated primary electron energies. Merely the position from normal to anomalous dispersion is shifted to higher wavelengths for increasing probing depth, i.e., from 400 nm to about 500 nm. While the dispersion of the CIS single-crystal changes at about 400 nm, the dispersion of the CISe changes at about 470 nm. In addition, both literature spectra (CIS and CISe) exhibit a local minimum in the refractive index n at about 300 nm which is not observable for the REELS measurement.

The extinction coefficient κ spectrum at a primary energy of 1000 eV displays a shoulder between 600 nm and 400 nm, which is not observed in the 500 eV spectrum. The comparison with the bulk data of CIS and CISe suggests that the shoulder is a Se-related feature, since the peak at about 400 nm is shifting to higher wavelengths from CIS to CISe. The higher extinction coefficient κ in the region above 450 nm can be attributed to the much smaller bulk band gap. For wavelengths $\lambda < 250$ nm, κ is decreasing for all primary electron energies.

For all measurements, the absorption coefficient α starts at the value of the surface band gap, rises continuously for smaller wavelengths and reaches $100\,\mu m^{-1}$ at about 200 nm. This general trend is also observed for the CIS and CISe single-crystals. However, these spectra already start at higher wavelengths (according to the respective band gaps) and a significant higher absorption coefficient α is noticeable in the low energy regime. The reason for this is probably a higher number of possible transitions in the band structure in this energy regime in comparison with the CISSe surface.

Spectral features which are observed in the dielectric function $\varepsilon(\hbar\omega)$ (and correspondingly n and κ) are closely linked to interband transitions which are related to the electronic band structure [228]. In order to investigate the characteristic interband transitions, the reflectivity of the samples is used and compared with literature values [227, 229]. The reflectivity R of a sample is calculated as [172]:

$$R = \frac{(n-1)^2 + \kappa^2}{(n+1)^2 + \kappa^2} \,. \tag{7.1}$$

The reflectivity of the CISSe sample (for the different primary energies) as well as characteristic transition energies for CIS and CISe single-crystals are shown in Fig. 7.9. The reflectivity spectra of the CISSe absorber are in reasonable agreement with published results [173, 174, 227, 229]. Only the local minimum at about 4 eV is not included in the REELS-determined CISSe reflectivity. Furthermore, labels assign features to interband transitions appearing in e.g., $CuInS_2$. In Fig. 7.10 the band diagram of a $CuInS_2$ single-crystal is shown together with the proposed transitions. This band structure calculation was performed by Levcenko *et al.* and neglects spin-orbit interactions [229]. The notation of the high-symmetry points have been chosen to be consistent with Refs. [72, 230]. The E_0 transition corresponds to the fundamental band gap from V_1 to C_1 at the Γ-point (see Fig. 7.10) and consists of three energetically close transitions [72, 227] (taking spin-orbit split into account). At higher energies, the reflection is mainly dominated by the strong $E_{1,2}$ features. According to Fig. 7.10, the appearance of the reflection peak $E_{1,2}$ can be assigned to an optical resonance at the Γ-point from V_1 to C_2. In contrast, Alonso *et al.* [227] assigned this to two transitions at the N-point which correspond in Fig. 7.10 to $V_1 \rightarrow C_1$ and

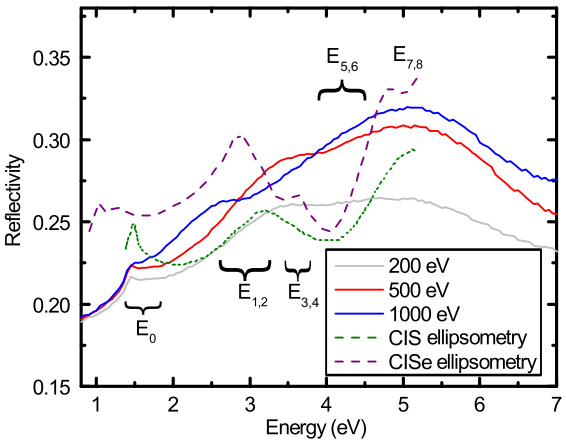

Figure 7.9: Reflectivity computed from the REELS data of the CISSe absorber for 200 eV (gray), 500 eV (red), and 1000 eV (blue) primary electron energies. Bulk sensitive ellipsometry measurements of CIS and CISe single-crystals [227] are shown as a dashed green and purple line, respectively. Characteristic transitions are marked according to Fig. 7.10.

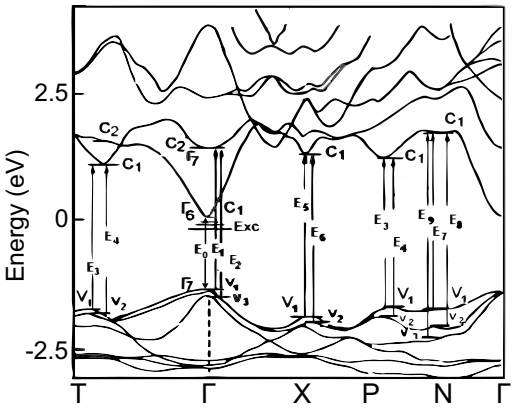

Figure 7.10: Calculated band structure of a $CuInS_2$ single-crystal. Notations of the transitions are depicted. Graph adapted from Ref. [229].

$V_2 \rightarrow C_1$. However, independent from the assignment of the transition, the peak position varies with the S/Se ratio, clearly visible when comparing the CIS and CISe reflection spectra. Thus, the $E_{1,2}$ peak position can be used as a measure for the S/Se ratio [6]. The peaks $E_{3,4}$ are only pronounced for the CISe spectrum and are alternatively attributed to transitions at the P-point ($V_1 \rightarrow C_1$ and $V_2 \rightarrow C_1$) or at the T-point according to Fig. 7.10. In Ref. [227] these peaks are attributed to a transition at the N-point. According to the band structure, two features occur at $\approx$ 4.5 eV which are caused by a transition at the X-point ($E_{5,6}$). However, these features are not present in the single-crystal data, while the REELS measurements show a broad intensity in this energy region. At 5 eV the reflectivity peaks in a distinct maximum which consists of two transitions $E_{7,8}$ and are probably caused by the transition $V_2 \rightarrow C_1$ at the N-point or $V_2 \rightarrow C_1$ at the Γ-point. The transition E_9 should appear at about 6 eV which was not measured in the ellipsometry measurements. In the REELS measurement this feature is possibly included in the main reflectivity peak at about 5 eV.

Although the qualitative agreement is reasonable, differences between the REELS and ellipsometry measurements are monitored which has probably several reasons. The REELS experiment has an energy resolution of about 0.8 eV and thus sharp features are smearing

out. In addition, only the first few layers of the sample are probed. Since CISSe surfaces are copper poor, the band structure in the vicinity of the surface is expected to be significantly different compared to a single-crystal and thus transitions are possibly shifted in energy or suppressed. Another important factor for the optical properties is the surface roughness of a sample. A smoother surface yields a higher reflectivity [231]. However, since the reflectivity of the REELS measured CISSe samples is in between the CIS and CISe spectrum, this effect is possibly negligible. In addition, the excitation of characteristic transitions with electrons tentatively lead to different transitions since the electron's momentum is much larger than that of the photon.

Determination of the IMFP from the REELS experiment

The REELS experiments provide the experimental inelastic scattering cross section $\lambda K(E)$. This can be used to determine the inelastic mean free path (IMFP) λ for the used primary electron energy E_0. The IMFP is defined as the inverse of the area below $K(E_0,\hbar\omega)$ [32]:

$$\frac{1}{\lambda(E_0)} = \left[\int_0^\infty \mathrm{d}E K_{th}(E_0,E)\right]. \tag{7.2}$$

Accordingly, the simulated theoretical $K_{th}(E_0,E)$ are used to determine the inelastic mean free path at the three primary energies $E_0 = 200\,\mathrm{eV}$, 500 eV, and 1000 eV. The determined values are plotted in Fig. 7.11. An error bar of $0.4\,\mathring{A}$ is estimated which is covered by the data point size. As a guide to the eye, the "universal curve" [232] is sketched and calculations performed with the TPP-2M code [160] are shown as dashed curves in Fig. 7.11. For the TPP-2M calculations, stoichiometric $CuIn(S,Se)_2$, In_2S_3, and $CuIn_5S_8$ were used. The TPP-2M values exceed the REELS ones for 200 eV and 500 eV. For a kinetic energy of 1000 eV the REELS and TPP-2M values are in good agreement with a deviation of less than 5 %. In addition, the results are well described by the "universal curve".

The reasons for the discrepancies between the REELS and the TPP-2M code, especially for $E_0 \leq 500\,\mathrm{eV}$, are discussed in the following. In the $\lambda K(E)$ model it is assumed that the electrons undergo only one scattering process. Especially for low kinetic energies the contribution of multiple times back-scattered electrons is probably not negligible which can be noticed in an increasing background in the measured REELS spectra [33]. Thus the area below $K_{th}(E_0,E)$ is overestimated which leads to too small IMFPs. A further source of errors are possible residual surface contaminations which mostly impact electrons with low kinetic energies. Furthermore, the non-stoichiometric surface composition of the investigated samples might lead to a systematic error in comparison with the ones used for the TPP-2M code. For the sake of completeness, the 200 eV values are shown in Fig. 7.11.

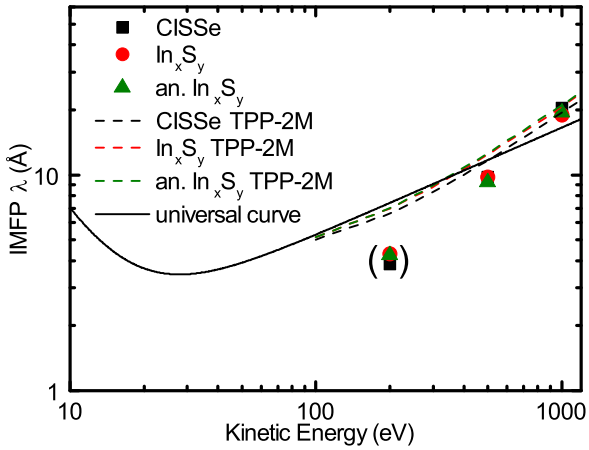

Figure 7.11: Inelastic mean free path (IMFP) for different kinetic energies for a CISSe absorber (black), an In_xS_y buffer layer (red), and an annealed In_xS_y buffer layer (green). The filled data points represent the REELS values, while the dashed curves are determined from the TPP-2M code [160]. The "universal curve" is plotted as a guide to the eye [232].

In conclusion, reflective electron energy loss spectroscopy experiments at different primary energies of 200 eV, 500 eV, and 1000 eV were performed and analyzed for a CISSe surface which is expected to show stoichiometric gradients. Hence, the $\lambda K(E)$ spectra were simulated for these different primary energies. The subsequent calculated dielectric function ε, refractive index n, extinction coefficient κ, and absorption coefficient α show differences for the varying primary energies. These spectra were compared with bulk-sensitive measurements of $CuInS_2$ and $CuInSe_2$ single-crystals which reveals a good qualitative agreement taking the different band gaps into account. The calculation of the reflection allows to analyze and assign features to characteristic transitions in the band structure with the help of literature spectra. Besides, the determined inelastic mean free path λ for 1000 eV is found to be in very good agreement with the values derived from the TPP-2M code from Tanuma *et al.* [160].

8

Concluding discussion and outlook

In the previous chapters, the chemical and electronic structure of surfaces and interfaces in indium sulfide-buffered Cu(In,Ga)(S,Se)$_2$-based thin-film solar cells were investigated. A dry PVD evaporation of this buffer layer promises an inline production of the complete device and thus upscaling to industrial requirements is expected to be relatively easy. Overall, three different interfaces (the In_xS_y/CISSe interface, the sodium doped Na:In_xS_y/CISSe interface, and the i-ZnO/Na:In_xS_y interface) were investigated using surface-sensitive photoemission spectroscopy (PES), inverse PES and surface-near bulk-sensitive x-ray emission spectroscopy (XES). The combination of these techniques allows comprehensive insights into the chemical and electronic structure of the surfaces and interfaces.
The three different interfaces were treated as model systems and the further cell processing, i.e., an elevated temperature step, was simulated in order to achieve a detailed knowledge about interdiffusion phenomena at the interfaces. In the following chapter, the obtained results are discussed and compared with literature. On the basis of the found results, suggestions for further improvements of chalcopyrite-based thin-film solar cells are made.

For a dry evaporation technique, the cleaning step of the chemical bath deposition [7] is absent which is expected to lead to different surface/interface properties. A systematic study of different environmental impacts on the absorber surface revealed a significant increase of adsorbates in dependence of humidity and storing temperature. In addition, changes of the absorber surface stoichiometry, in particular varying degrees of sulfur, copper, and sodium

concentrations were monitored. This diffusion of absorber elements possibly leads to an unfavorable chemical structure, e.g., copper enrichment at the surface which is possibly accompanied by a surface band gap decrease. In addition, oxidation of the absorber elements has to be considered which probably also leads to a variation of the electronic structure. Furthermore, independent from the storing conditions a creation of sodium carbonate (Na_2CO_3) was identified at the surface. Besides the reported beneficial effects of sodium on a solar cell [194], Na_2CO_3 may act as recombination center at the buffer/absorber interface which is expected to decrease all solar cell parameters [233]. In general, it is desirable that the buffer layer does not suffer from these surface modifications in order to deliberately control the properties of the absorber. Thus, the storage as well as the subsequent evaporation of a buffer layer should be performed in an humidity-free and oxygen-free environment. As the environmental conditions of other thin-film solar cell materials, e.g., kesterites (CZTSSe), lead to similar alterations of the surface [234], this experiment may serve as benchmark for further investigations on other materials.

Large efforts have been made to replace CdS as buffer material. A replacement of CdS with an indium sulfide-based material requires a detailed characterization of this buffer layer and the buffer/absorber interface. In the case of an In_xS_y buffer layer it was found that the crucial parameter for the performance of the full solar cell is the S/In ratio of the film with an optimum at an indium concentration of approximately 42 % [6]. The quantitative analysis shows only a small diffusion of copper from the absorber surface into the In_xS_y buffer upon deposition for an indium content of $40.2\% \leq x \leq 43.2\%$. Furthermore, the S/In ratio of the surface of all investigated In_xS_y layers is almost identical to that of In_6S_7 (i.e, S/In = 1.17). However, a coexistence of In_2S_3, In_6S_7, and InS might occur. These results indicate that the surface composition is largely independent of the nominal S/In ratio. The more bulk-sensitive XES measurements suggest the formation of an abrupt interface between absorber and buffer. This is in contrast to other publications [10, 70] which detected an intermixing upon indium sulfide deposition.
Moreover, an influence of the nominal bulk composition on the electronic properties of the In_xS_y surface is observed. For the nominal composition close to stoichiometric In_2S_3 ($x = 40.2\,\%$), a buffer band gap of (2.44 ± 0.14) eV is found, which slightly decreases for increasing indium content to about (2.34 ± 0.14) eV. One explanation is that the decreasing band gap is probably related to a lower fraction of sulfur since the valence band maximum is mainly composed by S p orbitals [155]. Furthermore, according to Gödecke *et al.* [118] a phase transition from the β- to α-phase occurs for indium contents larger than 40.5 % and the band gap decrease is probably related to this phase transition. Besides this, the band gap values are in good agreement with earlier reported optical ones [121, 175].
The conduction band (CB) alignment at the buffer/absorber interface strongly depends on

the nominal S/In ratio. While a significant spike is monitored for the stoichiometric In_xS_y, a small cliff is detected for x = 41 %. For further increasing In content, a flat alignment is observed for x = 42 %, while for x = 43.2 % a small spike appears in the CB. To further characterize the indium sulfide layer model systems, it is essential to study the impact of the thermal treatment from the subsequent processes which is reflected by an annealing step up to 200 °C. This treatment is needed for high efficient solar cells [10, 156, 163]. Here, a significant diffusion of copper is detected leading to a copper content of about (4.2 ± 2.0) % at the surface corresponding to Cu/In = (0.10 ± 0.05). Furthermore, an analysis of the XES S $L_{2,3}$ proposes a bulk Cu/In ratio of about 0.2, i.e., a formation close to $CuIn_5S_8$.

In general, the incorporation of copper into indium sulfide reduces its band gap leading to an unfavorable enhanced absorption of light in the buffer. The latter is accompanied with a reduction of the n-character of the indium sulfide layer which is in agreement with [121, 176]. However, for the stoichiometric sample (x = 40.2 %), the impact of the diffusion of absorber elements results in a negative CBO at the In_xS_y/CISSe interface due to an enhanced copper incorporation in the bulk [6]. For x$\geq$ 41 % which is indicative for a transition from the β- to α-phase [118] the conduction band alignments show a small spike in the conduction band offset ($\approx 0 - 0.1$ eV) which is in accordance with the high efficiencies.
Moreover, the copper diffusion suggests a copper depletion in the surface-near region of the $CuIn(S,Se)_2$ absorber surface. Since copper mainly affects the valence band [121], a wider band gap in the vicinity of the absorber surface is expected. Hence, the distance between the VBM and the Fermi level should increase, which comes along with a reduced recombination at the buffer/absorber interface [53]. Even though no direct observation of a copper depleted absorber surface is resolved with the methods applied in this thesis, this model is indeed supported by electric measurements [157, 235] of In_2S_3 which propose a reduction of the buffer/absorber interface recombination after annealing. Hence, the diffusion of copper leads on the one hand to a reduction of the buffer layer band gap but also reduces the recombination at the In_xS_y/CISSe interface. In addition, the almost flat band alignment at the latter interface can explain the S/In dependence on the solar cell efficiency.

The fact that almost all publications examine stoichiometric In_2S_3 might explain the reported significant efficiency improvements after annealing [150, 152, 156, 158, 163]. The In_2S_3/absorber interface reveals a significant spike in the conduction band alignment before annealing which is reduced after the annealing step. Different thermal treatments, e.g., a reduced annealing time, may lead to an almost flat alignment in the CBO which is favorable for the electron transport. In addition, the interface recombination is reduced due to a copper depleted absorber surface with a correspondingly larger band gap.

These results suggest that copper diffusion is an important parameter for high efficiencies when using indium sulfide buffer layers. Hence, a reduced copper diffusion would be favorable which is predicted for doping the In_xS_y buffer with sodium. Moreover, it is expected that doping the In_xS_y layer with sodium increases the indium sulfide band gap [122, 181]. Both hypothesis were confirmed by UPS/IPES measurements, yielding a significant larger Na:In_xS_y band gap of $E_{Gap}^{Surf} = (2.60 \pm 0.11)$ eV. The increased band gap yields a significant spike in the conduction band offset of the non-annealed Na:In_xS_y/CISSe interface.
After the annealing step, the copper diffusion is reduced by more than a factor of two in comparison to the annealed In_xS_y buffer layer at the surface. The annealed surface band gap is significantly reduced to $E_{Gap}^{Surf} = (2.11 \pm 0.11)$ eV compared to the non-annealed one. This can possibly be explained by a copper accumulation at the buffer surface. A reduced copper concentration in the bulk might lead to an increased bulk band gap of the Na:In_xS_y layer. In addition, a selenium diffusion appears for the Na:In_xS_y buffer. This suggests that the $CuIn(S,Se)_2$ surface becomes Cu and Se depleted, while the Na:In_xS_y buffer becomes Cu and Se enriched. Likewise to the In_xS_y/CISSe interface, the copper diffusion should decrease the interface recombination due to an increase of the distance of the VBM and E_F as stated above. Furthermore, the Se depletion is expected to shift the conduction band minimum away from E_F which suggests that the spike in the CBM gets reduced.
Under the assumption of a Se-free absorber surface, a flat band alignment might occur. However, several theoretical publications report that a spike in the conduction band alignment might be beneficial [52–54, 180] or at least not deteriorating the efficiency [55]. In contrast, other theoretical [61] and experimental work [8, 9, 236] interpret a flat alignment as ideal for the charge carrier transport. The here presented results, in particular the dependence of the conduction band offset of the In_xS_y/CISSe interface for different indium contents of the In_xS_y layer, suggest a flat offset as ideal. The high efficiency of solar cells with a Na:In_xS_y buffer can be explained as follows: the Na:In_xS_y surface band gap is possibly significantly smaller than the bulk band gap due to a copper accumulation at the buffer layer surface. Hence, one may speculate that light is not significant absorbed in the buffer layer. In addition, the copper diffusion from the absorber into the buffer is expected to deplete the absorber surface of copper, similar to the behavior observed for the undoped buffer layer. This comes along with a reduced recombination at the Na:In_xS_y/CISSe interface. A CBO which is smaller than 0.3 eV due to the Se diffusion is also suggested. The latter facts probably explain the high efficiency of solar cells with this buffer layer.

The impact of the front contact deposition was simulated by the post-annealing treatments. This treatment only allows to investigate the influence on the electronic and chemical properties while the physical impact of the ZnO sputter process is neglected. Therefore, the i-ZnO/Na:In_xS_y interface was further investigated. A significant interdiffusion attributed

to the sputter process, i.e., the formation of ZnS and SO_4^{2-}-bonds was observed at the interface. The investigation of the S-related local density of states with XES yields $ZnSO_4$ and/or $In_2(SO_4)_3$ as most likely compounds. An additional annealing step indicates that the copper diffusion from the CISSe absorber into the Na:In_xS_y layer still takes place and that the copper as well as selenium diffusion stops at the i-ZnO/Na:In_xS_y interface. UPS/IPES measurements revealed a cliff-like alignment at the interface which is not altered by the annealing step. However, the formation of ZnS at the interface may lead to a band alignment which is more favorable in terms of the solar cell efficiency, e.g., a reduction of the cliff-like conduction band offset. ZnS has a similar band gap to ZnO but the relative position of the VBM is shifted towards E_F and accordingly the CBM away from E_F. It was suggested [192] that the positive effect of the annealing step at 200 °C of an In_xS_y-buffered CIGSSe solar cell might be related to the i-ZnO/In_xS_y interface. In contrast, in this thesis a positive effect is assigned to the formation of ZnS at the window/buffer interface which possibly reduces the cliff in the band alignment.
In Fig. 8.1, a sketch of the proposed model for the band alignment of the i-ZnO/Na:In_xS_y/ CISSe layer stack is given before and after the annealing step.

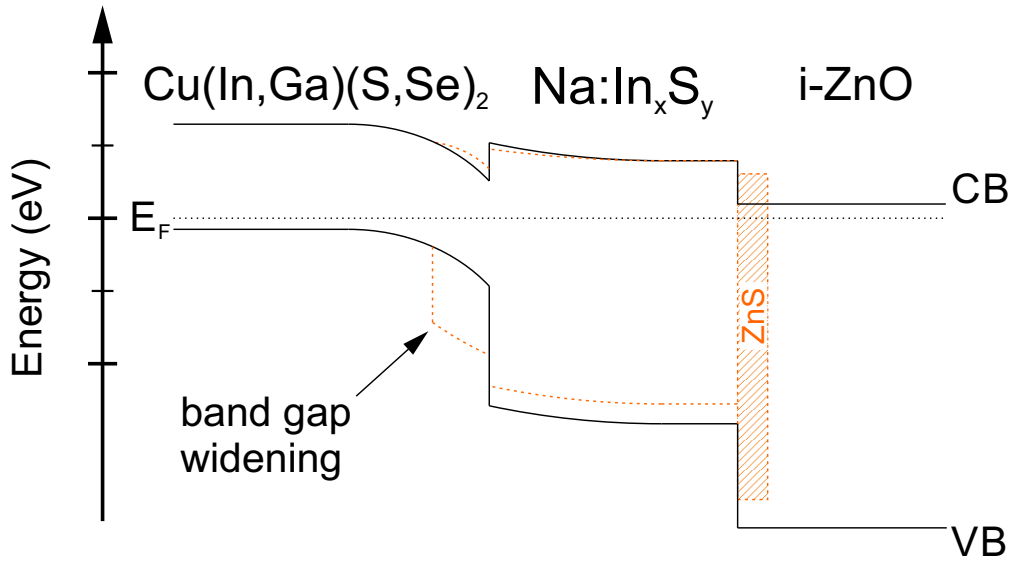

Figure 8.1: Sketch of the proposed band structure model before (black) and after annealing (dashed orange) of the Na:In_xS_y buffered solar cell with the i-ZnO part of the front contact. After the annealing step, the conduction band offset at the buffer/absorber interface is reduced and thus more favorable. The Cu depleted CISSe surface leads to the widening of the band gap at the surface-near region of the absorber resulting in a reduced interface recombination. The formation of ZnS may lead to a reduction of the cliff at the i-ZnO/Na:In_xS_y interface.

As shown in the first part of this thesis, contaminations at the absorber surface are formed within several hours, probably enhancing the interface recombination. Although the interface recombination can be minimized by an annealing step at 200 °C, the air-exposure should be minimized during processing. Hence, the thermal budget of the window layer deposition can possibly be reduced in order to minimize the Cu diffusion and not to deteriorate the buffer layer band gap. In order to get further insights into the In_xS_y/CISSe interface, it would be interesting to investigate the impact of Cu-poor and Cu-rich absorbers on the diffusion behavior. In this context, an Ar^+ ion sputter-induced removal of the In_xS_y layer is promising [140] to gain a depth-profile of the chemical composition.

In addition to the possible improvements directly related to indium sulfide buffer layers, superior efficiencies of up to 21.7 % were achieved in the last two years by utilizing a post-deposition treatment of the CIGSSe layer with potassium [1, 237]. This shows the potential for further improvements for the CIGSSe thin-film based solar cell technology. In this context, it would be interesting to investigate the buffer/absorber band alignment with and without an alkali treatment.

Besides the characterization of the chemical and electronic properties of the solar cell's surface, the optical properties were determined with the reflective electron energy loss spectroscopy (reflective EELS). An EELS spectrum consists of the higher loss energy (≥ 100 eV) which is typically utilized for a quantitative analysis. However, the low energy loss region (≤ 100 eV) is of major interest in this thesis. It provides fundamental information of the investigated samples because the inelastic scattering cross section $\lambda K(E)$ is linked to the dielectric function. Although in a reflective EELS experiment the contribution of the surface is probably overestimated, the determined optical properties of the In_xS_y layer surface are in good agreement with bulk-sensitive measurements. In particular, the band gaps fit the optical band gaps [121] as well as the ones measured by UPS/IPES in this work. One should note that the CISSe excitonic surface band gap was determined to be $E_{Gap}^{surf} = (1.4 \pm 0.2)$ eV providing for the first time an independent but complementary result of earlier performed UPS/IPES measurements. This result proves that the approach of the determination of the conduction band minimum with the help of XPS-derived valence band maxima and optical-derived band gaps leads to a significant underestimation of the position of the CBM.

Moreover, utilizing different primary electron energies in a REELS experiment allows to gather depth-resolved information of the surface dielectric function. In future experiments, the determined $\lambda K(E)$ may allow to describe the real background in XPS spectra better than the Shirley or Tougaard background approach [31, 238]. This is in particular interesting, as the background in XPS spectra provides further information on a sample, e.g., a change in morphology after annealing which can be disentangled with the help of $\lambda K(E)$.

A

Appendix

A.1 Band gap fit function and fit parameter for REELS

Band gap fit function

Assuming that the broadening in a REELS experiment is Gaussian-like, the band gap fit function is a convolution of a chosen "fit function" and a Gaussian. Since the onset of the inelastic-scattered electrons is assumed to be linear, a linear function is used as "fit function" which is zero for energies smaller than E_{Gap} and then rises linearly:

$$g(x) = \begin{cases} 0, & E < E_{Gap} \\ m \cdot x - E_{Gap} \cdot m, & E \geq E_{Gap} \end{cases} \tag{A.1}$$

Here, E_{Gap} is the band gap. Simultaneously, the intersection with the y-axis is determined by E_{Gap}. The zero for E < E_{Gap} is realized with a Heaviside step function $H(x - E_{Gap})$.

Correspondingly, the convolution can be calculated as follows

$$\begin{aligned} f(x) &= g(x) * \text{Gaussian}(x) \\ &= \left[(m \cdot x - E_{Gap} \cdot m) H(x - E_{Gap})\right] * \left[\frac{1}{\sqrt{2\pi\sigma}} Exp\left(-\frac{x^2}{2\sigma^2}\right)\right] \\ &= \frac{\sqrt{\sigma} m}{2} \left[\sqrt{\frac{2}{\pi}}\sigma \cdot Exp\left(-\frac{(E_{Gap}-x)^2}{2\sigma^2}\right) + (x - E_{Gap}) + (E_{Gap} - x) \cdot Erf\left(\frac{E_{Gap}-x}{\sqrt{2}\sigma}\right)\right] \end{aligned} \tag{A.2}$$

Here, $Erf(x)$ is the error function. This fit function can be easily integrated in a fit procedure in, e.g., Fityk or Igor. The width σ should be set according to the FWHM (= full width at half maximum) of the elastic peak. This should be determined prior to the actual fitting procedure. The FWHM is related to σ according to:

$$\text{FWHM} = 2\sqrt{2\ln 2}\sigma \approx 2.35\sigma \tag{A.3}$$

In Fig. A.1, the determined band gap fit function is exemplarily shown for four different FWHMs.

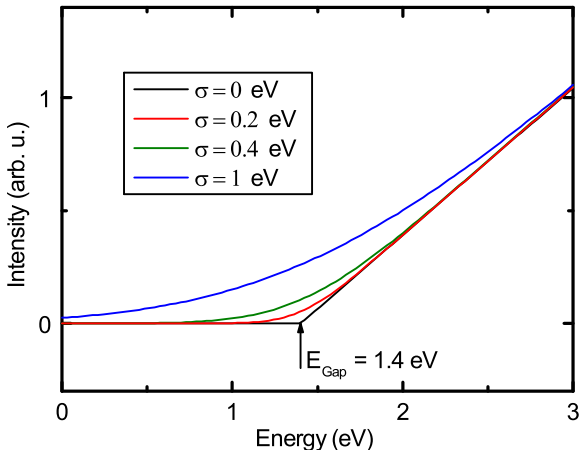

Figure A.1: Plot of the fit function as derived in equation A.1 for different broadenings σ. The bang gap parameter was set to $E_{Gap} = 1.4\,\text{eV}$ and the slope m was adjusted to fit the shown energy window.

Fit parameters used to model the experimental $\lambda K(E)$

Table A.1: Fit parameters used to model the experimental $\lambda K(E)$ for the CISSe absorber for different primary energies.

Absorber	i	$\hbar\omega$ (eV)	A	γ (eV)	α_i
$E_0 = 1000$ eV	1	6.7	1.7	3.2	
	2	9.5	5.4	3.5	
	3	12.7	13.4	3.6	
	4	14.9	49.4	4.5	0.5
	5	16.0	54.7	4.2	
	6	19.5	60.1	4.5	
	7	22.3	43.1	3.6	

Absorber	i	$\hbar\omega$ (eV)	A	γ (eV)	α_i
$E_0 = 500$ eV	1	6.7	1.3	3.0	
	2	9.3	5.5	4.5	
	3	12.7	19.6	5.0	
	4	15.3	36.5	5.0	0.5
	5	16.7	33.9	4.0	
	6	19.0	22.7	3.0	
	7	21.0	68.4	4.0	
	8	25.0	96.5	6.0	

Absorber	i	$\hbar\omega$ (eV)	A	γ (eV)	α_i
$E_0 = 200$ eV	1	6.7	1.4	4.0	
	2	9.8	4.8	5.0	
	3	13.0	14.2	5.5	
	4	16.0	17.1	6.0	
	5	18.5	24.1	6.0	0.5
	6	21.0	34.7	5.0	
	7	24.0	74.6	4.5	
	8	26.5	118.6	5.0	
	9	31.0	174.6	8.0	

Table A.2: Fit parameters used to model the experimental $\lambda K(E)$ for the buffer layer In_xS_y for different primary energies.

In_xS_y	i	$\hbar\omega$ (eV)	A	γ (eV)	α_i
$E_0 = 1000\,\text{eV}$	1	6.5	1.1	2.5	
	2	9.2	6.2	4.0	
	3	12.6	20.0	5.2	
	4	15.7	34.4	4.4	
	5	17.6	31.1	2.2	0.5
	6	19.0	9.1	2.0	
	7	20.5	60.8	3.5	
	8	23.3	81.4	4.0	
	9	28.0	65.4	6.0	

In_xS_y	i	$\hbar\omega$ (eV)	A	γ (eV)	α_i
$E_0 = 500\,\text{eV}$	1	6.7	1.0	2.5	
	2	9.3	5.5	4.5	
	3	12.9	22.4	6.5	
	4	15.5	18.3	5.0	
	5	17.7	18.9	4.0	0.5
	6	19.0	24.4	4.5	
	7	20.5	22.3	4.0	
	8	22.7	128.2	5.5	
	9	27.0	109.0	6.0	

In_xS_y	i	$\hbar\omega$ (eV)	A	γ (eV)	α_i
$E_0 = 200\,\text{eV}$	1	7.3	0.7	3.5	
	2	9.3	4.8	5.0	
	3	12.7	12.8	6.0	
	4	16.0	17.3	6.0	
	5	18.5	18.6	6.0	0.5
	6	21.0	16.4	6.0	
	7	23.0	44.1	6.0	
	8	26.0	230.2	7.0	
	9	30.0	124.6	7.0	

Table A.3: Fit parameters used to model the experimental $\lambda K(E)$ for the annealed buffer layer an-In_xS_y for different primary energies.

annealed In_xS_y	i	$\hbar\omega$ (eV)	A	γ (eV)	α_i
$E_0 = 1000$ eV	1	6.5	1.1	2.5	
	2	10.0	9.5	4.8	
	3	12.7	8.4	3.5	
	4	15.0	11.9	4.0	
	5	16.0	33.4	4.4	0.5
	6	17.8	59.8	3.0	
	7	20.5	45.0	3.0	
	8	23.3	85.9	4.5	
	9	28.0	44.0	6.0	

annealed In_xS_y	i	$\hbar\omega$ (eV)	A	γ (eV)	α_i
$E_0 = 500$ eV	1	7.3	1.2	3	
	2	10.2	7.0	5.0	
	3	13.5	16.3	5.0	
	4	17.0	51.4	6.0	
	5	18.5	36.7	5.0	0.5
	6	21.0	87.2	5.0	
	7	24.0	84.1	5.0	
	8	26.5	37.2	5.0	
	9	31.0	9.7	6.0	

annealed In_xS_y	i	$\hbar\omega$ (eV)	A	γ (eV)	α_i
$E_0 = 200$ eV	1	7.5	0.6	3.5	
	2	9.3	4.1	5.5	
	3	12.7	10.8	6.0	
	4	15.6	20.9	6.0	
	5	18.5	24.4	6.0	0.5
	6	21.0	32.9	6.0	
	7	23.5	44.1	5.6	
	8	25.6	223.4	6.8	
	9	29.0	80.0	5.0	

Bibliography

[1] P. Jackson, D. Hariskos, R. Wuerz, O. Kiowski, A. Bauer, T. M. Friedlmeier, and M. Powalla, "Properties of Cu(In,Ga)Se_2 solar cells with new record efficiencies up to 21.7%", Phys. Stat. Sol. RRL **9**, 28–31 (2015).

[2] M. A. Green, K. Emery, Y. Hishikawa, W. Warta, and E. D. Dunlop, "Solar cell efficiency tables (version 45)", Prog. Photovolt: Res. Appl. **23**, 1–9 (2015).

[3] D. Hariskos, S. Spiering, and M. Powalla, "Buffer layers in Cu(In,Ga)Se_2 solar cells and modules", Thin Solid Films **480-481**, 99–109 (2005).

[4] S. Siebentritt, "Alternative buffers for chalcopyrite solar cells", Sol. Energy **77**, 767–775 (2004).

[5] N. Naghavi, D. Abou-Ras, N. Allsop, N. Barreau, S. Bücheler, A. Ennaoui, C.-H. Fischer, C. Guillen, D. Hariskos, J. Herrero, R. Klenk, K. Kushiya, D. Lincot, R. Menner, T. Nakada, C. Platzer-Björkman, S. Spiering, A. Tiwari, and T. Törndahl, "Buffer layers and transparent conducting oxides for chalcopyrite Cu(In,Ga)(S,$Se)_2$ based thin film photovoltaics: present status and current developments", Prog. Photovolt: Res. Appl. **18**, 411–433 (2010).

[6] J. Palm, T. Dalibor, R. Lechner, S. Pohlner, R. Verma, R. Dietmüller, A. Heiß, H. Vogt, and F. Karg, "Cd-free CIS thin film solar modules at 17 % efficiency", in Proceedings of the 29th EU PVSEC (2014), pp. 1433–1438.

[7] A. Kylner, "The chemical bath deposited CdS/Cu(In,Ga)Se_2 interface as revealed by x-ray photoelectron spectroscopy", J. Electrochem. Soc. **146**, 1816–1823 (1999).

[8] M. Morkel, L. Weinhardt, B. Lohmüller, C. Heske, E. Umbach, W. Riedl, S. Zweigart, and F. Karg, "Flat conduction-band alignment at the CdS/$CuInSe_2$ thin-film solar-cell heterojunction", Appl. Phys. Lett. **79**, 4482–4484 (2001).

[9] L. Weinhardt, M. Morkel, T. Gleim, S. Zweigart, T. P. Niesen, F. Karg, C. Heske, and E. Umbach, "Band alignment at the CdS/CuIn(S,Se)$_2$ heterojunction in thin film solar cells", in Proceedings of the 17th EU PVSEC (2001), pp. 1261–1264.

[10] D. Abou-Ras, G. Kostorz, A. Strohm, H.-W. Schock, and A. N. Tiwari, "Interfacial layer formations between Cu(In,Ga)Se$_2$ and In$_x$S$_y$ layers", J. Appl. Phys. **98**, 123512–123512–7 (2005).

[11] D. Hauschild, F. Meyer, S. Pohlner, R. Lechner, R. Dietmüller, J. Palm, C. Heske, L. Weinhardt, and F. Reinert, "Impact of environmental conditions on the chemical surface properties of Cu(In,Ga)(S,Se)$_2$ thin-film solar cell absorbers", J. Appl. Phys. **115**, 183707 (2014).

[12] D. Hauschild, F. Meyer, A. Benkert, D. Kreikemeyer-Lorenzo, S. Pohlner, J. Palm, M. Blum, W. Yang, R. G. Wilks, M. Bär, C. Heske, L. Weinhardt, and F. Reinert, "Annealing-induced effects on the chemical structure of the In$_2$S$_3$/CuIn(S,Se)$_2$ thin-film solar cell interface", J. Phys. Chem. C **119**, 10412–10416 (2015).

[13] H. Hertz, "Ueber einen Einfluss des ultravioletten Lichtes auf die electrische Entladung", Ann. Phys. **267**, 983–1000 (1887).

[14] W. Hallwachs, "Ueber den Einfluss des Lichtes auf electrostatisch geladene Körper", Ann. Phys. **269**, 301–312 (1888).

[15] A. Einstein, "Über einen die Erzeugung und Verwandlung des Lichtes betreffenden heuristischen Gesichtspunkt", Ann. Phys. **322**, 132–148 (1905).

[16] H. Kuzmany, *Solid-state spectroscopy: an introduction*, 2nd edition (Springer, Heidelberg; New York, 2009), 554 pp.

[17] F. Reinert and S. Hüfner, "Photoemission spectroscopy – from early days to recent applications", New J. Phys. **7**, 97 (2005).

[18] S. Hüfner, *Photoelectron spectroscopy: principles and applications*, 3rd edition (Springer, Berlin; New York, 2003), 662 pp.

[19] G. Borstel and G. Thörner, "Inverse photoemission from solids: theoretical aspects and applications", Surf. Sci. Rep. **8**, 1–41 (1988).

[20] F. J. Himpsel, "Inverse photoemission from semiconductors", Surf. Sci. Rep. **12**, 3–48 (1990).

[21] D. Briggs and J. T. Grant, *Surface analysis by Auger and x-ray photoelectron spectroscopy*, 1st edition (IM Publications, Chichester, 2003), 840 pp.

[22] S. W. Gaarenstroom and N. Winograd, "Initial and final state effects in the ESCA spectra of cadmium and silver oxides", J. Chem. Phys **67**, 3500–3506 (1977).

[23] G. Moretti, "Auger parameter and Wagner plot in the characterization of chemical states by x-ray photoelectron spectroscopy: a review", J. Electron Spectrosc. Relat. Phenom. **95**, 95–144 (1998).

[24] C. Wagner and A. Joshi, "The auger parameter, its utility and advantages: a review", J. Electron Spectrosc. Relat. Phenom. **47**, 283–313 (1988).

[25] C. D. Wagner, "Chemical shifts of Auger lines, and the Auger parameter", Faraday Discuss. Chem. Soc. **60**, 291 (1975).

[26] J. Geiger, *Elektronen und Festkörper*, 1st edition (Vieweg & Sohn GmbH, Braunschweig, 1968), 165 pp.

[27] F. Yubero and S. Tougaard, "Model for quantitative analysis of reflection-electron-energy-loss spectra", Phys. Rev. B **46**, 2486–2497 (1992).

[28] J. Thirlwell, "Characteristic energy losses of low-energy electrons reflected from aluminium and copper", J. Phys. C: Solid State Phys. **1**, 979 (1968).

[29] R. d. L. Kronig, "On the theory of dispersion of x-rays", J. Opt. Soc. Am. **12**, 547–556 (1926).

[30] H. A. Kramers, "La diffusion de la lumiere par les atomes", Atti Cong. Intern. Fisici **2**, 545–557 (1927).

[31] S. Tougaard, "Universality classes of inelastic electron scattering cross-sections", Surf. Interface Anal. **25**, 137–154 (1997).

[32] F. Yubero, J. M. Sanz, B. Ramskov, and S. Tougaard, "Model for quantitative analysis of reflection-electron-energy-loss spectra: angular dependence", Phys. Rev. B **53**, 9719–9727 (1996).

[33] F. Yubero, D. Fujita, B. Ramskov, and S. Tougaard, "Experimental test of model for angular and energy dependence of reflection-electron-energy-loss spectra", Phys. Rev. B **53**, 9728–9732 (1996).

[34] S. Hajati, O. Romanyuk, J. Zemek, and S. Tougaard, "Validity of Yubero-Tougaard theory to quantitatively determine the dielectric properties of surface nanofilms", Phys. Rev. B **77**, 155403 (2008).

[35] M. P. Seah, I. S. Gilmore, and S. J. Spencer, "Background subtraction: II. general behaviour of REELS and the Tougaard universal cross section in the removal of backgrounds in AES and XPS", Surf. Sci. **461**, 1–15 (2000).

[36] S. Tougaard and J. Kraaer, "Inelastic-electron-scattering cross sections for Si, Cu, Ag, Au, Ti, Fe, and Pd", Phys. Rev. B **43**, 1651–1661 (1991).

[37] M. P. Seah and M. T. Anthony, "Quantitative XPS: the calibration of spectrometer intensity–energy response functions. 1–the establishment of reference procedures and instrument behaviour", **6**, 230–241 (1984).

[38] J. Yeh and I. Lindau, "Atomic subshell photoionization cross sections and asymmetry parameters: $1 \leq Z \leq 103$", At. Data Nucl. Data Tables **32**, 1–155 (1985).

[39] J. H. Scofield, "Hartree-Slater subshell photoionization cross-sections at 1254 and 1487 eV", J. Electron Spectrosc. Relat. Phenom. **8**, 129–137 (1976).

[40] R. Hesse, P. Streubel, and R. Szargan, "Improved accuracy of quantitative XPS analysis using predetermined spectrometer transmission functions with UNIFIT 2004", Surf. Interface Anal. **37**, 589–607 (2005).

[41] F. Erfurth, "Elektronenspektroskopie an Cd-freien Pufferschichten und deren Grenzflächen in Cu(In,Ga)(S,Se)$_2$ Dünnschichtsolarzellen", Dissertation (University of Würzburg, 2010), 98 pp.

[42] D. Abou-Ras, T. Kirchartz, and U. Rau, *Advanced characterization techniques for thin film solar cells*, 1st edition (Wiley-VCH Verlag GmbH & Co. KGaA, Weinheim, 2011), 547 pp.

[43] S. Wagner, J. L. Shay, P. Migliorato, and H. M. Kasper, "CuInSe$_2$/CdS heterojunction photovoltaic detectors", Appl. Phys. Lett. **25**, 434–435 (1974).

[44] L. L. Kazmerski, F. R. White, and G. K. Morgan, "Thin-film CuInSe$_2$/CdS heterojunction solar cells", Appl. Phys. Lett. **29**, 268–270 (1976).

[45] D. Lincot and J. Vedel, "Chemical bath deposition of cadmium sulfide thin films", in 10th E.C. photovoltaic solar energy conference (1991), pp. 931–934.

[46] U. Rau, K. Taretto, and S. Siebentritt, "Grain boundaries in Cu(In,Ga)(Se,S)$_2$ thin-film solar cells", Appl. Phys. A **96**, 221–234 (2009).

[47] S. Siebentritt, M. Igalson, C. Persson, and S. Lany, "The electronic structure of chalcopyrites - bands, point defects and grain boundaries", Prog. Photovolt: Res. Appl. **18**, 390–410 (2010).

[48] R. Baier, C. Leendertz, D. Abou-Ras, M. C. Lux-Steiner, and S. Sadewasser, "Properties of electronic potential barriers at grain boundaries in Cu(In,Ga)Se$_2$ thin films", Sol. Energy Mater. Sol. Cells **130**, 124–131 (2014).

[49] M. Turowski, M. K. Kelly, G. Margaritondo, and R. D. Tomlinson, "Direct confirmation of the conduction-band lineup in the CuInSe$_2$/CdS heterojunction solar cell", Appl. Phys. Lett. **44**, 768–770 (1984).

[50] A. J. Nelson, S. Gebhard, A. Rockett, E. Colavita, M. Engelhardt, and H. Höchst, "Synchrotron-radiation photoemission study of CdS/$CuInSe_2$ heterojunction formation", Phys. Rev. B **42**, 7518–7523 (1990).

[51] S.-H. Wei and A. Zunger, "Band offsets at the CdS/$CuInSe_2$ heterojunction", Appl. Phys. Lett. **63**, 2549–2551 (1993).

[52] A. Niemegeers, M. Burgelman, and A. De Vos, "On the CdS/$CuInSe_2$ conduction band discontinuity", Appl. Phys. Lett. **67**, 843 (1995).

[53] R. Klenk, "Characterisation and modelling of chalcopyrite solar cells", Thin Solid Films **387**, 135–140 (2001).

[54] T. Minemoto, Y. Hashimoto, T. Satoh, T. Negami, H. Takakura, and Y. Hamakawa, "Cu(In,Ga)Se_2 solar cells with controlled conduction band offset of window/Cu(In,Ga)Se_2 layers", **89**, 8327–8330 (2001).

[55] T. Minemoto, T. Matsui, H. Takakura, Y. Hamakawa, T. Negami, Y. Hashimoto, T. Uenoyama, and M. Kitagawa, "Theoretical analysis of the effect of conduction band offset of window/CIS layers on performance of CIS solar cells using device simulation", Sol. Energy Mater. Sol. Cells **67**, 83–88 (2001).

[56] R. Scheer and H.-W. Schock, *Chalcogenide photovoltaics: physics, technologies, and thin film devices*, 2nd edition (John Wiley & Sons, 2011), 328 pp.

[57] S. Hüfner, P. Steiner, I. Sander, F. Reinert, and H. Schmitt, "The optical gap of NiO", Z. Phys. B: Condens. Matter **86**, 207–215 (1992).

[58] T. Gleim, C. Heske, E. Umbach, C. Schumacher, S. Gundel, W. Faschinger, A. Fleszar, C. Ammon, M. Probst, and H.-P. Steinrück, "Formation of the ZnSe/(Te/)GaAs(100) heterojunction", Surf. Sci. **531**, 77–85 (2003).

[59] S. Krause, A. Schöll, and E. Umbach, "Determination of transport levels of inorganic semiconductors by ultraviolet and inverse photoemission", Phys. Rev. B **91**, 195101 (2015).

[60] T. Gleim, C. Heske, E. Umbach, C. Schumacher, W. Faschinger, C. Ammon, M. Probst, and H.-P. Steinrück, "Reduction of the ZnSe/GaAs(100) valence band offset by a Te interlayer", Appl. Phys. Lett. **78**, 1867–1869 (2001).

[61] X. Liu and J. R. Sites, "Calculated effect of conduction-band offset on $CuInSe_2$ solar-cell performance", in AIP conference proceedings, Vol. 353 (1996), pp. 444–452.

[62] J. Moulder, W. Stickle, P. Sobol, and K. Bomben, *Handbook of x-ray photoelectron spectroskopy*, 1st edition (Perkin-Elmer Corporation, Physical Electronics Division, Eden Prairie, 1992), 275 pp.

[63] D. Hauschild, "Winkelaufgelöste inverse Photoelektronenspektroskopie an ultradünnen PTCDA Schichten auf Ag(110)", Diploma (University of Würzburg, 2010), 73 pp.

[64] K. Treiber, "Elektronische und chemische Struktur indiumsulfidbasierter Pufferschichten für Cu(In,Ga)(S,Se)$_2$ Dünnschichtsolarzellen", Bachelor Thesis (University of Würzburg, 2013), 29 pp.

[65] H. Yoshida, "Near-ultraviolet inverse photoemission spectroscopy using ultra-low energy electrons", Chem. Phys. Lett. **539–540**, 180–185 (2012).

[66] V. Dose, "VUV isochromat spectroscopy", Appl. Phys. **14**, 117–118 (1977).

[67] D Funnemann and H Merz, "10 eV photon detector for inverse photoemission", J. Phys. E: Sci. Instrum. **19**, 554–557 (1986).

[68] J. Nordgren and J. Guo, "Instrumentation for soft x-ray emission spectroscopy", J. Electron. Spectrosc. Relat. Phenom. **110–111**, 1–13 (2000).

[69] J. J. Jia, T. A. Callcott, J. Yurkas, A. W. Ellis, F. J. Himpsel, M. G. Samant, J. Stöhr, D. L. Ederer, J. A. Carlisle, E. A. Hudson, L. J. Terminello, D. K. Shuh, and R. C. C. Perera, "First experimental results from IBM/TENN/TULANE/LLNL/LBL undulator beamline at the advanced light source", Rev. Sci. Instrum. **66**, 1394–1397 (1995).

[70] M. Bär, N. Barreau, F. Couzinié-Devy, S. Pookpanratana, J. Klaer, M. Blum, Y. Zhang, W. Yang, J. D Denlinger, H. Schock, L. Weinhardt, J. Kessler, and C. Heske, "Nondestructive depth-resolved spectroscopic investigation of the heavily intermixed In_2S_3/Cu(In,Ga)Se_2 interface", Appl. Phys. Lett. **96**, 184101–184101–3 (2010).

[71] M. Blum, L. Weinhardt, O. Fuchs, M. Bär, Y. Zhang, M. Weigand, S. Krause, S. Pookpanratana, T. Hofmann, W. Yang, J. D. Denlinger, E. Umbach, and C. Heske, "Solid and liquid spectroscopic analysis (SALSA)-a soft x-ray spectroscopy endstation with a novel flow-through liquid cell", Rev. Sci. Instrum. **80**, 123102 (2009).

[72] J. E. Jaffe and A. Zunger, "Electronic structure of the ternary chalcopyrite semiconductors $CuAlS_2$, $CuGaS_2$, $CuInS_2$, $CuAlSe_2$, $CuGaSe_2$, and $CuInSe_2$", Phys. Rev. B **28**, 5822–5847 (1983).

[73] K. L. Chopra, P. D. Paulson, and V. Dutta, "Thin-film solar cells: an overview", Prog. Photovolt: Res. Appl. **12**, 69–92 (2004).

[74] S.-H. Wei and A. Zunger, "Band offsets and optical bowings of chalcopyrites and Zn-based II-VI alloys", J. Appl. Phys. **78**, 3846–3856 (1995).

[75] J. C. Rife, "Copper gallium sulfide $CuGaS_2$", in *Handbook of optical constants of solids*, edited by E. D. Palik (Academic Press, Burlington, 1997), pp. 459–471.

[76] M. Bär, W. Bohne, J. Röhrich, E. Strub, S. Lindner, M. C. Lux-Steiner, C.-H. Fischer, T. P. Niesen, and F. Karg, "Determination of the band gap depth profile of the penternary $Cu(In_{(1-x)}Ga_x)(S_ySe_{(1-y)})_2$ chalcopyrite from its composition gradient", J. Appl. Phys. **96**, 3857–3860 (2004).

[77] W. Shockley and H. J. Queisser, "Detailed balance limit of efficiency of p-n junction solar cells", J. Appl. Phys. **32**, 510–519 (1961).

[78] American Society for Testing and Materials (ASTM) Terrestrial Reference Spectra for Photovoltaic Performance Evaluation, *Solar spectral irradiance: air mass 1.5, ASTM G173-03*, (2015) `http://rredc.nrel.gov/solar/spectra/am1.5/` (visited on 07/23/2015).

[79] S. Siebentritt, "What limits the efficiency of chalcopyrite solar cells?", Sol. Energy **95**, 1471–1476 (2011).

[80] T. Dullweber, G. Hanna, U. Rau, and H.-W. Schock, "A new approach to high-efficiency solar cells by band gap grading in $Cu(In,Ga)Se_2$ chalcopyrite semiconductors", Sol. Energy Mater. Sol. Cells **67**, 145–150 (2001).

[81] M. Gloeckler and J. R. Sites, "Band-gap grading in $Cu(In,Ga)Se_2$ solar cells", J. Phys. Chem. Solids **66**, 1891–1894 (2005).

[82] B. Dimmler, F. Grunwald, D. Schmid, and H.-W. Schock, "Analysis of UHV prepared CIS films with surface and bulk sensitive methods", in Proceedings of the 22nd IEEE photovoltaic solar energy conference (1991), p. 1088.

[83] L. M. Peter, "Towards sustainable photovoltaics: the search for new materials", Phil. Trans. R. Soc. A **369**, 1840–1856 (2011).

[84] M. Powalla and B. Dimmler, "CIGS solar cells on the way to mass production: process statistics of a 30 cm × 30 cm module line", Sol. Energy Mater. Sol. Cells **67**, 337–344 (2001).

[85] A. Chirilă, S. Buecheler, F. Pianezzi, P. Bloesch, C. Gretener, A. R. Uhl, C. Fella, L. Kranz, J. Perrenoud, S. Seyrling, R. Verma, S. Nishiwaki, Y. E. Romanyuk, G. Bilger, and A. N. Tiwari, "Highly efficient Cu(In,Ga)Se_2 solar cells grown on flexible polymer films", Nature Materials **10**, 857–861 (2011).

[86] F. Kessler, D. Herrmann, and M. Powalla, "Approaches to flexible CIGS thin-film solar cells", Thin Solid Films **480–481**, 491–498 (2005).

[87] K. Moriwaki, M. Nomoto, S. Yuuya, N. Murakami, T. Ohgoh, K. Yamane, S. Ishizuka, and S. Niki, "Monolithically integrated flexible Cu(In,Ga)Se_2 solar cells and submodules using newly developed structure metal foil substrate with a dielectric layer", Sol. Energy Mater. Sol. Cells **112**, 106–111 (2013).

[88] A. Rockett, J. S. Britt, T. Gillespie, C. Marshall, M. M. Al Jassim, F. Hasoon, R. Matson, and B. Basol, "Na in selenized Cu(In,Ga)Se_2 on Na-containing and Na-free glasses: distribution, grain structure, and device performances", Thin Solid Films **372**, 212–217 (2000).

[89] V. Probst, J. Rimmasch, W. Riedl, W. Stetter, J. Holz, H. Harms, F. Karg, and H.-W. Schock, "The impact of controlled sodium incorporation on rapid thermal processed Cu(InGa)Se_2-thin films and devices", in IEEE photovoltaic specialists conference, Vol. 1 (1994), pp. 144–147.

[90] M. Ruckh, D. Schmid, M. Kaiser, R. Schäffler, T. Walter, and H.-W. Schock, "Influence of substrates on the electrical properties of Cu(In,Ga)Se_2 thin films", Sol. Energy Mater. Sol. Cells **41-42**, 335–343 (1996).

[91] F. Karg, "High efficiency CIGS solar modules", Energy Procedia **15**, 275–282 (2012).

[92] T. Dalibor, S. Jost, H. Vogt, R. Brenning, A. Heiß, S. Visbeck, T. Happ, J. Palm, A. Avellán, T. Niesen, and F. Karg, "Advanced CIGSSe device for module efficiencies above 15%", in Proceedings of the 25th EU PVSEC (2010), pp. 2854 –2857.

[93] T. Dalibor, S. Jost, H. Vogt, A. Heiß, S. Visbeck, T. Happ, J. Palm, A. Avellán, T. Niesen, and F Karg, "Towards module efficiencies of 16% with an improved CIGSSe device design", in Proceedings of the 26th EU PVSEC (2011), pp. 2407 –2411.

[94] J. Palm, V. Probst, W. Stetter, R. Toelle, S. Visbeck, H. Calwer, T. Niesen, H. Vogt, O. Hernández, M. Wendl, and F. Karg, "CIGSSe thin film PV modules: from fundamental investigations to advanced performance and stability", Thin Solid Films **451–452**, 544–551 (2004).

[95] G. Hanna, A. Jasenek, U. Rau, and H.-W. Schock, "Influence of the Ga-content on the bulk defect densities of Cu(In,Ga)Se_2", Thin Solid Films **387**, 71–73 (2001).

[96] C. Heske, G. Richter, Z. Chen, R. Fink, E. Umbach, W. Riedl, and F. Karg, "Influence of Na and H_2O on the surface properties of Cu(In,Ga)Se_2 thin films", J. Appl. Phys. **82**, 2411 (1997).

[97] L. Weinhardt, O. Fuchs, A. Peter, E. Umbach, C. Heske, J. Reichardt, M. Bär, I. Lauermann, I. Kötschau, A. Grimm, S. Sokoll, M. C. Lux-Steiner, T. P Niesen, S. Visbeck, and F. Karg, "Spectroscopic investigation of the deeply buried Cu(In,Ga)(S,$Se)_2$/Mo interface in thin-film solar cells", J. Chem. Phys. **124**, 074705–074705–5 (2006).

[98] C. H. Fischer, M. Bär, T. Glatzel, I. Lauermann, and M. C. Lux-Steiner, "Interface engineering in chalcopyrite thin film solar devices", Sol. Energy Mater. Sol. Cells **90**, 1471–1485 (2006).

[99] W. Witte, S. Spiering, and D. Hariskos, "Substitution of the CdS buffer layer in CIGS thin-film solar cells", Vakuum in Forschung und Praxis **26**, 23–27 (2014).

[100] D. Schmid, M. Ruckh, and H.-W. Schock, "A comprehensive characterization of the interfaces in Mo/CIS/CdS/ZnO solar cell structures", Sol. Energy Mater. Sol. Cells **41-42**, 281–294 (1996).

[101] M. Bär, H.-J. Muffler, C.-H. Fischer, S. Zweigart, F. Karg, and M. C. Lux-Steiner, "ILGAR-ZnO window extension layer: an adequate substitution of the conventional CBD-CdS buffer in Cu(In,Ga)(S,$Se)_2$-based solar cells with superior device performance", Prog. Photovolt: Res. Appl. **10**, 173–184 (2002).

[102] T. Nakada, M. Mizutani, Y. Hagiwara, and A. Kunioka, "High-efficiency Cu(In,Ga)Se_2 thin-film solar cells with a CBD-ZnS buffer layer", Sol. Energy Mater. Sol. Cells **67**, 255–260 (2001).

[103] R. N. Bhattacharya and K. Ramanathan, "Cu(In,Ga)Se_2 thin film solar cells with buffer layer alternative to CdS", Sol. Energy **77**, 679–683 (2004).

[104] R. Hunger, M. V. Lebedev, K. Sakurai, T. Schulmeyer, T. Mayer, A. Klein, S. Niki, and W. Jaegermann, "Junction formation of $CuInSe_2$ with CdS: a comparative study of "dry" and "wet" interfaces", Thin Solid Films **515**, 6112–6118 (2007).

[105] J. Marlein, K. Decock, and M. Burgelman, "Analysis of electrical properties of CIGSSe and Cd-free buffer CIGSSe solar cells", Thin Solid Films **517**, 2353–2356 (2009).

[106] R. Sáez-Araoz, J. Krammer, S. Harndt, T. Koehler, M. Krueger, P. Pistor, A. Jasenek, F. Hergert, M. C. Lux-Steiner, and C.-H. Fischer, "ILGAR In_2S_3 buffer layers for Cd-free Cu(In,Ga)(S,Se)$_2$ solar cells with certified efficiencies above 16%", Prog. Photovoltaics **20**, 855–861 (2012).

[107] C.-H. Fischer, N. A. Allsop, S. E. Gledhill, T. Köhler, M. Kröger, R. Sáez-Araoz, Y. Fu, R. Schwieger, J. Richter, P. Wohlfart, P. Bartsch, N. Lichtenberg, and M. C. Lux-Steiner, "The spray-ILGAR®(ion layer gas reaction) method for the deposition of thin semiconductor layers: process and applications for thin film solar cells", Sol. Energy Mater. Sol. Cells, Special Issue : Thin film and nanostructured solar cells **95**, 1518–1526 (2011).

[108] F. Erfurth, A. Grimm, J. Palm, T. P. Niesen, F. Reinert, L. Weinhardt, and E. Umbach, "Direct determination of the band alignment at the (Zn,Mg)O/CISSe interface", Appl. Phys. Lett. **98**, 142107 (2011).

[109] M. Nakamura, Y. Kouji, Y. Chiba, H. Hakuma, T. Kobayashi, and T. Nakada, "Achievement of 19.7% efficiency with a small-sized Cu(In,Ga)(Se,S)$_2$ solar cells prepared by sulfurization after selenizaion process with Zn-based buffer", in Photovoltaic specialists conference (PVSC), IEEE 39th (2013), pp. 0849–0852.

[110] N. Barreau, J. C. Bernède, C. Deudon, L. Brohan, and S. Marsillac, "Study of the new β-In_2S_3 containing Na thin films part I: synthesis and structural characterization of the material", J. Cryst. Growth **241**, 4–14 (2002).

[111] M. A. Green, K. Emery, Y. Hishikawa, W. Warta, and E. D. Dunlop, "Solar cell efficiency tables (version 44)", Prog. Photovolt: Res. Appl. **22**, 701–710 (2014).

[112] M. Powalla, W. Witte, P. Jackson, S. Paetel, E. Lotter, R. Wuerz, F. Kessler, C. Tschamber, W. Hempel, D. Hariskos, R. Menner, A. Bauer, S. Spiering, E. Ahlswede, T. Friedlmeier, D. Blazquez-Sanchez, I. Klugius, and W. Wischmann, "CIGS cells and modules with high efficiency on glass and flexible substrates", IEEE Journal of Photovoltaics **4**, 440–446 (2014).

[113] A. Hultqvist, C. Platzer-Björkman, T. Tröndahl, M. Ruth, and M. Edoff, "Optimization of i-ZnO window layers for Cu(In,Ga)Se_2 solar cells with ALD buffers", in Proceedings of the 22nd EU PVSEC (2007), p. 2381.

[114] W. J. Duffin and J. H. C. Hogg, "Crystalline phases in the system In-In_2S_3", Acta Cryst. **20**, 566–569 (1966).

[115] C.-H. Ho, Y.-P. Wang, and Y.-S. Huang, "Optical characterization of band-edge property of In_6S_7 compound", J. Appl. Phys. **100**, 131905 (2012).

[116] M. A. M. Seyam, "Optical and electrical properties of indium monosulfide (InS) thin films", Vacuum **63**, 441–447 (2001).

[117] R. Diehl and R. Nitsche, "Vapour growth of three In_2S_3 modifications by iodine transport", J. Cryst. Growth **28**, 306–310 (1975).

[118] T. Gödecke and K. Schubert, "On the phase diagram InS_m", Zeitschrift für Metallkunde **76**, 358 –364 (1995).

[119] P. Pistor, "Formation and electronic properties of In_2S_3/Cu(In,Ga)Se_2 junctions and related thin film solar cells", Dissertation (University of Berlin, 2009), 168 pp.

[120] S. Pohlner, private communication, 2012.

[121] N. Barreau, "Indium sulfide and relatives in the world of photovoltaics", Sol. Energy **83**, 363–371 (2009).

[122] A. Lafond, C. Guillot-Deudon, S. Harel, A. Mokrani, N. Barreau, S. Gall, and J. Kessler, "Structural study and electronic band structure investigations of the solid solution $Na_xCu_{1-x}In_5S_8$ and its impact on the Cu(In,Ga)Se_2/In_2S_3 interface of solar cells", Thin Solid Films **515**, 6020–6023 (2007).

[123] C. Guillot-Deudon, S. Harel, A. Mokrani, A. Lafond, N. Barreau, V. Fernandez, and J. Kessler, "Electronic structure of $Na_xCu_{1-x}In_5S_8$ compounds: x-ray photoemission spectroscopy study and band structure calculations", Phys. Rev. B **78**, 235201 (2008).

[124] N. Barreau, J. Bernède, S. Marsillac, C. Amory, and W. Shafarman, "New Cd-free buffer layer deposited by PVD: In_2S_3 containing Na compounds", Thin Solid Films **431-432**, 326–329 (2003).

[125] P. Pistor, N. Allsop, W. Braun, R. Caballero, C. Camus, C.-H. Fischer, M. Gorgoi, A. Grimm, B. Johnson, T. Kropp, I. Lauermann, S. Lehmann, H. Mönig, S. Schorr, A. Weber, and R. Klenk, "Cu in In_2S_3: interdiffusion phenomena analysed by high kinetic energy x-ray photoelectron spectroscopy", Phys. Stat. Sol. (a) **206**, 1059–1062 (2009).

[126] N. Barreau, C. Deudon, A. Lafond, S. Gall, and J. Kessler, "A study of bulk $Na_xCu_{1-x}In_5S_8$ and its impact on the Cu(In,Ga)Se_2/In_2S_3 interface of solar cells", Sol. Energy Mater. Sol. Cells **90**, 1840–1848 (2006).

[127] N. Barreau, S. Marsillac, D. Albertini, and J. C. Bernede, "Structural, optical and electrical properties of β-$In_2S_{3-3x}O_{3x}$ thin films obtained by PVD", Thin Solid Films **403**, 331–334 (2002).

[128] W. Metzger, I. Repins, M. Romero, P. Dippo, M. Contreras, R. Noufi, and D. Levi, "Recombination kinetics and stability in polycrystalline Cu(In,Ga)Se_2 solar cells", Thin Solid Films **517**, 2360–2364 (2009).

[129] T. Sakurai, N. Ishida, S. Ishizuka, M. Islam, A. Kasai, K. Matsubara, K. Sakurai, A. Yamada, K. Akimoto, and S. Niki, "Effects of annealing under various atmospheres on electrical properties of Cu(In,Ga)Se_2 films and CdS/Cu(In,Ga)Se_2 heterostructures", Thin Solid Films **516**, 7036–7040 (2008).

[130] U. Rau, D. Braunger, R. Herberholz, H.-W. Schock, J. F Guillemoles, L. Kronik, and D. Cahen, "Oxygenation and air-annealing effects on the electronic properties of Cu(In,Ga)Se_2 films and devices", J. Appl. Phys. **86**, 497–505 (1999).

[131] M. Schmidt, D. Braunger, R. Schäffler, H.-W. Schock, and U. Rau, "Influence of damp heat on the electrical properties of Cu(In,Ga)Se_2 solar cells", Thin Solid Films **361-362**, 283–287 (2000).

[132] J. Reichardt, M. Bär, A. Grimm, I. Kötschau, I. Lauermann, S. Sokoll, M. C. Lux-Steiner, C.-H. Fischer, C. Heske, L. Weinhardt, O. Fuchs, C. Jung, W. Gudat, T. Niesen, and F. Karg, "Inducing and monitoring photoelectrochemical reactions at surfaces and buried interfaces in Cu(In,Ga)$(S,Se)_2$ thin-film solar cells", Appl. Phys. Lett. **86**, 172102–172102–3 (2005).

[133] R. Würz, M. Rusu, T. Schedel-Niedrig, M. Lux-Steiner, H. Bluhm, M. Hävecker, E. Kleimenov, A. Knop-Gericke, and R. Schlögl, "In situ x-ray photoelectron spectroscopy study of the oxidation of $CuGaSe_2$", Surf. Sci. **580**, 80–94 (2005).

[134] D. Regesch, L. Gütay, J. K. Larsen, V. Deprédurand, D. Tanaka, Y. Aida, and S. Siebentritt, "Degradation and passivation of CuInSe2", Appl. Phys. Lett. **101**, 112108–112108–4 (2012).

[135] C. Heske, U. Groh, O. Fuchs, L. Weinhardt, E. Umbach, T. Schedel-Niedrig, C.-H. Fischer, M. C. Lux-Steiner, S. Zweigart, T. P. Niesen, F. Karg, J. D. Denlinger, B. Rude, C. Andrus, and F. Powell, "Monitoring chemical reactions at a liquid-solid interface: water on CuIn$(S,Se)_2$ thin film solar cell absorbers", J. Chem. Phys **119**, 10467 (2003).

[136] C. Heske, U. Groh, L. Weinhardt, O. Fuchs, B. Holder, E. Umbach, C. Bostedt, L. J. Terminello, S. Zweigart, T. P. Niesen, and F. Karg, "Damp-heat induced sulfate formation in Cu(In,Ga)$(S,Se)_2$-based thin film solar cells", Appl. Phys. Lett. **81**, 4550–4552 (2002).

[137] M. Kunat, S. G. Girol, U. Burghaus, and C. Wöll, "The interaction of water with the oxygen-terminated, polar surface of ZnO", J. Phys. Chem. B **107**, 14350–14356 (2003).

[138] L. Weinhardt, O. Fuchs, D. Groß, E. Umbach, C. Heske, N. G. Dhere, A. A. Kadam, and S. S. Kulkarni, "Surface modifications of Cu(In,Ga)S_2 thin film solar cell absorbers by KCN and H_2O_2/H_2SO_4 treatments", J. Appl. Phys. **100**, 024907–024907–4 (2006).

[139] K. Granath, M. Bodegård, and L. Stolt, "The effect of NaF on Cu(In,Ga)Se_2 thin film solar cells", Sol. Energy Mater. Sol. Cells **60**, 279–293 (2000).

[140] S. Gall, N. Barreau, F. Jacob, S. Harel, and J. Kessler, "Influence of sodium compounds at the Cu(In,Ga)Se_2/(PVD)In_2S_3 interface on solar cell properties", Thin Solid Films **515**, 6076–6079 (2007).

[141] D. Braunger, D. Hariskos, G. Bilger, U. Rau, and H.-W. Schock, "Influence of sodium on the growth of polycrystalline Cu(In,Ga)Se_2 thin films", Thin Solid Films **361-362**, 161–166 (2000).

[142] D. W. Niles, "Na impurity chemistry in photovoltaic CIGS thin films: investigation with x-ray photoelectron spectroscopy", J. Vac. Sci. Technol. A **15**, 3044 (1997).

[143] A. Klein and W. Jaegermann, "Fermi-level-dependent defect formation in Cu-chalcopyrite semiconductors", Appl. Phys. Lett. **74**, 2283–2285 (1999).

[144] D. Schmid, M. Ruckh, F. Grunwald, and H.-W. Schock, "Chalcopyrite/defect chalcopyrite heterojunctions on the basis of $CuInSe_2$", J. Appl. Phys. **73**, 2902–2909 (1993).

[145] R. Bayón, C. Maffiotte, and J. Herrero, "Chemical bath deposition of indium hydroxy sulphide thin films: process and XPS characterization", Thin Solid Films **353**, 100–107 (1999).

[146] J. Ghijsen, L. H. Tjeng, J. van Elp, H. Eskes, J. Westerink, G. A. Sawatzky, and M. T. Czyzyk, "Electronic structure of Cu_2O and CuO", Phys. Rev. B **38**, 11322–11330 (1988).

[147] D. Cahen and R. Noufi, "Defect chemical explanation for the effect of air anneal on CdS/$CuInSe_2$ solar cell performance", Appl. Phys. Lett. **54**, 558–560 (1989).

[148] M. Bär, N. Allsop, I. Lauermann, and C.-H. Fischer, "Deposition of In_2S_3 on Cu(In,Ga)$(S,Se)_2$ thin film solar cell absorbers by spray ion layer gas reaction: evidence of strong interfacial diffusion", Appl. Phys. Lett. **90**, 132118–132118–3 (2007).

[149] N. Allsop, A. Schönmann, A. Belaidi, H.-J. Muffler, B. Mertesacker, W. Bohne, E. Strub, J. Röhrich, M. Lux-Steiner, and C.-H. Fischer, "Indium sulfide thin films deposited by the spray ion layer gas reaction technique", Thin Solid Films **513**, 52–56 (2006).

[150] J. Sterner, J. Malmström, and L. Stolt, "Study on ALD In_2S_3/Cu(In,Ga)Se_2 interface formation", Prog. Photovolt: Res. Appl. **13**, 179–193 (2005).

[151] T. Asikainen, M. Ritala, and M. Leskelä, "Growth of In_2S_3 thin films by atomic layer epitaxy", Appl. Surf. Sci. **82–83**, 122–125 (1994).

[152] N. Naghavi, R. Henriquez, V. Laptev, and D. Lincot, "Growth studies and characterisation of In_2S_3 thin films deposited by atomic layer deposition (ALD)", Appl. Surf. Sci. **222**, 65–73 (2004).

[153] W. Rehwald and G. Harbeke, "On the conduction mechanism in single crystal β-indium sulfide In_2S_3", J. Phys. Chem. Solids **26**, 1309–1324 (1965).

[154] N. Barreau, S. Marsillac, J. Bernède, T. Ben Nasrallah, and S. Belgacem, "Optical properties of wide band gap indium sulphide thin films obtained by physical vapor deposition", Phys. Stat. Sol. (a) **184**, 179–186 (2001).

[155] N. Barreau, A. Mokrani, F. Couzinié-Devy, and J. Kessler, "Bandgap properties of the indium sulfide thin-films grown by co-evaporation", Thin Solid Films **517**, 2316–2319 (2009).

[156] N. Naghavi, S. Spiering, M. Powalla, B. Cavana, and D. Lincot, "High-efficiency copper indium gallium diselenide (CIGS) solar cells with indium sulfide buffer layers deposited by atomic layer chemical vapor deposition (ALCVD)", Prog. Photovolt: Res. Appl. **11**, 437–443 (2003).

[157] H. A. Maksoud, M. Igalson, and S. Spiering, "Influence of post-deposition heat treatment on electrical transport properties of In_2S_3-buffered Cu(In,Ga)Se_2 cells", Thin Solid Films **535**, 158–161 (2013).

[158] T. Schulmeyer, A. Klein, R. Kniese, and M. Powalla, "Band offset at the $CuGaSe_2$/In_2S_3 heterointerface", Appl. Phys. Lett. **85**, 961–963 (2004).

[159] S. Pohlner, "Impact of indium sulphide based buffer layers on the electrical properties of CIGSSe thin film solar cells", Dissertation (University of Jena, 2013), 113 pp.

[160] S. Tanuma, C. J. Powell, and D. R. Penn, "Calculations of electron inelastic mean free paths. v. data for 14 organic compounds over the 50-2000 eV range", Surf. Interface Anal. **21**, 165–176 (1994).

[161] C. Laurencic, L. Arzel, F. Couzinié-Devy, and N. Barreau, "Investigation of Cu(In,Ga)Se_2/In_2S_3 diffuse interface by Raman scattering", Thin Solid Films **519**, 7553–7555 (2011).

[162] D. Ferro, V. Piacente, and P. Scardala, "Sublimation behaviour of indium trisulphide studied by a simultaneous torsion and knudsen technique", J. Mater. Sci. Lett. **7**, 1301–1304 (1988).

[163] A. Strohm, L. Eisenmann, R. Gebhardt, A. Harding, T. Schlötzer, D. Abou-Ras, and H.-W. Schock, "ZnO/In_xS_y/Cu(In,Ga)Se_2 solar cells fabricated by coherent heterojunction formation", Thin Solid Films **480-481**, 162–167 (2005).

[164] L. Gastaldi and L. Scaramuzza, "Single-crystal structure analysis of the spinel copper pentaindium octasulphide", Acta Cryst. **36**, 2751–2753 (1980).

[165] R. Scheer and H. J. Lewerenz, "Photoemission study of evaporated $CuInS_2$ thin films. II. electronic surface structure", J. Vac. Sci. Technol. A **12**, 56–60 (1994).

[166] S. Kohiki, M. Nishitani, T. Negami, and T. Wada, "X-ray photoelectron spectroscopy of $CuInSe_2$", Phys. Rev. B **45**, 9163–9168 (1992).

[167] D. Cahen, P. J. Ireland, L. L. Kazmerski, and F. A. Thiel, "X-ray photoelectron and Auger electron spectroscopic analysis of surface treatments and electrochemical decomposition of $CuInSe_2$ photoelectrodes", J. Appl. Phys. **57**, 4761–4771 (1985).

[168] M. Bär, J. Klaer, R. Félix, N. Barreau, L. Weinhardt, R. Wilks, C. Heske, and H.-W. Schock, "Surface off-stoichiometry of $CuInS_2$ thin-film solar cell absorbers", IEEE J. Photovolt. **3**, 828–832 (2013).

[169] E. Gullikson, *CXRO x-ray interactions with matter*, `http://henke.lbl.gov/optical_constants/` (visited on 02/11/2015).

[170] B. Henke, E. Gullikson, and J. Davis, "X-ray interactions: photoabsorption, scattering, transmission, and reflection at E = 50-30,000 eV, Z = 1-92", At. Data Nucl. Data Tables **54**, 181–342 (1993).

[171] C. Heske, U. Groh, O. Fuchs, E. Umbach, N. Franco, C. Bostedt, L. Terminello, R. Perera, K. Hallmeier, A. Preobrajenski, R. Szargan, S. Zweigart, W. Riedl, and F. Karg, "X-ray emission spectroscopy of Cu(In,Ga)$(S,Se)_2$-based thin film solar cells: electronic structure, surface oxidation, and buried interfaces", Phys. Stat. Sol. (a) **187**, 13–24 (2001).

[172] M. I. Alonso, M. Garriga, C. A. D. Rincón, E. Hernéndez, and M. León, "Optical functions of chalcopyrite $CuGa_xIn_{1-x}Se_2$ alloys", Appl. Phys. A **74**, 659–664 (2002).

[173] K. Orgassa, *Coherent optical analysis of the ZnO/CdS/Cu(In,Ga)Se_2 thin film solar cell*, 1st edition (Shaker-Verlag, Aachen, 2004), 154 pp.

[174] P. D. Paulson, R. W. Birkmire, and W. N. Shafarman, "Optical characterization of $CuIn_{1-x}Ga_xSe_2$ alloy thin films by spectroscopic ellipsometry", J. Appl. Phys. **94**, 879–888 (2003).

[175] W.-T. Kim and C.-D. Kim, "Optical energy gaps of β-In_2S_3 thin films grown by spray pyrolysis", J. Appl. Phys. **60**, 2631–2633 (1986).

[176] N. Barreau and M. Tessier, "Characterization of indium sulfide thin films containing copper", in MRS proceedings - Symposium M, Vol. 1165 (2009).

[177] A. Usujima, S. Takeuchi, S. Endo, and T. Irie, "Optical and electrical properties of $CuIn_5S_8$ and $AgIn_5S_8$ single crystals", Jpn. J. Appl. Phys. **20**, L505–L507 (1981).

[178] F. Couzinié-Devy, N. Barreau, and J. Kessler, "Influence of absorber copper concentration on the Cu(In,Ga)Se_2/(PVD)In_2S_3 and Cu(In,Ga)Se_2/(CBD)CdS based solar cells performance", Thin Solid Films **517**, 2407–2410 (2009).

[179] S. Spiering, A. Eicke, D. Hariskos, M. Powalla, N. Naghavi, and D. Lincot, "Large-area Cd-free CIGS solar modules with In_2S_3 buffer layer deposited by ALCVD", Thin Solid Films **451-452**, 562–566 (2004).

[180] M. Gloeckler and J. Sites, "Efficiency limitations for wide-band-gap chalcopyrite solar cells", Thin Solid Films **480–481**, 241–245 (2005).

[181] N. Barreau, J. C. Bernède, and S. Marsillac, "Study of the new β-In_2S_3 containing Na thin films. Part II: optical and electrical characterization of thin films", J. Cryst. Growth **241**, 51–56 (2002).

[182] L. Weinhardt, M. Blum, M. Bär, C. Heske, O. Fuchs, E. Umbach, J. Denlinger, K. Ramanathan, and R. Noufi, "Chemical properties of the Cu(In,Ga)Se_2/Mo/glass interfaces in thin film solar cells", Thin Solid Films **515**, 6119–6122 (2007).

[183] A. A. Lavrent'ev, N. Y. Safontseva, V. A. Dubeiko, B. V. Gabrel'yan, and I. Y. Nikiforov, "Electronic band structure of In_2S_3 and $CdIn_2S_4$ semiconductor spinels from the data of x-ray spectroscopy and theoretical calculations", Phys. Solid State **42**, 2047–2053 (2000).

[184] L. Weinhardt, O. Fuchs, D. Groß, G. Storch, E. Umbach, N. G Dhere, A. A Kadam, S. S Kulkarni, and C. Heske, "Band alignment at the CdS/Cu(In,Ga)S_2 interface in thin-film solar cells", Appl. Phys. Lett. **86**, 062109–062109–3 (2005).

[185] R. Scheer, L. Messmann-Vera, R. Klenk, and H.-W. Schock, "On the role of non-doped ZnO in CIGSe solar cells", Prog. Photovolt: Res. Appl. **20**, 619–624 (2012).

[186] G. S. Anderson, W. N. Mayer, and G. K. Wehner, "Sputtering of dielectrics by high-frequency fields", J. Appl. Phys. **33**, 2991–2992 (1962).

[187] S. D. Ekpe and S. K. Dew, "Theoretical and experimental determination of the energy flux during magnetron sputter deposition onto an unbiased substrate", J. Vac. Sci. Technol. A **21**, 476–483 (2003).

[188] S. Ishizuka, K. Sakurai, A. Yamada, K. Matsubara, P. Fons, K. Iwata, S. Nakamura, Y. Kimura, T. Baba, H. Nakanishi, T. Kojima, and S. Niki, "Fabrication of wide-gap $Cu(In_{1-x}Ga_x)Se_2$ thin film solar cells: a study on the correlation of cell performance with highly resistive i-ZnO layer thickness", Sol. Energy Mater. Sol. Cells **87**, 541–548 (2005).

[189] J. Kessler, O. Lundberg, J. Wennerberg, and L. Stolt, "Optimization of RF-sputtered ZnO/ZnO:Al for $Cu(In,Ga)Se_2$ based devices", in Proceedings of the 16th EU PVSEC (2000), pp. 775–778.

[190] L. Weinhardt, C. Heske, E. Umbach, T. P Niesen, S. Visbeck, and F. Karg, "Band alignment at the i-ZnO/CdS interface in $Cu(In,Ga)(S,Se)_2$ thin-film solar cells", Appl. Phys. Lett. **84**, 3175–3177 (2004).

[191] F. Erfurth, B. Hußmann, A. Schöll, F. Reinert, A. Grimm, I. Lauermann, M. Bär, T. Niesen, J. Palm, S. Visbeck, L. Weinhardt, and E. Umbach, "Chemical structure of the $(Zn_{1-x},Mg_x)O/CuIn(S,Se)_2$ interface in thin film solar cells", Appl. Phys. Lett. **95**, 122104 (2009).

[192] Q. Nguyen, K. Orgassa, I. Koetschau, U. Rau, and H.-W. Schock, "Influence of heterointerfaces on the performance of $Cu(In,Ga)Se_2$ solar cells with CdS and $In(OH_x,S_y)$ buffer layers", Thin Solid Films **431-432**, 330–334 (2003).

[193] E. Cadel, N. Barreau, J. Kessler, and P. Pareige, "Atom probe study of sodium distribution in polycrystalline $Cu(In,Ga)Se_2$ thin film", Acta Materialia **58**, 2634–2637 (2010).

[194] C. Heske, R. Fink, E. Umbach, W. Riedl, and F. Karg, "Na-induced effects on the electronic structure and composition of $Cu(In,Ga)Se_2$ thin-film surfaces", Appl. Phys. Lett. **68**, 3431–3433 (1996).

[195] M. Bär, A. Ennaoui, J. Klaer, T. Kropp, R. Sáez-Araoz, N. Allsop, I. Lauermann, H.-W. Schock, and M. C. Lux-Steiner, "Formation of a ZnS/Zn(S,O) bilayer buffer on $CuInS_2$ thin film solar cell absorbers by chemical bath deposition", J. Appl. Phys. **99**, 123503 (2006).

[196] C. Platzer-Björkman, T. Törndahl, D. Abou-Ras, J. Malmström, J. Kessler, and L. Stolt, "Zn(O,S) buffer layers by atomic layer deposition in Cu(In,Ga)Se_2 based thin film solar cells: band alignment and sulfur gradient", J. Appl. Phys. **100**, 044506 (2006).

[197] T. Adler, "Zn(O,S) Puffer Eigenschaften in Cu(In,Ga)Se_2 Solarzellen", Dissertation (TU Darmstadt, 2013), 197 pp.

[198] L. Weinhardt, "Elektronische und chemische Eigenschaften von Grenzflächen und Oberflächen in optimierten Cu(In,Ga)(S,Se)$_2$ Dünnschichtsolarzellen", Dissertation (University of Würzburg, 2005), 153 pp.

[199] A. Meisel, R. Leonhardt, and R. Szargan, *Röntgenspektren und chemische Bindung*, 1st edition (Leipzig Geest & Portig, 1977).

[200] L. Weinhardt, M. Bär, H. J. Muffler, C. H. Fischer, M. C. Lux-Steiner, T. P. Niesen, F. Karg, T. Gleim, C. Heske, and E. Umbach, "Impact of Cd^{2+}-treatment on the band alignment at the ILGAR-ZnO/CuIn(S,Se)$_2$ heterojunction", Thin Solid Films **431–432**, 272–276 (2003).

[201] C. Battistoni, J. L. Dormann, D. Fiorani, E. Paparazzo, and S. Viticoli, "An XPS and Mössbauer study of the electronic properties of $ZnCr_xGa_{2-x}O_4$ spinel solid solutions", Sol. State Comm. **39**, 581–585 (1981).

[202] C. Klauber, "Magnesium Kα x-ray line structure revisited", Appl. Surf. Sci. **70-71**, 35–39 (1993).

[203] M. Bodegård, K. Granath, and L. Stolt, "Growth of Cu(In,Ga)Se_2 thin films by coevaporation using alkaline precursors", Thin Solid Films **361-362**, 9–16 (2000).

[204] J. D. Garcia and J. E. Mace, "Energy level and line tables for one-electron atomic spectra", J. Opt. Soc. Am. **55**, 654–661 (1965).

[205] M. Caglar, S. Ilican, Y. Caglar, and F. Yakuphanoglu, "Electrical conductivity and optical properties of ZnO nanostructured thin film", App. Surf. Sci. **255**, 4491–4496 (2009).

[206] V. Srikant and D. R. Clarke, "On the optical band gap of zinc oxide", J. Appl. Phys. **83**, 5447–5451 (1998).

[207] B. E. Sernelius, K.-F. Berggren, Z.-C. Jin, I. Hamberg, and C. G. Granqvist, "Band-gap tailoring of ZnO by means of heavy Al doping", Phys. Rev. B **37**, 10244–10248 (1988).

[208] N. Fujimura, T. Nishihara, S. Goto, J. Xu, and T. Ito, "Control of preferred orientation for ZnO_x films: control of self-texture", J. Cryst. Growth **130**, 269–279 (1993).

[209] M. Bär, A. Ennaoui, J. Klaer, R. Sáez-Araoz, T. Kropp, L. Weinhardt, C. Heske, H.-W. Schock, C. H. Fischer, and M. C. Lux-Steiner, "The electronic structure of the [Zn(S,O)/ZnS]/$CuInS_2$ heterointerface - impact of post-annealing", Chem. Phys. Lett. **433**, 71–74 (2006).

[210] B. K. Meyer, A. Polity, B. Farangis, Y. He, D. Hasselkamp, T. Krämer, and C. Wang, "Structural properties and bandgap bowing of $ZnO_{1-x}S_x$ thin films deposited by reactive sputtering", Appl. Phys. Lett. **85**, 4929–4931 (2004).

[211] C. Persson, C. Platzer-Björkman, J. Malmström, T. Törndahl, and M. Edoff, "Strong valence-band offset bowing of $ZnO_{1-x}S_x$ enhances p-type nitrogen doping of ZnO-like alloys", Phys. Rev. Lett. **97**, 146403 (2006).

[212] M. Stöger-Pollach, "Optical properties and bandgaps from low loss EELS: pitfalls and solutions", Micron **39**, 1092–1110 (2008).

[213] S. Gusenleitner, E. Handick, D. Hauschild, and F. Reinert, "Quantitative analysis of electron energy loss spectra and modelling of optical properties of multilayer systems for extreme ultraviolet radiation regime", J. Appl. Phys. **115**, 123513 (2014).

[214] S. Lazar, G. A. Botton, M. Y. Wu, F. D. Tichelaar, and H. W. Zandbergen, "Materials science applications of HREELS in near edge structure analysis and low-energy loss spectroscopy", Ultramicroscopy **96**, 535–546 (2003).

[215] B. Rafferty and L. M. Brown, "Direct and indirect transitions in the region of the band gap using electron-energy-loss spectroscopy", Phys. Rev. B **58**, 10326–10337 (1998).

[216] Y. R. Denny, H. C. Shin, S. Seo, S. K. Oh, H. J. Kang, D. Tahir, S. Heo, J. G. Chung, J. C. Lee, and S. Tougaard, "Electronic and optical properties of hafnium indium zinc oxide thin film by XPS and REELS", J. Electron Spectrosc. Relat. Phenom. **185**, 18–22 (2012).

[217] D. Tahir, E. K. Lee, H. L. Kwon, S. Kun Oh, H. J. Kang, S. Heo, E. H. Lee, J. G. Chung, J. C. Lee, and S. Tougaard, "Electronic and optical properties of GIZO thin film grown on SiO_2/Si substrates", Surf. Interface Anal. **42**, 906–910 (2010).

[218] J. Lindhard, "On the properties of a gas of charged particles", Dan. Mat. Fys. Medd. **28** (1954).

[219] R. H. Ritchie, "Plasma losses by fast electrons in thin films", Phys. Rev. **106**, 874–881 (1957).

[220] S. Tougaard and F. Yubero, "QUEELS software package for calculation of surface effects in electron spectra", Surf. Interface Anal. **36**, 824–827 (2004).

[221] D. Tahir and S. Tougaard, "Electronic and optical properties of Cu, CuO and Cu_2O studied by electron spectroscopy", J. Phys.: Condens. Matter **24**, 175002 (2012).

[222] F. Yubero, S. Tougaard, E. Elizalde, and J. M. Sanz, "Dielectric loss function of Si and SiO_2 from quantitative analysis of REELS spectra", Surf. Interface Anal. **20**, 719–726 (1993).

[223] F. Wooten, *Optical properties of solids*, 1st edition (Academic Press, New York, 1972), 272 pp.

[224] C. Sanz, C. Guillén, and J. Herrero, "Annealing of indium sulfide thin films prepared at low temperature by modulated flux deposition", Semicond. Sci. Technol. **28**, 015004 (2013).

[225] M. Calixto-Rodriguez, A. Tiburcio-Silver, A. Ortiz, and A. Sanchez-Juarez, "Opto-electronical properties of indium sulfide thin films prepared by spray pyrolysis for photovoltaic applications", Thin Solid Films **480–481**, 133–137 (2005).

[226] J. C. Ingram, K. W. Nebesny, and J. E. Pemberton, "Optical properties of metal surfaces from electron energy loss spectroscopy in the reflection mode", Appl. Surf. Sci. **44**, 279–291 (1990).

[227] M. I. Alonso, K. Wakita, J. Pascual, M. Garriga, and N. Yamamoto, "Optical functions and electronic structure of $CuInSe_2$, $CuGaSe_2$, $CuInS_2$, and $CuGaS_2$", Phys. Rev. B **63**, 075203 (2001).

[228] P. Lautenschlager, M. Garriga, S. Logothetidis, and M. Cardona, "Interband critical points of GaAs and their temperature dependence", Phys. Rev. B **35**, 9174–9189 (1987).

[229] S. Levcenko, N. N. Syrbu, V. E. Tezlevan, E. Arushanov, S. Doka-Yamigno, T. Schedel-Niedrig, and M. C. Lux-Steiner, "Optical spectra and energy band structure of single crystalline $CuGaS_2$ and $CuInS_2$", J. Phys.: Condens. Matter **19**, 456222 (2007).

[230] O. Madelung, *Semiconductors: data handbook*, 3rd edition (Springer, Berlin, 2004), 691 pp.

[231] G. Yin, C. Merschjann, and M. Schmid, "The effect of surface roughness on the determination of optical constants of $CuInSe_2$ and $CuGaSe_2$ thin films", J. Appl. Phys. **113**, 213510 (2013).

[232] M. P. Seah and W. A. Dench, "Quantitative electron spectroscopy of surfaces: a standard data base for electron inelastic mean free paths in solids", Surf. Interface Anal. **1**, 2–11 (1979).

[233] M. Saad and A. Kassis, "Effect of interface recombination on solar cell parameters", Sol. Energy Mater. Sol. Cells **79**, 507–517 (2003).

[234] M. E. Erkan, V. Chawla, I. Repins, and M. A. Scarpulla, "Interplay between surface preparation and device performance in CZTSSe solar cells: effects of KCN and NH_4OH etching", Sol. Energy Mater. Sol. Cells **136**, 78–85 (2015).

[235] C. Hönes, J. Hackenberg, S. Zweigart, A. Wachau, F. Hergert, and S. Siebentritt, "A comparative study of the annealing behavior of Cu(In,Ga)$(S,Se)_2$ based solar cells with an indium sulfide buffer layer, partly submitted to wet chemical treatments", J. Appl. Phys. **117**, 094503 (2015).

[236] L. Kronik, L. Burstein, M. Leibovitch, Y. Shapira, D. Gal, E. Moons, J. Beier, G. Hodes, D. Cahen, D. Hariskos, R. Klenk, and H.-W. Schock, "Band diagram of the polycrystalline CdS/Cu(In,Ga)Se_2 heterojunction", Appl. Phys. Lett. **67**, 1405–1407 (1995).

[237] A. Chirilă, P. Reinhard, F. Pianezzi, P. Bloesch, A. R. Uhl, C. Fella, L. Kranz, D. Keller, C. Gretener, H. Hagendorfer, D. Jaeger, R. Erni, S. Nishiwaki, S. Buecheler, and A. N. Tiwari, "Potassium-induced surface modification of Cu(In,Ga)Se_2 thin films for high-efficiency solar cells", Nat Mater **12**, 1107–1111 (2013).

[238] D. A. Shirley, "High-resolution x-ray photoemission spectrum of the valence bands of gold", Phys. Rev. B **5**, 4709–4714 (1972).

Own publications

The publications are listed chronologically.

First author

- **D. Hauschild**, F. Meyer, S. Pohlner, R. Lechner, R. Dietmüller, J. Palm, C. Heske, L. Weinhardt, and F. Reinert, "Impact of environmental conditions on the chemical surface properties of Cu(In,Ga)(S,Se)$_2$ thin-film solar cell absorbers", J. Appl. Phys. **115**, 183707 (2014).

- **D. Hauschild**, F. Meyer, A. Benkert, D. Kreikemeyer-Lorenzo, S. Pohlner, J. Palm, M. Blum,W. Yang, R. G.Wilks, M. Bär, C. Heske, L.Weinhardt, and F. Reinert, "Annealing-induced effects on the chemical structure of the In_2S_3/CuIn(S,Se)$_2$ thin-film solar cell interface", J. Phys. Chem. C **119**, 10412-10416 (2015).

- **D. Hauschild**, E. Handick, S. Gusenleitner, F. Meyer, H. Schwab, A. Benkert, S. Pohlner, J. Palm, S. Tougaard, C. Heske, L. Weinhardt, and F. Reinert, "Dielectric and optical properties of Cu(In,Ga)(S,Se)$_2$ and In_xS_y surfaces probed by reflection electron energy loss spectroscopy", to be published (2015).

- **D. Hauschild**, F. Meyer, A. Benkert, D. Kreikemeyer-Lorenzo, S. Pohlner, J. Palm, M. Blum, W. Yang, R.G. Wilks, M. Bär, C. Heske, L. Weinhardt, and F. Reinert, "Chemical and electronic structure of the sodium doped In_xS_y/CuIn(S,Se)$_2$ thin-film solar cell interface", to be published (2015).

Co-author

- M. Wießner, **D. Hauschild**, A. Schöll, F. Reinert, V. Feyer, K. Winkler, and B. Krömker, "Electronic and geometric structure of the PTCDA/Ag(110) interface probed by angle-resolved photoemission", Phys. Rev. B **86**, 045417 (2012).
- S. Gusenleitner, **D. Hauschild**, T. Graber, D. Ehm, S. Tougaard, and F. Reinert, "Factor analysis and advanced inelastic background analysis in XPS: Unraveling time dependent contamination growth on multilayers and thin films", Surf. Sci. **616**, 161-165 (2013).
- S. Gusenleitner, E. Handick, **D. Hauschild**, and F. Reinert, "Quantitative analysis of electron energy loss spectra and modelling of optical properties of multilayer systems for extreme ultraviolet radiation regime", J. Appl. Phys. **115**, 123513 (2014).
- M. Wießner, **D. Hauschild**, C. Sauer, V. Feyer, A. Schöll, and F. Reinert, "Complete determination of molecular orbitals by measurement of phase symmetry and electron density", Nat. Commun. **5**, 4156 (2014).
- F. Meyer, M. Blum, A. Benkert, **D. Hauschild**, S. Nagarajan, R. G. Wilks, J. Andersson, W. Yang, M. Zharnikov, M. Bär, C. Heske, F. Reinert, and L. Weinhardt, ""Building block picture" of the electronic structure of aqueous Cysteine derived from resonant inelastic soft x-ray scattering", J. Phys. Chem. B **118**, 13142-13150 (2014).
- A. Benkert, F. Meyer, **D. Hauschild**, M. Blum, W. Yang, R. G. Wilks, M. Bär, F. Reinert, C. Heske, and L. Weinhardt, "Isotope effects in the resonant inelastic soft x-ray scattering maps of gas-phase methanol", to be published (2015).

Danksagung

Ebenso wie andere wissenschaftliche Arbeiten, ist auch diese hier nicht im "dunkeln Kämmerchen" allein entstanden, sondern war vielmehr ein langwieriger Prozess, zu dessen Gelingen viele beigetragen haben. Deshalb möchte ich mich bei den Folgenden bedanken:

Bei **Prof. Dr. Friedrich Th. "Friedel" Reinert** möchte ich mich bedanken, weil er es mir ermöglichte, in seiner Arbeitsgruppe dieses spannende Thema zu bearbeiten. Dazu gehörte nicht nur die finanzielle Unterstützung für die regelmäßigen Fahrten ans Karlsruher Institut für Technologie (KIT) und Strahlzeiten in Berkeley, sondern vielmehr die Fähigkeit zum richtigen Zeitpunkt Ideen und Kommentare zu geben sowie kritisch nachzufragen. Der dabei erweiterte Blickwinkel half von anderen Systemen sowie Methoden zu lernen.
Herrn **Prof. Dr. Jens Pflaum** danke ich für die Übernahme des Zweitgutachtens.
Dr. Lothar Weinhardt möchte ich danken, da er es mir ermöglichte an diesem hochinteressanten Projekt zu arbeiten. Danke sagen muss ich auch für die große Unterstützung, die Möglichkeit, ihn immer anrufen zu können (trotz seines übervollen Terminkalenders) und natürlich für seine ansteckende Begeisterung, Daten zu analysieren und immer noch das letzte Bisschen aus ebendiesen herauszukitzeln.
Des Weiteren haben meine Büromitstreiter einen großen Anteil am Gelingen dieser Arbeit:
Andreas Benkert danke ich dafür, dass er immer darauf geachtet hat, dass alle im Boot sind (oder Hubschrauber) und entsprechend für seine lebenserhaltenden Maßnahmen. Ferner danke ich für die vielen hilfreichen Diskussionen rund um XES Messungen sowie die ganzen Igor und Inventortipps.
Frank Meyer danke ich dafür, dass zumindest er die gleichen Kernarbeitszeiten hatte und mit mir bis mindestens 10 Uhr die Stellung hielt. Des Weiteren danke ich für die vielen Diskussion, egal ob zu Bandverbiegung, Stöchiometrie oder vielen anderen Themen.
Holger Schwab danke ich dafür, dass er immer hilfreiche Tipps zu jeglichen Alltagsthemen gab. Zusätzlich halfen die Diskussion zu Untergründen und mittleren freien Weglängen.

Danke auch für die regelmäßig wiederkehrenden Einführungen in die Kondophysik.
Vielen Dank Jungs, für die tolle Zeit!

Den Mitarbeitern bzw. ehemaligen Mitarbeitern der AVANCIS GmbH & Co. KG, insbesondere **Dr. Stephan Pohlner** für die Herstellung der vielen vielen Proben sowie **Dr. Jörg Palm** und **Dr. Thomas Dalibor** für die meist kurzfristige Freigabe der Veröffentlichungen. **Dr. Dagmar Kreikemeyer Lorenzo** danke ich für die lockere und freundschaftliche Zusammenarbeit und die vielen hilfreichen Telefonate/Diskussionen. Erwähnenswert ist auch ihre bemerkenswerte Fähigkeit, jeden auf einer Strahlzeit aufzuheitern. ¡Muchas gracias!
Der **Mechanikwerkstatt** danke ich für den Bau von den Probenhaltern, des IPES-Detektors sowie den vielen Kleinigkeiten. Der **Elektronikwerkstatt** danke ich für die Reparaturen der "altersschwachen" CLAM 4 Controller und Planung sowie Aufbau von den Steuereinheiten für den IPES Aufbau.
Vielen Dank an **Dr. Moni Blum** für den reibungslosen Ablauf der Strahlzeiten und die vielen netten Gesprächsrunden. Des Weiteren danke ich der restlichen "SALSA" Gruppe, für die tolle Arbeitsatmosphäre.
Auch habe ich der "Helmholtzgruppe" um **Prof. Dr. Marcus Bär** für das Teilen eines Zimmers während der Konferenz in Straßburg (trotz der nächtlichen Holzfällarbeiten von **Roberto F. Duarte**) sowie für die tollen Strahlzeiten und natürlich für den Wissensaustausch rund um In_2S_3 Puffer zu danken.
Prof. Dr. Sven Tougaard danke ich für die freundliche Einführung in die QUASES-Welt und für die geduldige Beantwortung all meiner Fragen.
Prof. Dr. Clemens Heske danke ich für den vielen Input während des Paper Schreibens, für die KIT-Runden, bei denen ich mir von ihm viel Wissen aneignen konnte und für die Unterstützung während des IPES-Detektorbaus.
Darüber hinaus danke ich **Sina Göhl-Gusenleitner** und **Evelyn Handick** für den gewinnbringenden REELS Diskussionen und dem reibungslosen Aufteilen der Messzeit an der Kammer.
Dr. Michael Wießner, **Dr. Christoph Sauer** sowie **Patrick Bayersdorfer** haben stets für die "sarkasmusfreie" physikalischen und nicht-physikalische Diskussionen gesorgt. Mille grazie!
Während dieser Dissertation sind auch im Rahmen der Masterarbeit von **Angela Eckstein** sowie **Evelyn Handick** und der Bachelorarbeit von **Katharina Treiber** tolle Daten entstanden, die zum Teil auch den Weg in diese Arbeit gefunden haben.
Ich danke auch der **AG Fauth** und insbesondere **Martin Zinner** für das zur Verfügung stellen der Glovebox. Ohne diese wären die Proben sehr viel "dreckiger" und ich hätte somit viel mehr Oberflächenadsorbate entfernen müssen.

Ich danke auch der gesamten **EP VII** für die tolle gemeinschaftliche Arbeitsatmosphäre während der letzten Jahre.
Vielen Dank auch an **Dr. Sina Zapf** für die vielen hilfreichen Tipps rund um das Zusammenschreiben.

Zu guter Letzt: Diese Arbeit wäre ohne die Unterstützung und das Gewähren der notwendigen Freiräume von meiner Familie so nicht möglich gewesen. Der herzlichste Dank gebührt deshalb meiner Frau **Melanie** und meinen Kindern **Anni** und **Julius**. "Tausend Dank".